Multi-spectral Dual Axes Confocal Endomicroscope with Vertical Cross-sectional Scanning for *in-vivo* Targeted Imaging of Colorectal Cancer

by

Zhen Qiu

A dissertation submitted in partial fulfillment
of the requirements for the degree of
Doctor of Philosophy
(Biomedical Engineering)
in the University of Michigan
2014

Doctoral Committee:

Associate Professor Thomas D. Wang, Chair
Associate Professor Xudong Fan
Professor Katsuo Kurabayashi
Associate Professor Kenn R. Oldham
Professor Albert J. Shih

Dedication

To my family

Acknowledgements

I would like to thank to Professor Thomas D. Wang for his guidance, patience, and kindness. The research and dissertation would not have been possible without his support. I would like to express thanks to the guidance and help from Professor Albert Shih, Professor Kenn Oldham and Professor Katsuo Kurabayashi, Professor Xudong Fan.

I would like to thank Xiyu Duan, Dr. Haijun Li, Dr. Zhongyao Liu, Dr. Supang Khondee, Dr. Joshi Bishnu, Dr. Emily Rabinsky, Quan Zhou, Jongsoo Choi, and other group members for their countless efforts in helping me with my projects and research studies.

I am grateful for the friendship of team members from Professor Katsuo Kurabayashi's Bio-MEMS Lab and Professor Kenn Oldham's Vibrations & Acoustics Lab, especially Dr. Choong-ho (Chris) Rhee, with whom I worked closely on the piezo-MEMS process and characterization experiments. I would like to express thanks to researchers and technical stuffs at Lurie Nanofabrication Facility, especially Dr. Pilar Herrera Fierro, Dr. Nadine Wang, Ed Tang, for their plentiful instructions on the microfabrication. I also thank Dr. Weibin Zhu and Dr. Tao Ling for their discussion and help on the MEMS device development.

I would like to thank our collaborators at Stanford University, Dr. Mike Mandella, Dr. Hyejun Ra, Dr. Wibool Piyawattanametha, Dr. Jonathon Liu, Dr. Jae-Woong Jeong for their friendship and help on the dual axes confocal endomicroscopy project.

Finally, I would like to thank my wife, Jing Chen, for her unwavering love, support and encouragement. I am so thankful for my parents for their unconditional love, endless patience and never ending knowledge.

Table of Contents

List of Figures

List of Tables

List of Abbreviations

NA	**numerical aperture**
WD	**working distance**
NIR	**near infra-red**
FOV	**field of view**
MSA	**mechanical scan angle**
OSA	**optical scan angle**
FWHM	**full width at half maximum**
SIL	**solid immersion lense**
PMT	**photomultiplier tube**
WDM	**wavelength division multiplexing**
MEMS	**microelectromechanical systems**
PZT	**lead zirconate titanate**
SOI	**silicon on insulator**
DRIE	**deep reactive-ion etching**
LPCVD	**low pressure chemical vapor deposition**
PECVD	**plasma enhanced chemical vapor deposition**

PDMS	**polydimethylsiloxane**
SEM	**scanning electron micrograph**
FEM	**Finite Element Modeling**
SPDT	**single point diamond turning**
PCB	**printed circuit board**

Abstract

Pathologists review histology cut perpendicular to the tissue surface or in the vertical cross-section (XZ-plane) in order to visualize the normal or abnormal differentiation patterns. The epithelium of hollow organs, such as the colon, is the origin of many important forms of cancer. The vertical cross-section provides a comprehensive view of the epithelium which normally differentiates in the basilar to luminal direction. Real-time imaging in this orientation has not been fully explored in endomicroscopy because most instruments collect images in the horizontal cross-section (XY-plane). Imaging microstructures from the tissue surface to about half a millimeter deep can reveal early signs of disease. Furthermore, the use of molecular probes is an important, emerging direction in diagnostic imaging that improves specificity for disease detection and reveals biological function. Dysplasia is a pre-malignant condition in the colon that can progress into colorectal cancer. Peptides have demonstrated tremendous potential for *in-vivo* use to detect colonic dysplasia. Moreover, peptides can be labeled with NIR dyes for visualizing the full depth of the epithelium in small animals. This study aims to demonstrate large FOV multi-spectral targeted

in-vivo vertical optical section with a dual axes confocal endomicroscope enabled by MEMS technology. The NIR multi-spectral fluorescence images demonstrate both histology-like morphology imaging and molecular imaging of specific peptide binding to dysplasia in the mouse colon. The specific aims of this study are: (1) to develop miniature vertical cross-sectional scan engine based on MEMS technology for imaging on XZ-plane; (2) to integrate micro-optics and develop multi-spectral dual axes confocal endomicroscope imaging system; (3) to perform *in-vivo* targeted vertical cross-sectional imaging with large FOV on colorectal cancer mouse model.

Chapter 1

Introduction

Tremendous advances have been made in the technological development of whole body molecular imaging, including PET, SPECT, MRI, bioluminescence, and ultrasound. However, a great unmet need still exists for high resolution imaging of biological processes that occur in the epithelium, the thin layer of tissue in hollow organs where many important cancers originate. Optical imaging has played a key role in medical diagnostics and biomedical research in the clinic and laboratory. Diagnosis is often performed on excised tissues, examining them under high-power microscopes to look at cellular abnormalities. Analysis of biopsied tissues has been the gold standard for cancers that are epithelial in origin, starting at subsurface layers. By convention, pathologists review histology cut perpendicular to the tissue surface or in the vertical cross-section (XZ-plane) in order to visualize the normal (or abnormal) tissue maturation pattern. The vertical cross-section provides a comprehensive view of the epithelium which normally differentiates in the basilar to luminal direction. The epithelium of hollow organs, such as the colon, is the origin of many important types of cancer. Imaging microstructures from the tissue surface to about half a millimeter deep can reveal early signs of disease and progression.

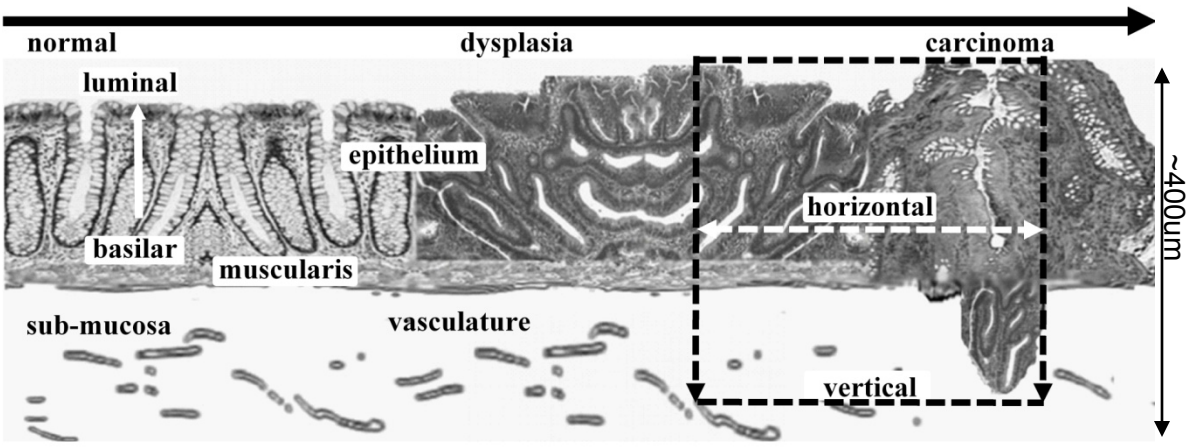

Figure 1.1 – Carcinoma of the colon arises from a transformation of normal epithelium to dysplasia. Subtle molecular changes develop first in the crypts prior to morphological changes in the tissue. An intra-vital microscope placed on the luminal surface of the tissue can be used to study the molecular progression of this disease longitudinally in small animal models. Imaging in the vertical cross-section (plane perpendicular to tissue surface) is the preferred orientation for detecting subtle differences in tissue differentiation patterns and for identifying the early presence of invasion, compared to the horizontal cross-section (parallel to tissue surface).

As shown in Fig. 1.1, normal colonic epithelium transforms to a pre-malignant condition (dysplasia) prior to evolving into carcinoma [1]. Molecular changes develop well in advance of morphological changes. Real-time *in-vivo* imaging in the vertical cross-section (dashed black box, around 800 μm wide x 400 μm deep) which is the plane perpendicular to the tissue surface provides a comprehensive view of the epithelium which normally differentiates in the basilar to luminal direction. This real-time vertical cross-sectional scanning orientation also can accurately register the location of biological behavior of interest relative to the tissue surface. Imaging in the horizontal cross-section (dashed white line) which is the plane parallel to the tissue surface reveals a local view of the epithelium along a surface that tends to have a similar degree of differentiation. This en-face scanning orientation will not provide information about biological

behavior either above or below this plane, and can be difficult to register the location relative to the tissue surface.

1.1 Current Technologies and Challenges

The vertical cross-section (XZ-plane) presents histology-like images for diagnosis and quantitative studies of early cancer development. Imaging in this orientation has not been fully explored in endomicroscopy because most instruments do not have sufficient dynamic range to collect images in the vertical cross-section [2-6]. Imaging in the XY-plane (parallel to the tissue surface) visualizes tissue that tends to have similar microarchitecture over the FOV. Imaging in the vertical cross-section on miniature endomicroscopy faces many technical challenges. One of the greatest challenges for performing high resolution (sub-cellular) imaging in small animal or human hollow tissue is the ability to overcome motion artifact, including respiratory displacement, heart beating, and organ peristalsis. For small animal imaging, conventional intra-vital microscopes (e.g. Olympus IV100, Tokyo, Japan) use bulk optic objectives that are fixed to large, stationary platforms. As a result, motion will occur in live animals relative to the objective that appear exaggerated in the relatively small field-of-view of intra-vital microscopes, typically on the order of a hundred microns. On the other hand, an endomicroscope can have sufficiently small size and weight to move relative to the bodily motion of the animal during the imaging session, thus substantially reduce the motion artifact in the images. Fiber coupling allows for the image to be transmitted to the detector. Furthermore, the

small size of these instruments provides much better positioning accuracy onto target organs. MEMS and micro-optics technologies enable the development of miniature endomicroscopes within space constraints of millimeter dimensions. An axial scanning method has been demonstrated that translates a bulky or miniature objective lens placed in direct contact with the tissue [7-9]. However, this strategy can introduce significant image distortions [10]. The confocal endomicroscope jointly developed by Pentax (Montvale, NJ, USA) and Optiscan (Victoria, Australia) [3] uses a thin nitinol based wire actuator for Z-axis scanning inside the instrument. Unfortunately, the scanning speed of this actuator is so limited, and the instrument can only perform en-face (XY-plane) imaging with Z-stack. In addition, the accuracy of the Z-axis scan is influenced significantly by the natural hysteresis in the actuator.

1.2 Novel Dual Axes Confocal Architecture

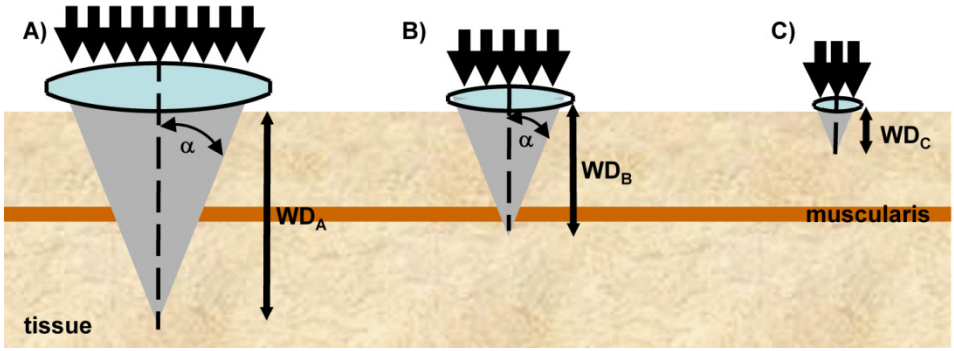

Figure 1.2 – For improved access to the epithelium in small animal models, the diameter of the intra-vital microscopy must be reduced in size. Conventional microscopes use a single axis configuration where the incident beam is aligned on-axis with the objective. As the diameter of the objective is reduced from A)→B)→C), the working distance (WD), imaging depth, and FOV are also diminished.

In conventional microscopy, high NA objective lenses are used to achieve sub-cellular resolution. This strategy cannot be used in endomicroscopy without incurring a tradeoff in either working distance or FOV, as shown in Fig. 1.2. Recent advancements in miniaturization of optics, availability of fiber-optics, and emergence of micro-scanners have allowed for the technique of confocal microscopy [2, 3, 11, 12] to be performed in vivo through medical endoscopes to perform rapid, real-time optical assessment of tissue pathology.

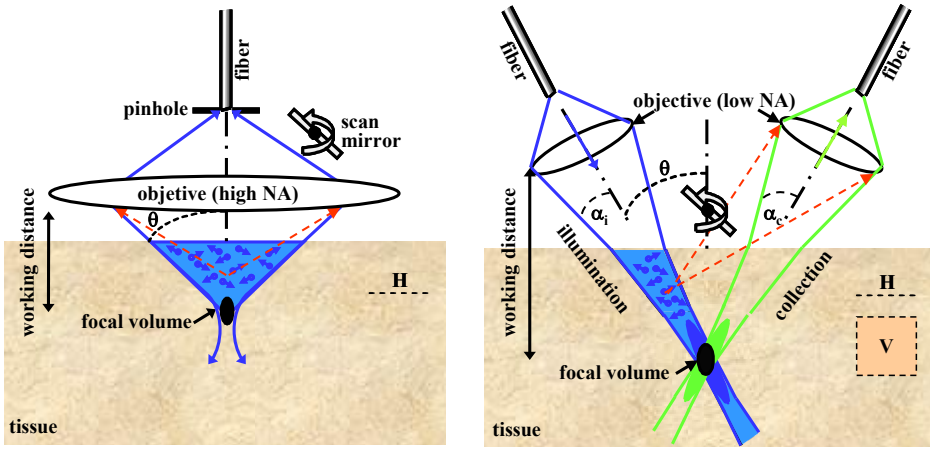

(A) single axis (conventional) **(B) dual axes (innovation)**

Figure 1.3 – (A) In the conventional single axis configuration, the fiber (pinhole) is aligned with the optical axis of the objective, requiring a high NA to achieve sub-cellular resolution. (B) The dual axes architecture uses separate, low NA objectives to achieve sub-cellular resolution and long working distance. Post-objective scanning provides a large field-of-view and instrument scalability to millimeter dimensions. Both vertical (V) and horizontal (H) cross-sectional images can be collected because of the reduced collection of light scattered by tissue (dashed orange lines).

Current miniature intra-vital endomicroscopes all use the conventional single axis optical design, shown in Fig. 1.3A, where the pinhole (single mode optical fiber) and objective are located along the same optical axis [13]. A high NA objective is needed to achieve sub-cellular resolution, limiting the working

distance as discussed above. Consequently, the scanning mechanism (mirror) is placed on the pinhole side of the objective, or in the pre-objective position, and this design cannot be scaled down in dimension without loss of working distance or FOV. Furthermore, much of the light that is scattered by the tissue present between the objective and focal volume (dashed orange lines) is collected with the high NA objective, reducing the dynamic range of detection.

The novel dual axes architecture [14], shown in Fig. 1.3B, is an innovation that challenges the current paradigm of (single axis) confocal microscopy, Fig. 1.3A. The dual axes confocal microscope uses two low NA objectives and separate illumination and collection beams that intersect to achieve subcellular resolution in both the transverse and axial dimensions. The low NA objectives create a long working distance so that the scan mirror can be placed on the tissue side of the lens, or in the post-objective position. Very little of the light that is scattered by tissue along the illumination path (dashed orange lines) is collected by the low NA objective, thus the dynamic range is significantly improved. Consequently, optical sections can be collected in both vertical (V) and horizontal (H) planes with dual axes, as compared to horizontal only for single axis. Vertical cross-sections show the relationship among tissue micro-structures as they vary with depth, and are the preferred view of pathologists [15-17]. The single axis optical configuration does not have sufficient dynamic range to provide this view. In intra-vital microscopy, scanning of the focal volume is performed to create an image. In the dual axes configuration, the low NA objectives create a long working distance that allows for the scanner to be placed

in the post-objective position [15-17]. This design feature is critical for scaling the size of the instrument down to millimeter dimensions for in vivo imaging in small animal models without losing performance. The scan mirror can sweep a diffraction-limited focal volume over an arbitrarily large FOV, limited only by the maximum deflection angle of the mirror. In comparison, in the conventional microscope, axial scanning is realized by moving objective lens, in Fig. 1.4. *In-vivo* imaging on living animal will not be practical due to the motion artifacts. For endomicroscopes, which usually contact tissue surface, the novel axial scanning with dual axes confocal architecture will be better approach.

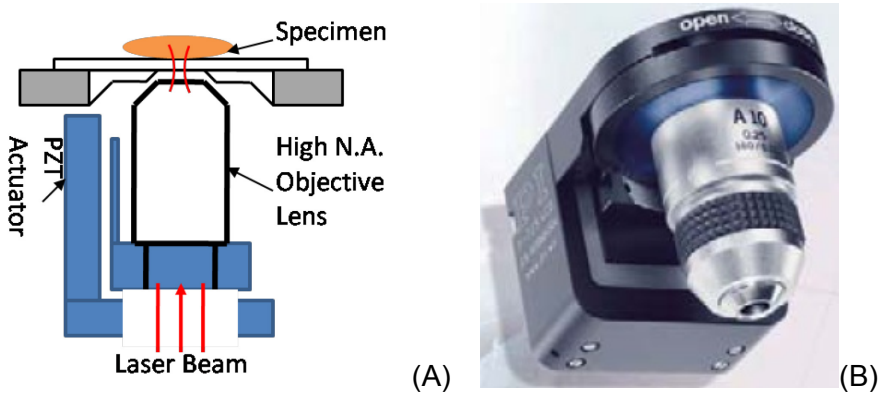

Figure 1.4 – Conventional axial scanning with objective lens. In the single axis confocal microscopy, moving the distal end objective lens can realize the axial scanning while the pre-objective XY-plane scan is used for en-face imaging. (A) Schematic design; (B) Photography of bulk PZT based Z-axis actuator (with objective lens mounted) Physik Instrumente company.

The dual axes design was shown to have superior rejection of out-of-focus and multiply scattered light using Monte-Carlo analysis [18]. Moreover, using diffraction theory to determine the drop-off in the axial response, this configuration was shown to achieve a significant improvement in dynamic range compared to that of a comparable single axis design [17]. This property of the

dual axes design allows for imaging in the vertical cross-section. Off-axis illumination and collection of light with low numerical aperture objectives in the dual axes confocal architecture provides a significant improvement in dynamic range compared to that of single axis. This unique geometry allows for the collection of fluorescence images in vertical cross-sections (perpendicular to tissue surface), an orientation that provides a comprehensive view of the normal tissue differentiation patterns of the epithelium, the origin of cancer in the colon.

The improvement in dynamic range in a non-scattering media can be quantified using diffraction theory with paraxial approximations [18]. Numerical simulation (in Matlab®) has been performed [19]. The superior dynamic range of detection for dual axes in comparison to that of single axis has been further evaluated using a tissue scattering (turbid) model [20, 21]. Calculations performed to analyze these effects are based on Monte Carlo simulations using a non-sequential ray tracing program (ASAP® 2006, Breault Research Organization, Tucson, AZ). For both non-scattering and scattering media, in order to achieve the same axial resolution (FWHM) in the single axis configuration, much higher NA (nearly double) is needed.

The superior dynamic range of detection of the dual axes configuration allow for the collection of vertical cross-sectional images. This capability has been demonstrated on a table-top prototype imaging system [17]. The transverse and axial resolutions are experimentally measured to be x = 1.4 μm, y = 1.2 μm, and z = 2.5 μm, respectively. Post-objective scanning is performed with a galvo scan mirror (VM500,GSI Lumonics) in the fast-axis at 950 Hz, and with a piezo

translation stage (P-290, Physik Instrumente) in the slow-axis at 2 Hz. In this research study, these bulky scanning mechanisms will be scaled down and realized by MEMS scanner and thin-film PZT actuator for miniature microscope instrument. Vertical cross-sectional fluorescence images of colon was collected with the tabletop dual axes confocal microscope [17]. With use of post-objective scanning, a very large field-of-view of 800 μm wide by 500 μm deep was achieved. Furthermore, the imaging system was scaled down in size to millimeter dimensions using fiber coupling and post-objective scanning to provide a long working distance with a large FOV [22, 23] for *ex-vivo* and *in-vivo en-face* imaging.

Compared to the existing commercial imaging instruments, the optical properties of the novel dual axes confocal architecture offers significant advantages in imaging performance (Table. 1.1) over that of other miniature single photon intra-vital microscopes [24-28] that are available for performing in vivo imaging. All of these instruments employ the conventional single axis configuration, perform horizontal cross-sectional imaging only, and have limitations in working distance, field-of-view, dynamic range, and tissue penetration depth for the reasons discussed above. In addition, compared to the multi-photon microscope system, which is a now becoming commonly used method for performing intra-vital deep imaging studies [29-33], the dual axes confocal microscope still has significant advantages. The multi-photon effect occurs when two lower energy (longer wavelength) photons arrive at a biomolecule simultaneously to excite fluorescence [34]. Multi-photon microscope

requires expensive light sources (lasers) to provide the high peak powers and ultrashort pulses required to perform real time in vivo imaging, The ultrashort pulse lasers may have unknown nonlinear effect on tissue sample. The cost and size of the imaging system currently limit its the mobility and clinical application from bench-top to bedside. Also, these lasers need to be tuned to produce different excitation bands, thus multi-spectral images are collected sequentially rather than simultaneously. This limits the ability of two-photon microscopy to study ligand-receptor interactions and cell tracking behavior.

Tech	Diameter (mm)	Resolution (μm)	Speed (frame/sec)	Field of View (μm x μm)	Imaging Depth (μm)	Wavelength (nm)
Olympus IV100	1.3~3.5 "stick" lenses	*NO Optical Sectioning (non-confocal)*			200	488, 561, 633, 748
Pentax OptiScan	6, integrated into Pentax Endoscope	Lateral: 0.7 Axial: 7	~1fps	600 X 500 *(en-face)*	0~200 adjustable	488 only
Mauna Kea Cellvizio®	2.5, flexible fiber	Lateral: 3.5 Axial: 13	12fps	600μm diameter *(en-face)*	0~120 non-adjustable	488 only
Proposed Miniature Dual Axes Endomicroscope	5 , flexible fiber	Lateral: 2 Axial: ~4	>10 fps	800 X 500 (vertical cross-section)	0~500 adjustable 5Hz~10Hz	680~785, Multispectral

Table. 1.1 – Comparison Summary. Compared to the existing commercial imaging instruments, the optical properties of the novel dual axes confocal endomicroscope offers significant advantages in imaging performance over that of other miniature single photon endomicroscopes.

1.3 Peptides as Molecular Probes

The use of molecular probes is an important, emerging direction in diagnostic imaging that improves specificity for disease detection and reveals

biological function. Dysplasia is a pre-malignant condition in the colon that increases risk for progression onto cancer. Peptides have demonstrated tremendous potential for in vivo use to detect colonic dysplasia [35, 36]. This class of *in-vivo* molecular probe can be labeled with near-infrared (NIR) dyes for visualizing the full depth of the epithelium in small animals. Peptides have demonstrated tremendous potential for use as molecular probes to identify cell surface targets *in-vivo* [37, 38]. In addition to high clonal diversity, small size, low immunigenicity and compatibility with fluorescence dyes (such as FITC, Cy 5.5, Cy 7, and LI-COR), peptides exhibit rapid binding kinetics and high binding specificity. Targeting peptides have been developed using techniques of phage display, a powerful combinatorial method that uses recombinant DNA technology to generate a complex library of peptides for selection by preferential binding to cell surface targets [39, 40]. The protein coat of bacteriophage, such as the filamentous M13 or icosahedral T7, is genetically engineered to express a very large number (>109) of different peptides with unique sequences to achieve high affinity binding [41]. Selection is then performed by bio-panning the phage library against cultured cells that over-express the target [42-44]. The DNA sequence of candidate phage are then recovered and used to synthesize the peptide. Moreover, peptides can be labeled with near-infrared dyes for imaging over the full depth of the epithelium in small animal model of colon cancer. The binding of peptides to target receptors can be observed *in-vivo* with *intra-vital* microscopy to perform disease detection, therapy monitoring, and drug discovery. Selected

peptides that are fluorescence-labeled will be provided by collaborators in our research group for *in-vivo* targeted imaging.

1.4 Summary

In this dissertation, I will present my work in addressing this important biomedical research problem by developing a novel multi-spectral *intra-vital* endomicroscope which can perform real-time imaging of the full depth (over 400 μm) of the epithelium in vertical cross-sections, an orientation that is not currently available with any other molecular imaging approach. Imaging in the plane perpendicular to the tissue surface is highly sensitive to the subtle changes in normal tissue differentiation patterns that can reveal the early expression of cancer biomarkers. I will develop an integrated molecular imaging strategy that provides a comprehensive view of the biological differentiation patterns in mouse model of colon cancer. Based on a novel dual axes confocal architecture, we will develop new scanning mechanism for *in-vivo* fluorescence imaging in vertical cross-sections. This innovative approach uses off-axis illumination and collection of light to overcome tissue scattering and achieve superior dynamic range for fluorescence detection. In addition, this configuration can achieve sub-cellular resolution (< 5 μm) with deep tissue penetration (> 400 μm) and large FOV (> 800 μm). Imaging performance will be demonstrated in small animal model of colorectal cancer.

Chapter 2

Dual Axes Confocal Endomicroscope System Development

In Chapter 2, dual axes confocal endomicroscope system design and development will be described in details. Different axial scan strategies will be introduced for the vertical cross-sectional imaging with miniature endomicroscope. Multi-spectral imaging system integration and development will be introduced in details.

2.1 Vertical Cross-sectional Scanning

As a preferred view mode for pathologists, XZ-plane imaging helps visualize the differentiation between normal tissue and tumor from the superficial layer of hollow organs (e.g. the colon) to sub-millimeter depth in the epithelium [45]. However, this view has rarely been exploited by endomicroscopes while en-face (XY-plane) imaging with slow z-stacking must be resorted to, largely because fast axial scanning is challenging in limited space. Imaging system design will be described in this section. Several axial scanning mechanism for miniature dual axes confocal endomicroscope will be introduced in details later.

2.1.1 Imaging System Design

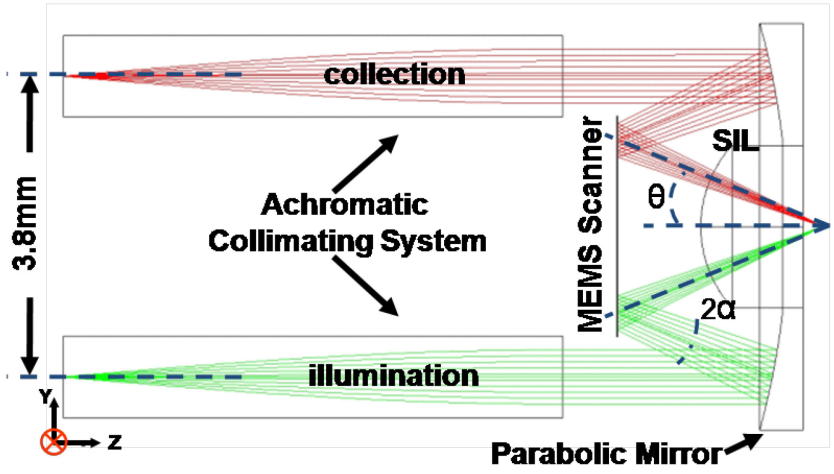

Figure 2.1 – Dual axes endomicroscope architecture. Cross-sectional view of the dual axes endomicroscope architecture shows ray-tracing simulation in ZEMAX for achieving large FOV 3D images with low NA micro-optics and post-objective scanning strategy.

We determined the scan parameters needed to achieve vertical cross-sectional images with the miniature dual axes endomicroscope design in colonic epithelium by performing ray-trace simulations in ZEMAX (2012, Release 2, Redmond, WA), Fig. 2.1. In the dual axes confocal endomicroscope architecture, low NA optics with post-objective scanning strategy provides large working distance (WD) and sub-cellular lateral and axial resolution. Two collimated beams are focused at an inclination angle θ to the Z-axis by a parabolic mirror with a maximum cone half-angle α to a common point in the tissue after being deflected by a MEMS scanner. From these simulations, we found that we can achieve vertical cross-sectional images having an 800 μm FOV in the transverse dimension (X-axis) by requiring a MEMS scanner that has a mechanical scan angle (MSA) of ±6 degrees, Fig. 2.2. The three pairs of spots in Fig. 2.2B

represent the focus points of the illumination and collection beams at either extent of the scanning range and on X-axis. The relations from diffraction theory [17] give us a predicted lateral resolution of 1.9 μm on X-axis and 1.7 μm on Y-axis, and the predicted axial resolution is 4.2 μm (all at 671 nm wavelength). The Z-axis actuator moves the focal volume over a range of ~ 400 μm below the tissue surface, in Fig. 2.2A, which is sufficient for imaging colonic epithelium in the mouse (< 200 μm) or human (< 500 μm). The scanning mirror of the MEMS scanner in the optical circuit has the ability to be translated up to ~ 1 mm in a forward/backward direction by the z-axis actuator. However, the real vertical range for imaging is limited by beam-clipping at the outside diameter (1.8 mm) of the solid immersion lens (SIL, Fig. 2.1).

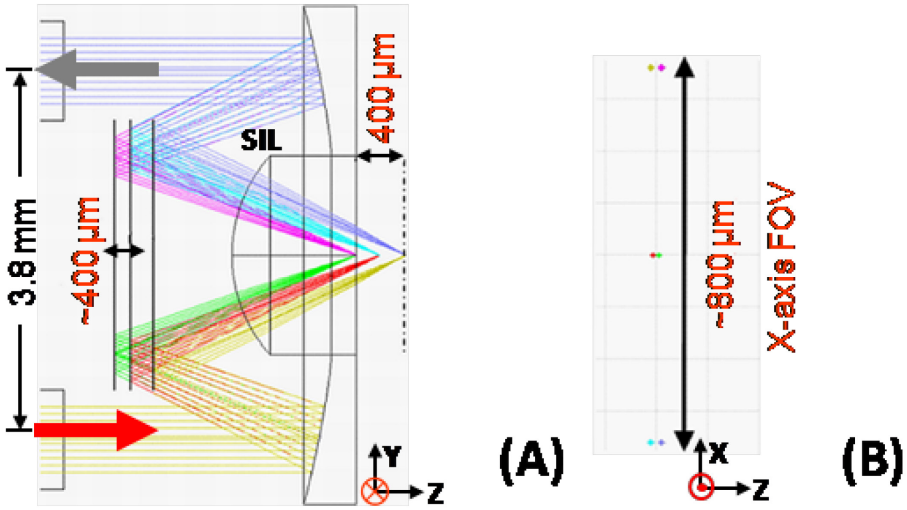

Figure 2.2 – Endomicroscope schematic. (A) Cross-sectional view of dual axes architecture shows ray-tracing simulation in ZEMAX for achieving 800 μm (width)×400 μm (depth) images. (B) X-axis 800 μm FOV at mechanical scan angle of ±6 degrees.

Detailed schematic of X-axis scanning ray-tracing simulation in ZEMAX is shown in 3D view (Fig. 2.3A) and side-view (Fig. 2.3B).

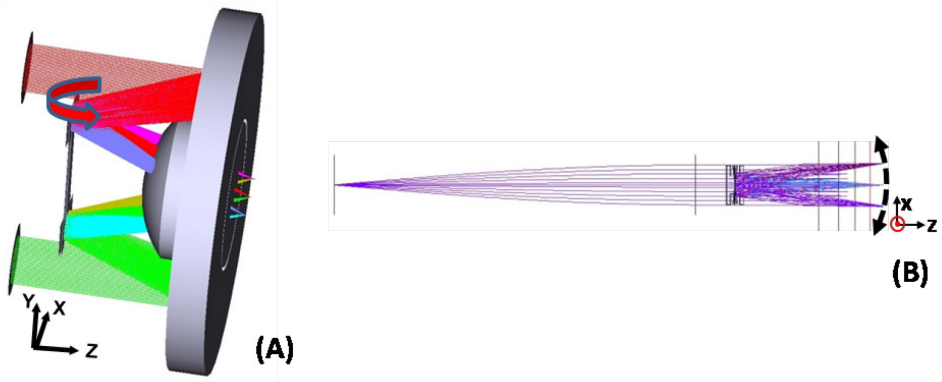

Figure 2.3 – X-axis scanning schematic. (A) 3D schematic of X-axis scanning rat-tracing simulation in ZEMAX. (B) Side view of the X-axis scanning ray-tracing simulation in ZEMAX.

Detailed schematic of Y-axis scanning ray-tracing simulation in ZEMAX is shown in side-view (Fig. 2.4).

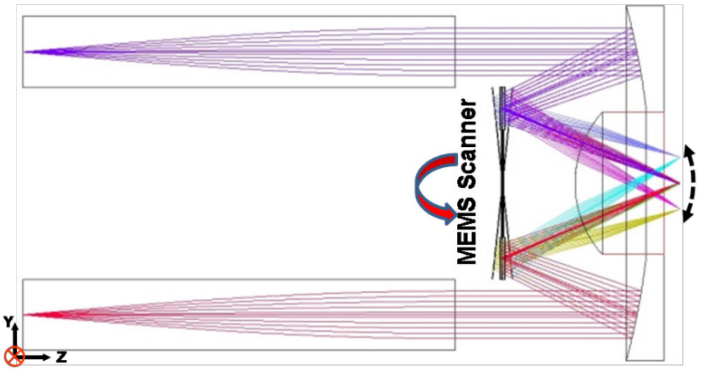

Figure 2.4 – Y-axis scanning schematic. Cross-sectional view of dual axes architecture shows ray-tracing simulation of Y-axis scanning in ZEMAX.

The refractive index of the bulk colon tissue specimen is around 1.37. When the beam incidence into the bulk tissue with a large angle, it will be

refracted at the surface of the tissue with aberrations. If there is a solid immersion lens (SIL, n~=1.4) which refractive index is very similar with the tissue specimens, the light will vertical incidence the surface of the SIL and the aberrations is reduced. Fig. 2.5 shows the simulation results with ZEMAX. Compared with the design without SIL (Fig. 2.5B), we find that the aberrations are reduced by using SIL contacting tissue specimens, as shown in Fig. 2.5A.

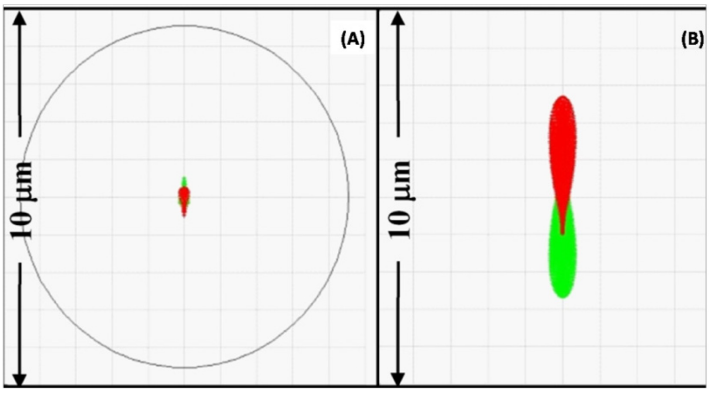

Figure 2.5 – Solid immersion lens in the design. The focus spot performance of dual axes confocal endomicroscope with SIL at the end is shown in (A).The focus spot performance of dual axes confocal endomicroscope without SIL at the end is shown in (B), in which the spot size is ~4 times larger.

For single-color NIR dual axes confocal fluorescence endomicroscope, the fluorescence excitation is provided by a solid-state diode laser (671nm, 300 mW, CNI Laser Inc., Changchun, China) at λ_{ex} = 671 nm. The laser beam is coupled into a single mode fiber (S630-HP, NA=0.12, Nufern, East Granby, CT). The illumination beam (0.95 mm $1/e^2$ diameter) is delivered by a custom-made single mode fiber-coupled achromatic doublet lens (NT65-568, Edmund Optics, Barrington, NJ) collimator (2.99 mm focal length, GRINTECH GmbH, Jena, Germany). The optical path of the miniature dual axes microscope consists of

two parallel and collimated beams, each being used to provide an illumination and a collection optical path, respectively as shown in Fig. 2.1.

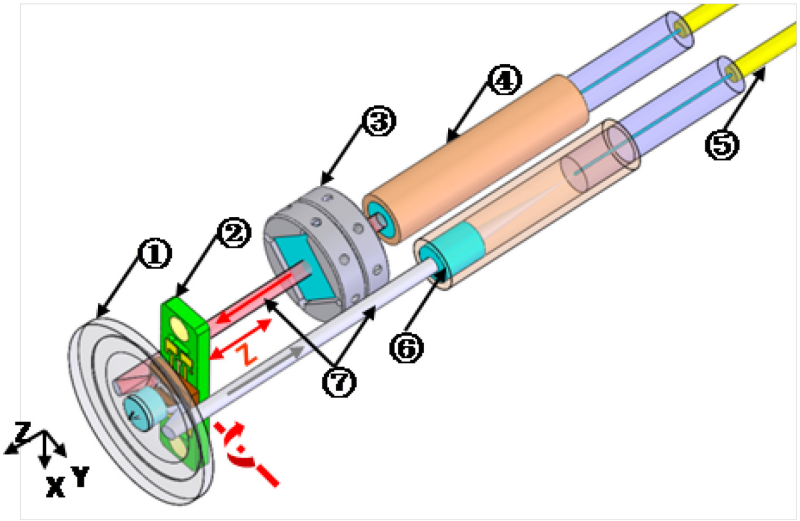

Figure 2.6 – Optical circuit design for dual axes confocal endomicroscope. Optical circuit design for vertical cross-sectional imaging with fiber-coupled achromatic collimators. Components: (1) Aluminum coated parabolic mirror with solid immersion lens (SIL) in center; (2) MEMS mirror with PCB holder; (3) Prism with holder; (4) Achromatic doublet lens based collimator; (5) Single mode fiber; (6) Achromatic lens; (7) Illumination (red) and collection beam (gray).

The collimators are fixed inside two precise parallel holes drilled using a computer numerical control (CNC) machine (Haas system). The metal package was manufactured at Protomatic (Dexter, MI). The illumination beam passes through two custom-made 0.1 deg optical wedges (Risley prisms) that are 3.5 × 3.5 mm^2 in dimension, made of N-BK7 glass, and anti-reflection coated with reflectivity <0.5% for 640-785 nm (Tower Optical, Boynton Beach, FL). Each Risley prism is held by a holder (Fig. 2.6, #3), which is located inside a sleeve through Class III medium fit. A miniature wrench is used to turn the processing holes. The Risley prisms provide fine adjustment to bring the illumination and

collection beams into a parallel relationship within 0.05 degrees. Optimal alignment is then validated by measuring the lateral and axial resolution. The center-to-center distance between the collimated beams is 3.8 mm. The beams are deflected by a MEMS scanner, shown in Fig. 2.6, located in the post-objective position. Multi-spectral imaging with the dual axes confocal endomicroscope is enabled by the fiber coupled achromatic collimator design without changing any micro-optics. Two NIR solid-state diode lasers with 671 nm and 785nm excitation wavelength will be coupled into the endomicroscope system for multi-spectral imaging.

2.1.2 Axial Scanning Mechanism

Miniature scanner is a key component for miniature endomicroscope to realize axial (Z-axis) scanning. In the conventional table-top or meso-scale microscopy, high NA objective lenses are commonly used to achieve sub-cellular lateral and axial resolution. The strategy by actuating the distal end objective lens (Fig. 2.7) cannot be used in endomicroscopy without incurring a tradeoff in either working distance or FOV. The dual axes architecture uses two low NA objectives and separate illumination and collection beams that intersect to achieve subcellular resolution in both the transverse and axial dimensions. In this study, we proposed several axial scanning strategies for vertical cross-sectional imaging with dual axes confocal endomicroscope.

2.1.2.1 Mini-motor based Axial Scanning Mechanism

We have developed the medical endoscope compatible miniature OD5mm dual axes confocal microscope prototype (in Fig. 2.7) using commercial micro-motor for slow axial (Z-axis) scanning in stepper style. The micro-motor based 5 mm-diameter miniature microscope can collect fluorescence en-face 2D images in horizontal cross-sections from Z = 0 to 500 μm in ~4 μm (optical axial resolution) interval layer-by-layer. Axial (Z-axis) translation is realized by a miniature brushless micro-motor which is commercially available from MINIMOTOR (Micromo, Faulhaber® Technology, Switzerland, manual [46]), Fig. 2.8A. The output rotation speed of micro-motor itself is around 6000 rpm. Then the rotation torque is transmitted through planet gearbox to the screw shaft which is connected to mechanical guide by nut and bracket. The Z-axis translational actuator mechanism will translate the MEMS scanner PCB stage smoothly if all the mechanism is perfectly assembled. However, the integration of the micro-motor based linear actuator system (shown in Fig. 2.8A) is challenging. We modified the wiring of micro-motor to fit inside the 5 mm miniature microscope (Fig. 2.8A). The bias of guide mechanism and mechanical assembling error essentially cause serious misalignment and motion hysteresis, shown in Fig. 2.8C. The micro-motor is controlled by commercial controller board (Fig. 2.8B) from MINIMOTOR with custom-made program (Fig. 2.8B) developed in our lab using LabVIEW®. Because of the limited space, the guide is not designed symmetrically. The control system is open-loop due to the lack of sensor for feedback control. Therefore, system compensation and calibration are performed to make the transmission system move properly.

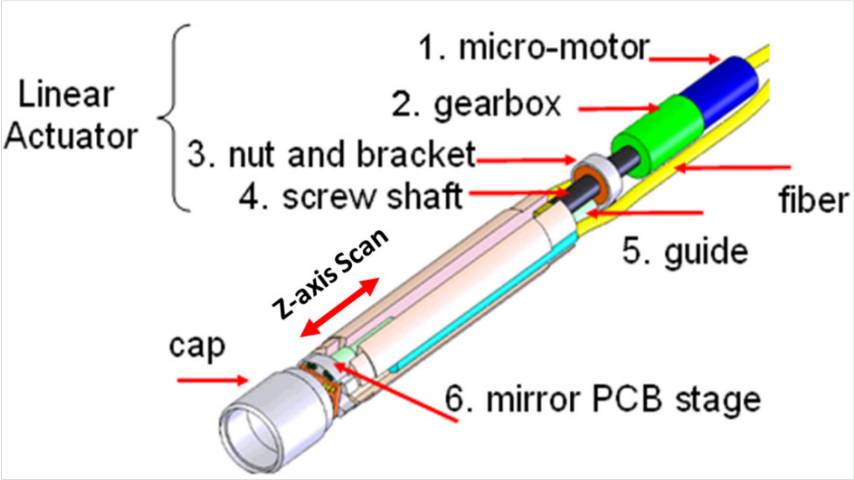

Figure 2.7 – Electromagetic mini-motor driven in OD5mm dual axes confocal endomicroscope. Key mechatronic components: (1) Micro-motor (micro-mo); (2) Gearbox (3) Nut and bracket for connection between screw and mechanical guide ; (4) High reduce ratio screw shaft to realize ~20 to 200 μm/sec linear motion; (5) Mechanical guide for connecting micro-mirror' PCB stage with linear actuator; (6) Scanner PCB stage is a holder for MEMS scanner and wiring, in the future MEMS thin film PZT Z-axis actuator will also be mounted on it. Linear actuator consists of gearbox in front of the MEMS scanner, tiny nut and the screw shaft.

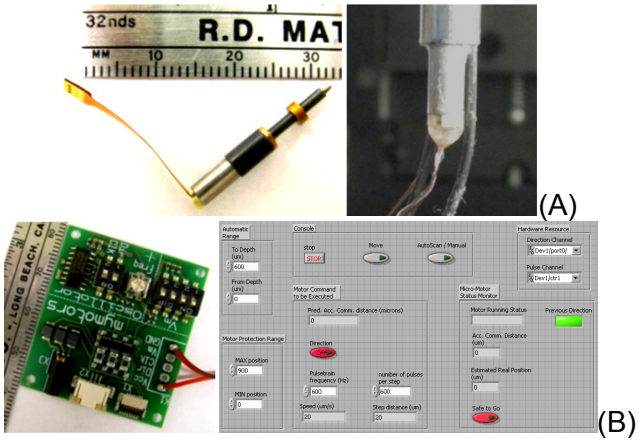

Figure 2.8 – Electromagetic mini-motor details. (A) Micro-motor and translation mechanism on the head, the ribbon of micro-motor is hand-made modified to fit the miniature microscope, ribbon is replaced by MEMS magnet wire and the bottom of motor is UV glued to release the tension; (B) Controller and LabVIEW program, commercial controller is used and the LabVIEW program is developed in our research lab for micro-motor's precise motion control. The program consists of three main modules: (1) Motion command console; (2) Look-up table based system error compensation and (3) Command logging.

To characterize the transmission system, we have built a position sensing system for testing which is shown in Fig. 2.9A.

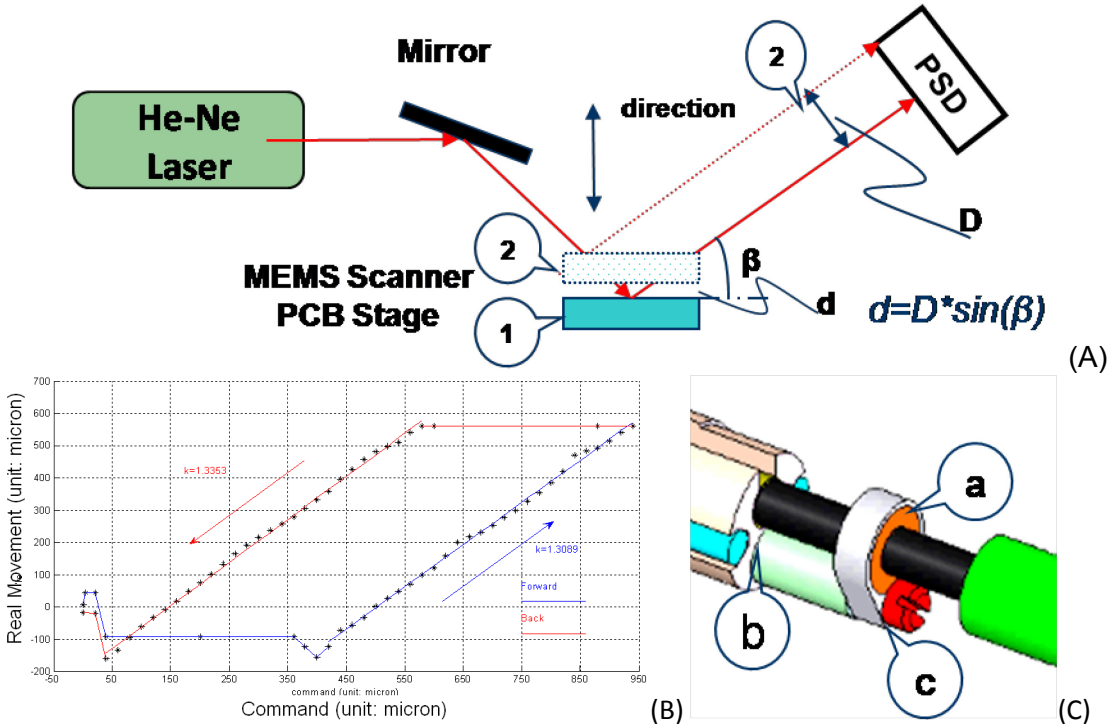

Figure 2.9 – Z-axis testing of mini-motor based axial scan mechanism. (A) Setup for testing Z-axis translational motion; (B) Performance of Z-Scan Actuator, the hysteresis of stage's motion is obvious due to imperfect mechanical assembly (20 mm/step). Errors mainly come from three places which are shown in (C) (a) Backlash, Nut and Screw Shaft, (b) Friction between mechanical guide and yoke (c) Loose screw connecting guide to shaft, RTV glue on the screw for flexibility.

Through the experiment results (Fig. 2.9B), we observe that the hysteresis is an essential problem for this miniature translational actuation system design. When the motor moves out of "dead-region", the linearity is acceptable. The resolution of micro-motor based actuator is about 2 μm which is double of optical axial resolution 4 μm. The total axial stroke is over 800 μm which is much longer than the desired Z-axis penetration depth 400 μm. The actuation system does not perform repeatable movement results because of the unstable slide friction

and unavoidable assembly error. Moreover, the simple axial scanner used in this first prototype requires a total of 25 seconds with medium speed (20 μm per second, 2.5 sec at max speed 200 μm per second) to perform the full Z-axis scan, and is not sufficiently fast to collect vertical cross-sectional images (at least 5~10 Hz for 400 μm stroke).

The micro-motor based translational actuation system can easily achieve 400μm stroke. Ideally this feature can adjust the en-face imaging depths for collection of 3D volumetric images. However, due to the slow Z-axis translational motion, the micro-motor based endoscope compatible microscope can only collect real-time horizontal cross-sectional images layer-by-layer through changing z-axis depth in stepper style. Another drawback of using micro-motor is that it is too long (> 20 mm) for miniature microscope probe. It may be possible to backside load (real clinical way) miniature microscope into the biopsy channel of GI endoscope only if total length of the microscope probe's rigid part is less than 17mm. With micro-motor, the total length of the microscope probe is over 50mm which is not practical for clinical trial. Bottleneck of the micro-motor technology is that the bulk motor structure cannot be scaled down to millimeter scale.

In vivo fluorescence images have been collected in horizontal cross-sections with the mini-motor based miniature dual axes confocal endomicroscope on human subjects at Veterans Affairs Hospital (Palo Alto, CA) [22]. The polyps area was injected with the near-infrared dye indocyanine green (ICG, Sigma-Aldrich, Inc, 785 nm excitation), which was used as a non-specific contrast agent by dissolving in distilled water at a concentration of 5 mg/ml and then diluted in

10X phosphate-buffered saline (PBS). Later, miniature dual axes confocal microscope was loaded inside the biopsy tool channel of the GI endoscope. Images were collected by the miniature dual axes confocal endomicroscope which directly contacted the surface of colon tissue, as shown in Fig. 2.10A.

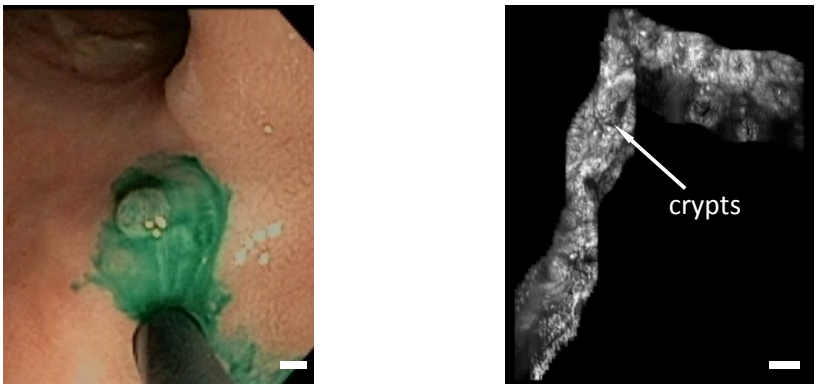

(A) Endomicroscope in human subject (B) En-face mosaicing images of colon

Figure 2.10 – (A) Miniature dual axes confocal microscope inside human body for colon In vivo fluorescence imaging, scale bar 2 mm. (B) Mosaicing images of colon in horizontal cross-section located at depth Z ~ 80 μm, scale bar 100 μm.

The tissue (polyps) was against the SIL. The miniature microscope was held statically while the thin layer of tissue is floating under it. The transverse and axial resolutions are 3 μm and 4 μm, respectively. All images were taken at 5 Hz with 2 frame averaging. The Z-Scan depth was adjusted from z=0 to 150 μm by 5 μm step. The mosaicing image of colon tissue was generated from a sequential horizontal cross-sections collected in the same plane at z=80 μm through adjusting micro-motor based translational actuation mechanism, as shown in Fig. 2.7. We cannot get vertical cross-sectional imaging because of slow Z-axis motion. The tissue is floating under the miniature microscope so that it is

impossible to reconstruct a 3D in vivo volumetric Image using stack of en-face images at different depth. Mosaicing algorithm was used to merge series of en-face images together, as shown in Fig. 2.10B.

2.1.2.2 Bulk PZT based Axial Scanning Mechanism

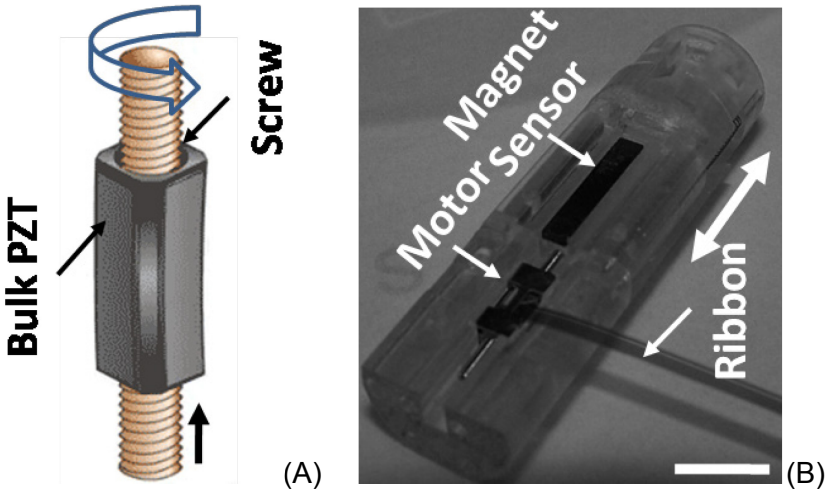

Figure 2.11 – Squiggle motor based miniature dual axes confocal microscope in OD5mm package. (A) Working principle of bulk PZT based squiggle motor. (B) Miniature OD10mm dual axes confocal endomicroscope with squiggle motor inside for axial scanning, scale bar: 5 mm.

Bulk lead zirconate titanate (PZT) material based squiggle motor (New Scale Technologies, Victor, NY, Fig. 2.11A) based translational mechanism is an alternative approach for axial scanning for miniature dual axes endomicroscope. Fig. 2.11B shows the OD10mm dual axes confocal endomicroscope package with squiggle motor driven Z-axis scanning stage. Based on the similar working principle, a squiggle motor based scanning system in OD5mm package was further developed. As shown in Fig. 2.12A, the OD5mm endomicroscope is clamped inside the aluminum v-groove for further precise optics alignment and

wiring. 3 mm travel range can be realized by moving the inner screw of the squiggle motor within one second, as illustrated in Fig.2.12B. However, fast speed (> 1 Hz) axial scanning is challenging by using squiggle motor based driving mechanism because the screw rotation is relatively slow.

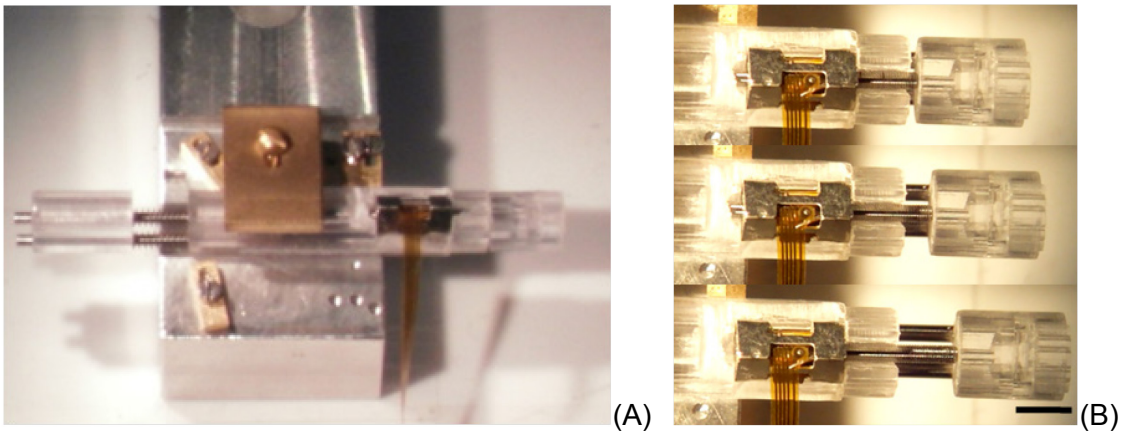

(A) (B)

Figure 2.12 – Squiggle motor based miniature dual axes confocal microscope in OD5mm package. (A) Miniature OD5mm dual axes confocal endomicroscope in V-groove holder (B) Large displacement movement performed by squiggle motor driving sliding mechanism, scale bar: 3 mm.

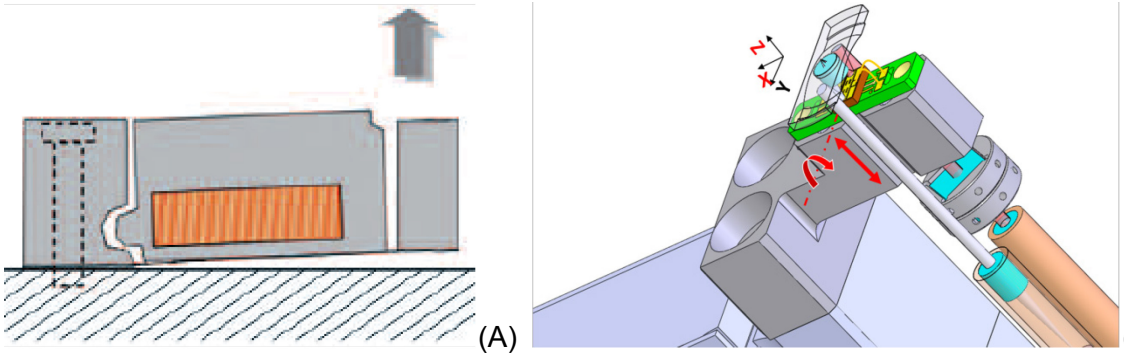

(A) (B)

Figure 2.13 – Bulk PZT Z-axis actuator in OD10mm handheld package. (A) Working principle of bulk PZT driver with mechanical amplitude amplification mechanism; (B) Integration with 1D Au-coated MEMS scanner in OD10mm package for XZ-plane scanning.

To overcome the axial scanning speed problem, we developed a novel and compact meso-scale opto-mechanical design for an axial scanning

mechanism with the bulk PZT based Z-axis actuator (P601.4SL, Physik Instrumente, Auburn, MA), Fig. 2.13A. For our application, we need to realize a raster-scanning pattern with kHz tilting speeds at 2-10 Hz frame rates over a Z-axis range of 0 ~ 400 μm. To perform axial scanning with a fast pure z-axis fast motion, we have developed a handheld “proof-of-concept” design that provides us an opportunity to study the vertical cross-sectional imaging in a miniature dual axes endomicroscope. An electro-static MEMS 1D X-axis (or 2D XY-plane, XZ-plane) resonant scanner is located in the post-objective position, and is directly integrated onto the bulk PZT based Z-axis actuator through a PCB and mechanical cantilever (Fig. 2.13B) that can be well aligned along the Z-axis and located closely to the parabolic mirror at the end. Using the “T-shape” mechanical cantilever linker (Fig. 2.13B), the scanner and its PCB are all directly mounted onto the tip of the bulky PZT based Z-axis actuator with embedded strain gauge sensor that translates the focal volume into the tissue over a range of 0~400 μm with 0 degree tilt angle (Fig. 2.13B). The MEMS mirror is secured onto the PCB with low stress silver epoxy, and while scanning in resonant mode (> 3 kHz), this device is not affected by low frequency vibrations (< 100 Hz) produced by the Z-axis actuator.

2.1.2.3 Monolithic MEMS Scanner based Axial Scanning Mechanism

For the development of ultra compact OD5mm miniature dual axes confocal fluorescence endomicroscope, we propose a novel thin-film PZT based monolithic MEMS translational/tilt micro-scanner for large FOV vertical cross-

sectional (XZ-plane) imaging. Using folded PZT unimorphs with fast response and a passive inner silicon dioxide (SiO_2) spring array, this device performs both large vertical (Z-axis) displacement and high-speed, large-amplitude tilting (X-axis during imaging). A unique "bend-up/bend-down" PZT beam design provided large Z-axis displacement. Utilizing two folded beams at the devices' four corners, the current monolithic micro-scanner performs more than double z-axis displacement and eliminates twisting about the z-axis. Meanwhile, inside a gimbal frame an inner scanning mirror supported by a passive SiO_2 spring array can perform large tilting angle amplitude using low voltage, high frequency AC excitation (< 5 Vpp) delivered through the outer PZT beams.

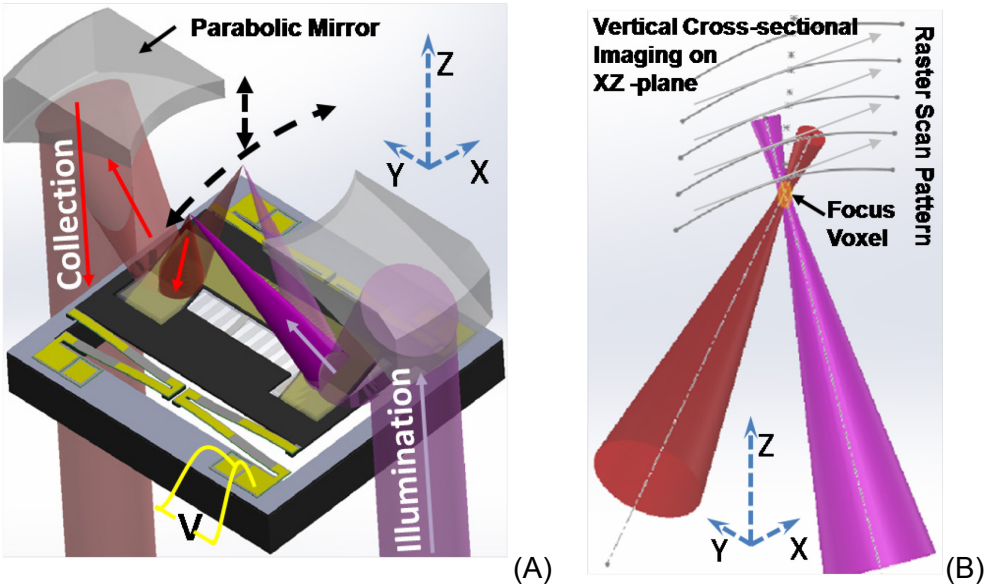

Figure 2.14 – Monolithic thin-film PZT based MEMS scanner for beam steering and axial focus scanning. (A) Schematic of XZ-plane scanhead with monolithic thin-film PZT based MEMS scanner. (B) Schematic of focus voxel in vertical cross-sectional imaging on XZ-plane with raster scan pattern.

	Electro-magnetic Mini-Motor*	Bulky Piezo Material based		Electro-static XZ-plane Resonant Scanner	Thin-FilmPZT based Monolithic Scanner	Electro-thermal Scanner[o]
		Squiggle Motor	P601.4SL			
Displacement	3~10mm	3~10mm	<500 μm	~200 μm in ambient air	> 400 μm	500 μm to 1mm
Frequency[1]	<1Hz	1~2Hz	~10Hz w/ load	~1kHz	Up to 10Hz	<1Hz
Resonant Frequency	NONE	NONE	200Hz w/o load	1~5kHz	200~500Hz	200~500Hz
Driving Voltage	<30V	>100V	>100V	>50V	<20V	<20V
Driving Current	>100mA	Low	Low	Extremely Low	Low	>100mA
Footprint	>OD 3mm	<4mm	>10mm	<3mm	<3mm	<5mm

* mini-motor is integrated with linear screw device; [o] ref [47, 48]
[1] frequency at max z-axis out of plane displacement
Table 2.1 – Comparison of different axial scanning strategies. Thin-film piezoelectric material based MEMS scanners have much better performance compared to other MEMS or meso-scale scanner/actuators with low driving voltage, extremely low current, and large (up to 500 μm) translational displacement in small foortprint.

The comparison among different scanning strategies is listed in Table 2.1. Compared with other scanners, the thin-film PZT based MEMS monolithic scanner/actuator is the future trend for miniature endomicroscope imaging system in terms of its overall performances, like low driving voltage and ultra-low current, large displacement in small footprint. Those devices based on other working principles have drawbacks in certain specs. Usually the electromagnetic minimotors or MEMS scanners require high current in a large size. The electrothermal MEMS devices [47, 48] need high driving current with low driving voltage, and limited bandwidth (< 200 Hz) because of the slow transient response time. The electrostatic MEMS devices can perform large tilting angle but has limited Z-axis displacement with large driving voltage in ambient air

environment because of the air damping. The advantage of electrostatic devices is the high yielding and relative lower cost of fabrication.

2.2 Multi-spectral Dual Axes Confocal Endomicroscope System

In this study, we will develop multi-spectral dual axes confocal endomicroscope system for intro-vital imaging on small animals. Fiber based optical system design will provide flexibility and mobility during the real-time imaging and will potentially be used for future clinical application of *in-vivo* imaging on human patient. In section 2.2.1, the development of the light sources, optics, and electronics for multi-spectral imaging will be described in general. Fiber based multi-spectral NIR laser engine will be introduced in details in section 2.2.2. Fiber based multi-spectral NIR fluorescence collection unit based on cage system will be introduced in details in section 2.2.3.

2.2.1 Multi-spectral Dual Axes Confocal Endomicroscope System Design

We adapt the light sources, optics and detectors to perform multi-spectral imaging with excitation at 671nm and 785 nm, as shown in Fig.2.15A. The optical design of the dual axes scan head uses a replicated parabolic mirror as the low N.A. focusing element. Because the collimated beams are aligned parallel to each other, the "self-aligned" parabolic mirror directs the focused beams to intersect at a common focal point below the tissue surface. This feature allows for light over a broad spectral range to become focused to the same point below the tissue surface simultaneously. Thus, the addition of a second excitation

wavelength can be used to demonstrate the use of the miniature dual axes confocal endomicroscope to study ligand-receptor interactions which is future work.

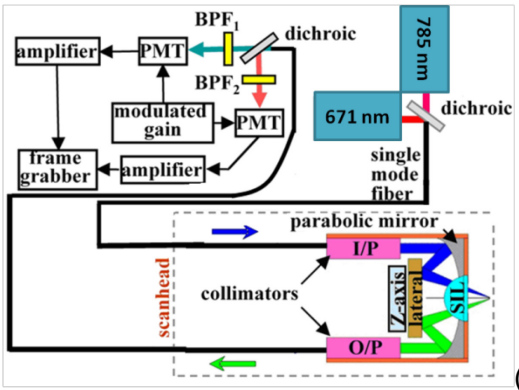

(A)

Parameters	Dual Axes	
λ (nm)	680	785
n	1.4	1.4
α	0.128	0.128
θ (deg)	24	24
FOV (μm²)	500x800	500x800
Δx (μm)	1.6	1.9
Δy (μm)	1.4	1.7
Δz (μm)	3.5	4.2

(B)

Figure 2.15 – Multi-spectral dual axes confocal endomicroscope system design. (A) Schematic of multi-spectral dual axes confocal fluorescence endomicroscope that provides excitation at 671 and 785 nm; (B) Image resolution for miniature dual axes prototypes is expected to be < 5 μm at both wavelengths, sufficient for observing sub-cellular biological phenomena.

Excitation at 671nm and 785 nm from two diode lasers will be delivered into a single mode optical fiber using a dichroic beamsplitter (FF740-Di01-25x36–45°, Semrock,Rochester, NY), and focused into the tissue using the same optics in the dual axes scan head. Fluorescence in both spectral bands is collected off-axis, focused into another single mode fiber, and split by a second dichroic. A band-pass filter (BPF1, 690 to 720 nm) (BPF2, 805 to 845 nm) is placed in front of each photomultiplier tube (PMT, H7422-40 and -50, Hamamatsu, Japan) for separate detection of fluorescence from the two excitation sources, respectively. The gains are separately modulated to achieve appropriate amplification of the fluorescence signal from the deeper regions of tissue. The image resolution in the transverse and axial dimensions for the dual axes architecture with uniform

illumination can be determined from diffraction theory, and is given as the FWHM in Fig. 2.15B.

We will acquire vertical cross-sectional images with a tissue penetration depth > 400 μm and lateral field-of-view > 800 μm. Because we expect a transverse resolution of ~ 5 μm in real imaging, the fluorescence image will be digitized to 420 x 270 pixels, which is oversampled by a factor of 2 to meet the Nyquist criteria. A high speed, 8 channel, 12 bit data acquisition board (PCI-5105, National Instruments, Austin, TX) that can digitize 60×10^6 pixels/sec per channel will be used. At this rate, two fluorescence images can be acquired at speeds up to 30 Hz, which easily exceeds our goal of 10 Hz. The vertical cross-sectional images have a high dynamic range (> 40 dB), and will be digitized to 12 bits at 10 frames per sec, limited by the gain-settling time of the PMT. A high speed analog output board (PCI-6711, National Instruments,Austin, TX) will generate the waveforms needed to drive the scanning mirror, and will provide the triggers for the data acquisition board.

2.2.2 Multi-spectral Near Infra-red Laser Engine (671nm and 785nm)

For multi-spectral targeted vertical cross-sectional imaging, we developed low-cost fiber based NIR multi-spectral laser engine for illumination. The laser system is essentially The laser engine consists of 671 nm and 785 nm continuous wave (CW) solid-state diode lasers and pigtail single mode fiber (S630-HP, Nufern, Granby, CT) coupled wavelength-division multiplexing (WDM) beam combiner component. The NIR 785 nm laser system has been coupled by

permanent pigtail fiber with FC/PC connector end. The 300 mW output 671 nm laser is a free space system which is fiber coupled into the WDM with FC/PC connectors, in Fig. 2.16.

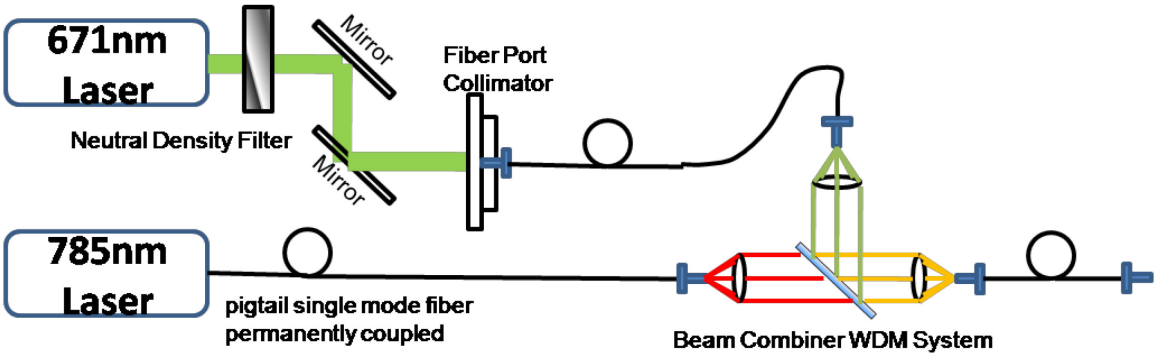

Figure 2.16 – Multi-spectral near infra-red (671 nm & 785 nm) laser engine design. 300 mW free space 671 nm CW laser is fiber coupled into a single mode fiber, and then combined with 40 mW 785 nm CW laser using fiber coupled WDM system.

We have performed two different coupling for the 671nm laser, shown in Fig. 2.17. The U bench (F-915T & FP-2A, Newport, Irvine, CA) objective lens (MV-10X, Newport, Irvine, CA) based coupling, in Fig. 2.17A, is utilized for single mode fiber with bare end on one side. Another end is FC/PC connector that is butt-coupled to the FC/PC connector of WDM beam combiner. Fiber port collimator (PAF-X-15-PC-B, Thorlabs, Newton, NJ) based coupling system is shown in Fig. 2.17B. The FC/PC connector of WDM beam combiner is directly connector on the fiber port end. Compared with the approach in Fig. 2.17A, the power loss of fiber port collimator based coupling system will be slightly smaller with minimum contact damage. In the future, FC/APC connector will be used for the coupling system to reduce the reflective light influence.

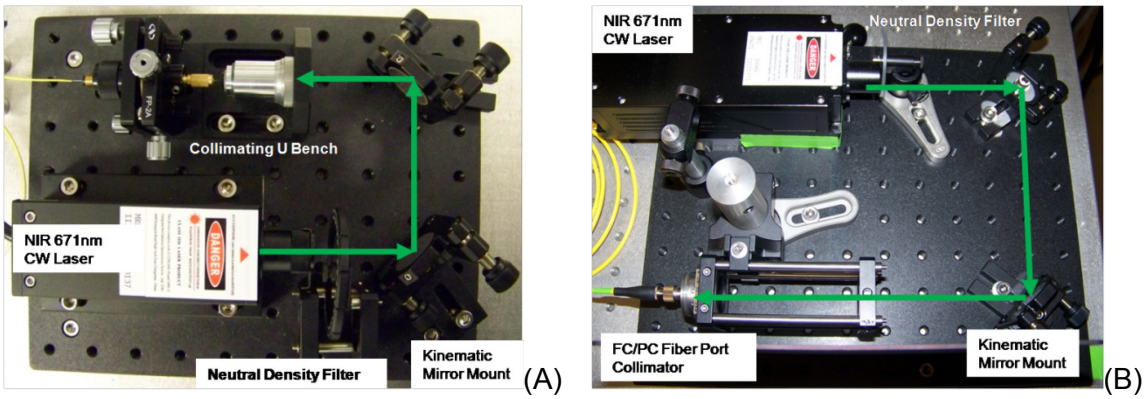

Figure 2.17 – NIR fiber coupled 671 nm CW laser system. (A) Collimating U bench based fiber coupling system; (B) Fiber port collimator based coupling system.

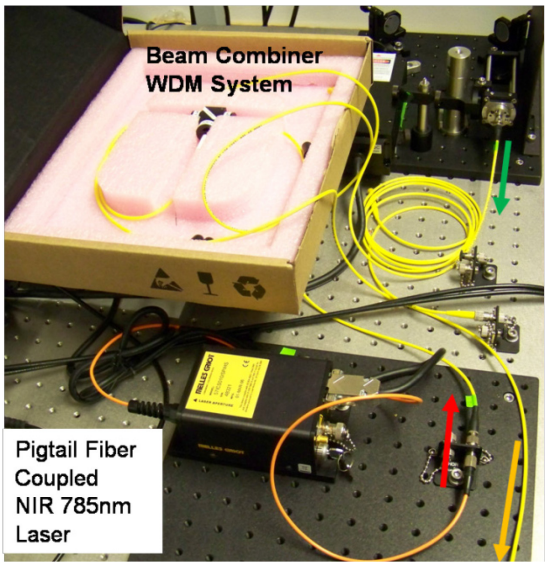

Figure 2.18 – Multi-spectral NIR laser engine setup and layout. Fiber based WDM beam combiner system is used to combine 671 nm (green color arrow) and 785 nm (red color arrow) laser system. The output (yellow color arrow) laser illumination power is delivered to the fiber coupled dual axes confocal endomicroscope with butt-coupled FC/PC fiber connectors.

The final fiber coupled multi-spectral NIR laser engine is shown in Fig. 2.18. The pigtail permanent fiber coupled NIR 785 nm laser (57ICS010/SP/HS, Melles Griot, Carlsbad, CA) is directly connected to WDM with butt-coupling. The dichroic mirror combines the 671 nm and 785 nm wavelength inside the WDM beam combiner. Then the multi-spectral beam is coupled into the single mode

output fiber. With the fiber coupling design, the system can be compact and expended to 4-color laser engine system in the future. The light will be delivered from the FC/PC connector end of WDM to the fiber based dual axes confocal endomicroscope imaging system with butt-coupling.

2.2.3 Multi-spectral Fluorescence Collection Unit

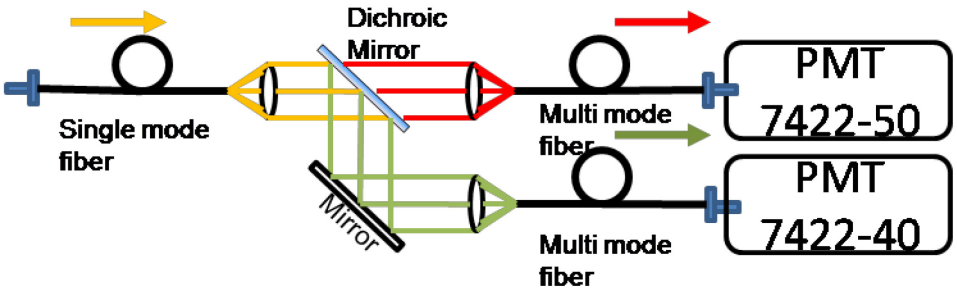

Figure 2.19 – Multi-spectral NIR fluorescence collection unit design.Fluorescence signal is split into two collimated beams by a dichroic mirror. One channel is the emission light by 785 nm excitation; the other channel is the emission light by 671 nm excitation. Each beam is coupled into multi-mode fiber that connects to PMT.

For the fluorescence collection end of multi-spectal dual axes confocal fluorescence endomicroscope, we developed cage-system based and fiber coupled multi-spectral fluorescence collection unit. As shown in Fig. 2.19A, the collected fluorescence light is split to two separate beams, filtered and coupled into the multi-mode fibers. The multi-mode fibers will be connected directly to the photomultiplier tube (PMT) units. The 680 nm fluorescence light will be collected by a PMT (H7422-40, Hamamatsu, Middlesex, NJ). The 800nm fluorescence light will be collected by a PMT (H7422-50, Hamamatsu, Middlesex, NJ). The single mode fiber on the collection end of the dual axes confocal endomicroscope works as the function of pin-hole in the conventional free space

confocal microscope. The fluorescence collection unit can be expended to 4-color system in the future because of its scalability. The fiber coupled cage-system based collection unit design, shown in Fig. 2.20, is not sensitive to the ambient light at all. Such open-housing design will help build a practical fluorescence collection unit for clinical trial in the future. The current output of PMTs (H7422-40 and -50) are converted by low noise high impedance amplifiers (Femto, Germany) to voltage and fed to the multi-channel data acquisition card.

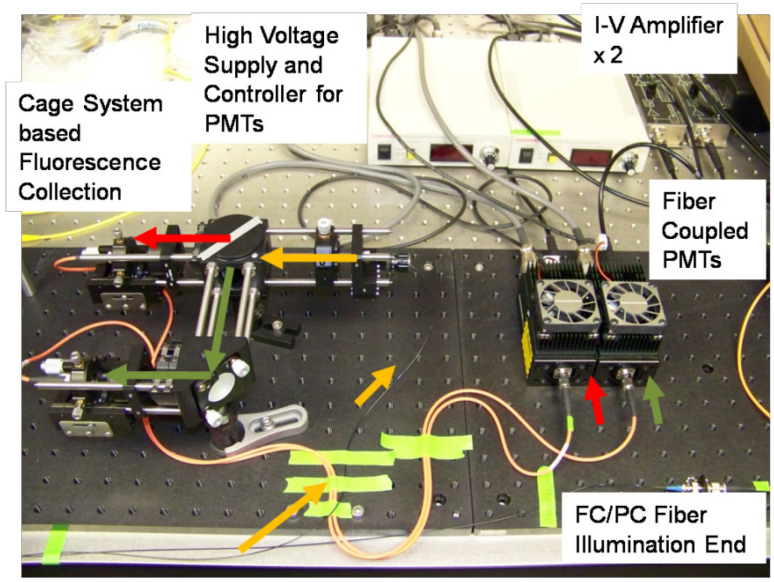

Figure 2.20 – Multi-spectral NIR (671 nm & 785 nm) fluorescence collection unit setup and layout.

2.3 Phantom Design for System Characterization

The use of phantoms is becoming increasingly important, especially when the optical system should be used for medical detection and diagnosis progress toward clinical utility. Till now, there is no existing standard phantom design matching the requirement of our real-time vertical cross-sectional imaging system.

Most of optical calibration targets (e.g. 1951 USAF) are only 2D surface machined device for *en-face* imaging characterization in reflectance mode. Fluorescent beads usually are commercially available for 488 nm to 650 nm range. We will develop a 3D phantom with near-infrared fluorescence conjugated beads (shown in Fig. 2.21) for the vertical cross-sectional multi-spectral fluorescent imaging system characterization. First, certain polymers which can mimic the scattering properties of human tissue will be considered as candidates for the phantom design. To validate the fabrication process, low-cost commercial fluorescent beads (e.g. FITC, excitation 488 nm) will be mixed with polymer precursor. In our study, we mix the Cy5.5 dye labeled fluorescent beads (FluoSpheres® Polystyrene Microspheres, 15 μm, Invitrogen, Grand Island, NY) with PDMS (10:1 ratio, Dow Corning).

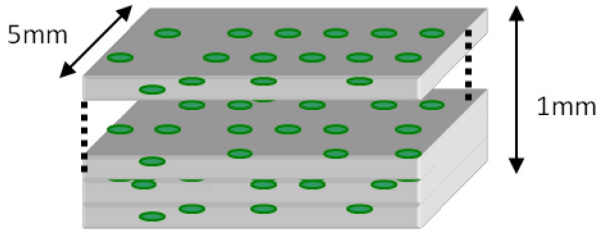

Figure 2.21 – Schematic of 3D phantom for vertical cross-sectional imaging characterization. Fluorescent beads are mixed inside the cubic phantom, not in scale.

Chapter 3

Miniature Scan Engine Development

We have developed several miniature XZ-plane scan engines to perform real time vertical cross-sectional imaging with tissue penetration depth up to 400 μm in a miniature dual axes confocal endomicroscope. To our best knowledge, there is very few MEMS XZ-plane scanner/actuator for vertical cross-sectional imaging in miniature imaging system. For proof-of-concept, we first developed 1D X-axis and 2D XY-plane electrostatic resonant scanners for *en-face scanning*, which can be integrated with bulk PZT based actuators for axial (Z-axis) scanning in a handheld dual (outer diameter < 10 mm) axes confocal endomicroscope imaging system. For the package that is further scaled down in size (outer diameter < 5 mm), we developed novel electrostatic 2D MEMS XZ-plane resonant scanner and thin-film piezoelectric materials based monolithic MEMS XZ-plane scanner. We are packaging those new monolithic MEMS XZ-plane scanners into OD5mm instrument for future *in-vivo* imaging.

3.1 Introduction

For fast lateral scanning in the XY-plane (*en-face* imaging), a 2D scanner was previously developed by our collaborators at Stanford University and integrated into the miniature dual axes confocal imaging system [22, 23, 49]. The scanner design uses a gimbal geometry to perform scanning for collecting horizontal (XY-plane) cross-sectional images, and rotation around an inner and outer axes defined by the location of the respective torsion springs, as shown in Fig. 3.1A. Fabrication (shown in Fig. 3.1B) of this 2D MEMS scanner, driven by staggered vertical comb-drive (SVC), involves four-mask, four DRIE steps and accurate alignment is important in minimizing failures due to electrostatic instability during high voltage actuation. The scanner's basic performance is listed in Table. 3.1. However, wafer bonding with low stress and 4-mask multiple DRIE process with critical alignment requirement are not suitable for mass production application. In addition, high driving voltage is required for the scanner at both DC static and AC resonant scanning mode. The parametric resonances [50, 51] can sometimes be observed in the inner axis near frequencies of $2\times f_0/N$ (f_0: resonant frequency, N: an integer ≥1).The previous 2D XY scanners [22, 49] design suffers from a frequent device failure and low manufacturing yield (< 5%) due to the relatively complex design that demand a fabrication process that requires feature alignments with extremely high precision, leading to manufacturing errors, poor reliability, and low yield. High yield and reliability are key factors for endomicroscope imaging system. The development of 1D MEMS X-axis resonant scanner will be introduced first in section 3.2.2. Then 2D XY-plane and XZ-plane resonant scanners will be described in section 3.2.3.

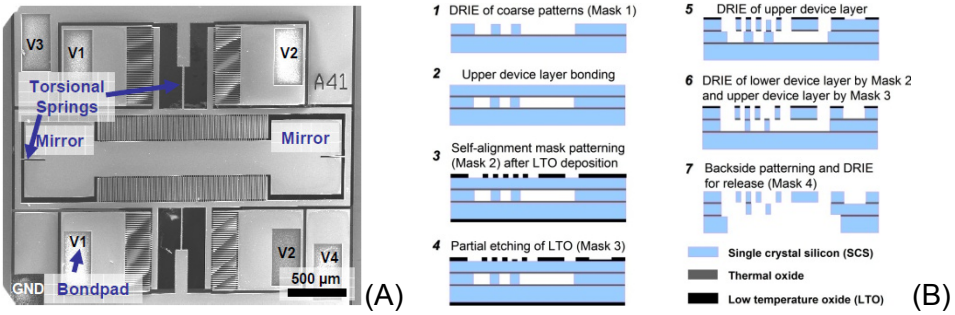

Figure 3.1 – 2D electrostatic MEMS scanner with staggered vertical comb-drive. (A) SEM of a gimbaled, two-dimensional XY MEMS scanner driven by staggered vertical comb-drive (SVC) actuators with resonance frequencies determined by the inner and outer springs and provides lateral scanning in the XY-plane. (B) Process flow for fabrication of the MEMS scanner [22, 49].

Maximum Field-of-View (FOV)	**Reflectivity of Mirror Surface w/o Al coating**	**Reflectivity of Mirror Surface w/ Al coating**	**roughness of mirror surface**	**Optical deflection of outer axis**		**Optical deflection of inner axis**	
800x400µm^2 (XY, en-face imaging)	37 % (at visible wavelengths)	74 % (at visible wavelengths)	~25 nm **root mean square (RMS)**	±12.4° res. freq 500Hz	±4.8° Static	±7.2° res. freq. 2,9kHz	±5.5° static

Table 3.1 – Performance summary of the two-dimensional XY-plane MEMS micro-mirror driven by staggered vertical comb-drive (SVC) actuators [49].

For the vertical cross-sectional imaging application, we will take advantage of the parametric resonance to develop resonant scanners with large tilting angle (XY-plane) and large displacement (Z-axis) at low driving voltage. Robust fabrication process will be developed for good reliability and high yield (up to 80%), which is important for integration into miniature endomicroscope imaging system. We propose a parametrically excited resonant scanner based on in-plane comb-drive configuration which will simplify the electrostatic scanner design for one dimensional (X-axis) and two dimensional (both XY-plane and XZ-plane, lissajous scan pattern) scanning. The resonant scanner is lack of DC static scanning capability. However, for our *in-vivo* imaging application, DC static scanning is not necessary for high-speed lateral scanner. The Z-axis static

scanning will be realized by thin-film PZT based actuator. An alternative way for 2D XY-plane or XZ-plane imaging is to use 2D lissajous scan pattern by resonant scanning on both axes. To perform real-time vertical cross-sectional imaging, we first developed a fast lateral scanning MEMS scanner that complements the Z-axis actuator. With use of post-objective scanning in the dual axes architecture, we can achieve a very large field of view (> 800 μm). This level of performance requires a robust, high speed lateral scanner for use in live animal imaging in colon.

3.2 Electrostatic MEMS Resonant Scanner

The major technological challenge of electrostatic scanner design is to achieve both a fast scanning speed (high dynamic bandwidth) and a large optical deflection angle (optical scan angle ±12º for 800 μm FOV in our application). In addition, we hope that by simplifying the scanner design, we will also improve the reliability and fabrication yield. The 1D X-axis and 2D XY resonant scanners can be integrated with compact Z-axis scanner for handheld and miniature imaging system, while the 2D XZ-plane resonant scanner will enable vertical cross-sectional imaging with dual axes confocal endomicroscope in a miniature OD5mm package for *in-vivo* imaging in small animals and humans in the future.

3.2.1 Parametric Resonance Working Principle

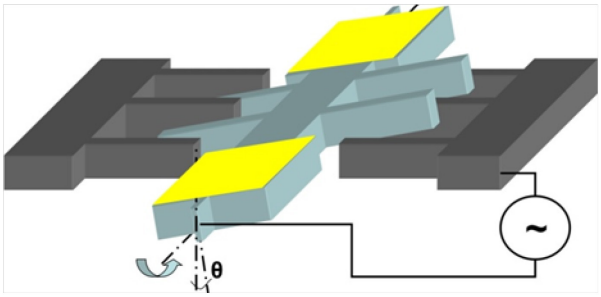

Figure 3.2 – Parametrically excited MEMS resonant scanner working principle. AC voltage will be added to two sides of comb-drives. The mirror is developed using in-plane comb-drive configuration.

To overcome these issues and meet the performance requirement, we developed afast scanning (> 3 kHz) comb-drive actuated electrostatic resonant scanners. Our primary aim will be focused on obtaining vertical cross-sectional images in tissue at high scan speeds. Our new scanner designs employ a parametrically excited driving mechanism [50], shown in Fig.3.2. Parametric resonance is an effect that causes maximum oscillation by certain driving frequencies ($f_{driving} = 2 \times f_0/N$, N: an integer $\geqslant 1$, f_0: torsional resonance frequency) to a non-linear mechanical system, where a periodic force acting upon a mechanical structure varies in both time and displacement.Similar non-linear phenomena have been observed for photons in photonic crystals [52], electrostatically forced nanowires [53], optically trapped atoms [54] as well as for MEMS resonator devices [55].

3.2.2 One-dimensional MEMS Resonant Scanner

3.2.2.1 X-axis MEMS Resonant Scanner Design

The proposed 1D device structure consists of a patterned Au-coated (for > 90% reflectivity at NIR wavelength range) movable silicon plate mirror that has dumbbell contoured reflective surface, according to the dual axes architecture shown in Fig. 2.1, a fixed frame that includes two flexure beams which connect the mirror plate to the frame, and comb-shaped electrodes on the sides of both the middle of the mirror and the frame, shown in Fig. 3.3. The surface geometry and dimensions of the mirror plate are primarily determined by the current packaging design of the miniature dual axes scan head. The flexure beams serve as torsional springs to provide a restoring torque against the rotation of the mirror. A rectangular AC waveform driving voltage signal will be applied to the comb-drives. Compared to other waveform, like sine or triangle ones, the advantage of using rectangular AC waveform driving is that it can be realized in a relatively simpler analog driving circuit. In our process, there will be no comb-drive's misalignment problem which is always the key challenging issue for SVC scanner fabrication with multiple etchings and wafer bonding process. Two DRIE steps on front and backside Silicon will make the fabrication quite reliable and stable, also higher the yield.

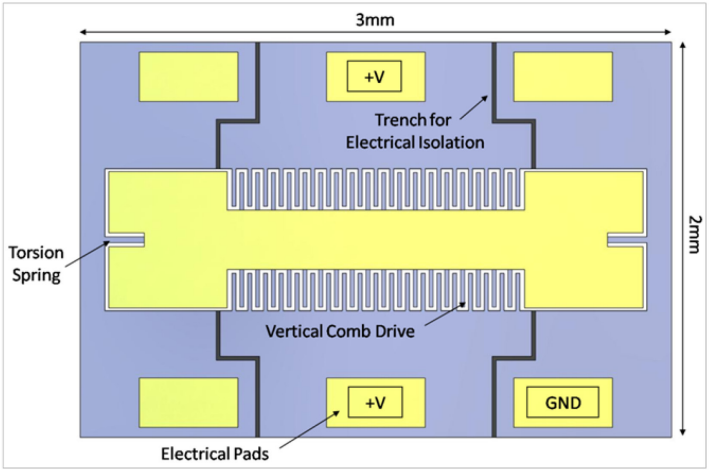

Figure 3.3 – Schematic of the 1D MEMS scanner with in-plane comb-drive configuration. Both moving and static comb-drives actuators are on the same plane in geometry, not in scale. High-speed lateral scanning micro-mirror operated in the non-linear regime as a parametric resonator. This MEMS scanner has a small device footprint (3.0 × 2.0 mm^2) that is well suited for integration into the dual axes scan-head. Both sides of the outer static comb-drive actuators will be connected to same potential voltage +V, the inner mirror will be connected to GND analog signal. Trench on the device will isolate the mirror area out of AC driving region.

Any tiny asymmetry on the structure caused by imperfect fabrication process (i.e. mechanical structure neutral plane will not overlap that of electrical field) will trigger the scanner to tilt at mechanical resonant frequency while the design is fully symmetrical. The dimensions of the torsional springs are selected to be on the order of 200 μm in length, 5 μm in width, 30 μm in thickness (thickness of device Si on Silicon-On-Insulator wafer) to yield the maximum rotational angle at the desired scanning frequency for the given mirror structure. The mechanical torsional resonant frequency will be ~ 3 kHz based on those parameters. Theoretically, the structure experiencing parametric resonance has multiple driving frequencies $f_{driving} = 2 \times f_0/N$ located near integer fractions of twice the natural (e.g. mechanical) resonance frequency f_0. Here, we will excite the first mode of parametric resonance corresponding to N = 1 for our device.

Operational conditions ensuring the dynamic stability of parametric resonators are determined by a combination of the drive voltage and the drive frequency. The MEMS mirror will be operated under an optimal condition that leads to stable scanner oscillations with a time-invariant vibrational amplitude. To make this behavior happen, we will identify the optimal condition by carefully modulating the drive voltage and frequency prior to the operation. Large rotational angle (mechanical scan angle > ± 6º) can be achieved by reducing the torsional stiffness of the flexure beams or tuning driving frequency around the peak. Lower dynamic bandwidth resulting from the lower stiffness normally reduces the speed of conventional MEMS scanners operated in the linear regime as simple harmonic oscillators. In contrast, the parametric resonance mode occurring at the driving frequency twice the natural frequency can counterbalance the speed loss. Usually, air damping in atmospheric operations limits the upper bound (e.g. n >= 3) for the rotational angle range. In addition, it can achieve a mechanical rotational angle more than ±12º optical deflection at a driving frequency close to 6 kHz ($f_{driving}$ = 2×f_0, when f_0 is 3 kHz) for MEMS parametric resonators experiencing atmospheric air damping. Therefore, there is no need for special low-pressure or vacuum device packaging in this prototype.

3.2.2.2 Fabrication Process

The tilting mirror in the 1D resonant scanner requires an open area on the backside, which is realized with an advanced deep reactive-ion etching (DRIE, Deep Silicon Etcher, STS Pegasus 4”, SPTS, San Jose, CA) process with high

aspect ratio and steep side walls. With the in-plane vertical comb-drive configuration [55], MEMS resonant scanners require only a “3-step process” (Fig. 3.4) using a 4-inch silicon-on-insulator (SOI) wafer (device silicon/buried oxide/handle silicon layer: 30/2/500, unit: μm), including: (a) patterned gold coating on the top side of device silicon for reflective mirror surface and electrical pads, (b) DRIE on the top silicon layer for vertical in-plane comb-drive actuators and mirror’s hinges, (c) DRIE on the bottom layer for an opening hole and buffered oxide etch (BOE) for releasing the tilting mirror.

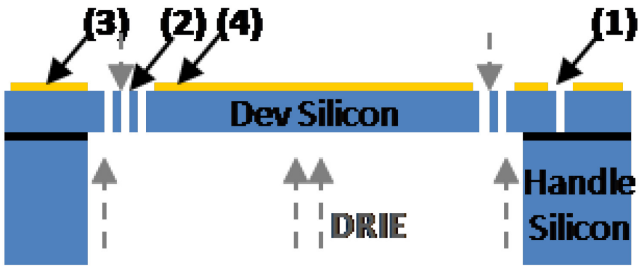

Figure 3.4 – Process flow for MEMS 1D (X-axis, lateral scanning) resonant scanner. (1) Electrical isolation trench; (2) Comb-drive actuator or torsion spring silicon beam; (3) Electrical pads; (4) Patterned Au/Ti coating for high reflectivity for NIR range (> 90%).

During post-processing, each module (around 20 × 20 mm^2) is diced (ADT 7100 Dicing Saw, Horsham, PA) from the SOI wafer with 5 μm photo-resist protection on the top side of the device silicon layer. Then, the protection photo-resist is removed by reactive-ion etching (RIE, LAM9400, LAM Research, Fremont, CA). Each device is dry-released from the module by breaking off the link-arm struts with laser cutting (or tweezers). With the simple robust fabrication and fully dry post-process, the new application-driven MEMS scanner design and

its fabrication process guarantee a high device yield (> 90%). The mirror surface is first coated with a 10 nm layer of Cr followed by a 120 nm layer of Au, for enhanced reflectivity (> 85%, 640-785 nm) in the NIR. The MEMS devices are all developed in the Lurie Nanofabrication Facility (LNF) at the University of Michigan.

3.2.2.3 Characterization

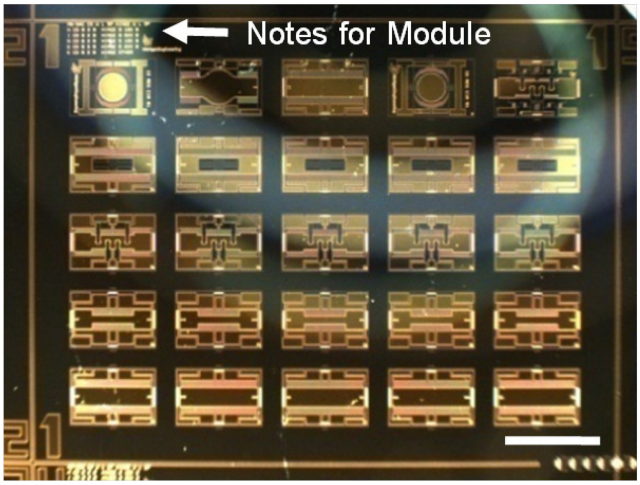

Figure 3.5 – Stereomicroscope image of 1D MEMS scanner module, scale bar: 3mm. 5 different designs are proposed in one module for comparison. The yielding is > 80%.

We have developed the 1D MEMS resonant scanner for X-axis lateral scanning using a working principle based on electrostatic, parametric resonant tilting [50, 55] to achieve a scan angle greater than the desired optical scan angle (OSA) ±12 degrees with a low drive voltage (< 40 V) in a small 3 × 2 mm^2 footprint. Single module of twenty-five 1D MEMS resonant scanners is shown in Fig. 3.5. Each device is released by dicing-free dry process from the module by breaking the link arm on the edge, Fig. 3.6. The tilting mirror steers the two

overlapping beams (illumination and collection) together over the FOV with a geometry that has a high fill-in factor of 90.3% (2.71 mm / 3 mm, the width of mirror surface is 2.71 mm, the width of MEMS chip is 3 mm) in the lateral dimension of the device (Fig. 3.6).

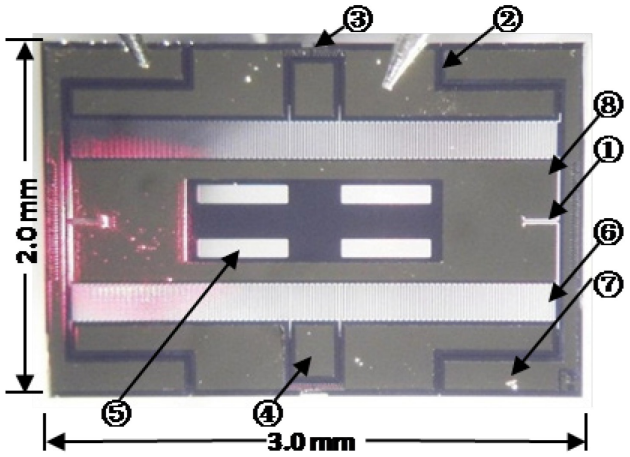

Figure 3.6 – Stereomicroscope image of MEMS 1D (X-axis) resonant scanner. Red spot represents reflected He-Ne (633nm) laser beam from gold coated reflective surface. Components: (1) Hinge; (2) Electric isolation trench; (3) Link-arm struts; (4) Sensor pad; (5) Four weight-reducing holes; (6) Electrostatic comb-drive actuators; (7) Electric Au/Cr pad; (8) Au/Cr coated reflective mirror surface.

The response curve and phase shifting of the MEMS resonant scanner are shown in Fig. 3.7A. Dynamic stable region of the 1D MEMS scanner, starting and stop frequencies versus different driving voltage, is shown in Fig.3.7B. The mirror is excited to start tilting and reaches the peak amplitude by sweeping the pulse width modulation (PWM, 0 to 50%, with 10% step size) of a square waveform in 1.0 sec initiation time by fixing the drive frequency at a desired value for imaging. With parametric resonance, the mirror is driven by a square waveform (50% duty cycle) with drive frequency $f_{driving} = 2 \times f_{res}/N$ (N = 1,2,3,…, in

ambient air, we use N=1). For example, the resonant frequency of the tilting mirror is 3010 Hz at a drive frequency of 6020 Hz, $f_{res} = f_{driving} \times N/2$, N=1). Meanwhile, synchronization of the phase between the driving waveform on X-axis and Z-axis, which is the key for vertical cross-sectional imaging at fast frame rates, is achieved using custom LabVIEW (National Instruments, Austin, TX) software.

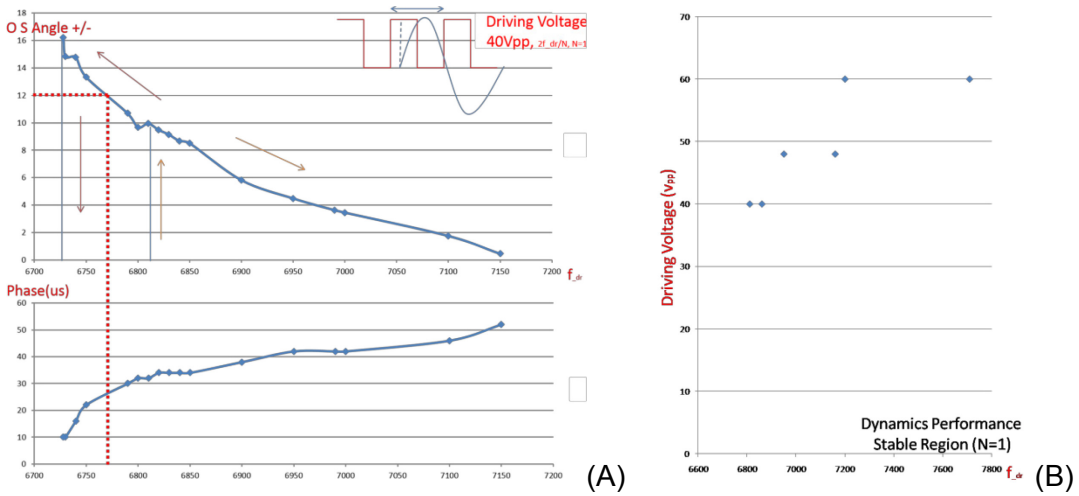

(A) (B)

Figure 3.7 – MEMS 1D (X-axis) resonant scanner characteristics. (A) Optical scan angle versus driving frequency (upper image); phase shift versus driving frequency (bottom image); (B) Stable region of the scanner.

3.2.3 Two-dimensional MEMS Resonant Scanner

3.2.3.1 XY-plane MEMS Resonant Scanner Design

Based on the parametric resonance working principle, we also designed 2D MEMS XY-plane resonant scanners for *en-face* imaging, Fig. 3.8. The small footprint (3.2 × 2.9 mm^2) will fit the miniature dual axes confocal fluorescence endomicroscope in OD 5mm. Integrating the 2D scanner for *en-face* (XY-plane)

imaging with a bulk or thin-film PZT based scanner for Z-axis focusing [45, 56], the miniature endomicroscope will acquire 3D volumetric images.

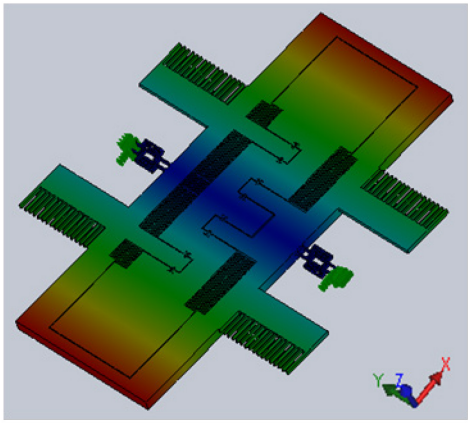

Fig.3.8 – 2D XY-plane MEMS resonant scanner design 3D schematic in Solidworks.

Large tilting angle at high-speed can be realized by this device (3.2 × 2.9mm^2) that has a high fill-in factor (up to 90% on the X-axis in Fig. 3.8) scanning mirror supported in a gimbal frame driven by two electrostatic-comb drive actuators on each axis. An alternative electrostatic vertical staggered comb drive based 2D microscanner in [22, 49] demonstrated a comparatively small tilting angle (corresponding to FOV 362 x 212 μm^2) while requiring higher voltage.

Simulation of mechanical resonant vibration mode is shown in Fig.3.9. The first torsional mode of inner and outer axes will be used for XY-plane *en-face* imaging, with a lissajous scan pattern.

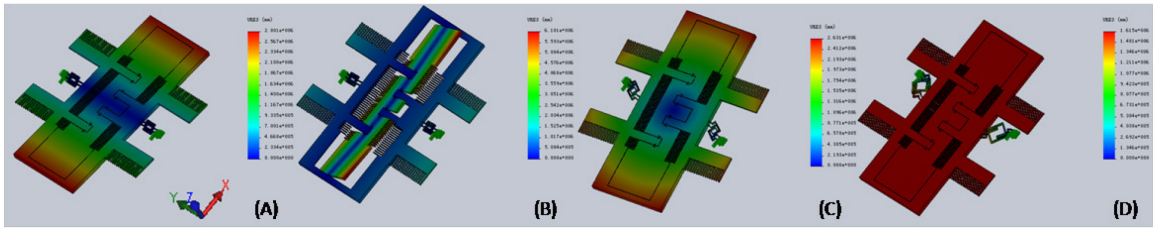

Figure 3.9 – 2D XY-plane MEMS scanner FEM simulation in Solidworks, showing mechanical vibration eigen modes. (A) Outer spring tilting mode; (B) Inner spring tilting mode; (C) Outer 2nd vibration mode; (D) Outer 3rd piston mode; higher eigen frequency modes are not shown here.

3.2.3.2 XZ-plane MEMS Resonant Scanner Design

The 2D resonant vibration modes will enable the lissajous scan pattern on XZ-plane as well. For vertical cross-sectional imaging, we designed a 2D MEMS XZ scanner with leveraging beam based mechanism on the outer frame and inner torsional mirror. The schematic design is shown in Fig.3.10A (inner torsional tilting mirror is not shown), with a mask drawing (AutoCAD 2010, Autodesk, San Rafael, CA) in Fig.3.10B.

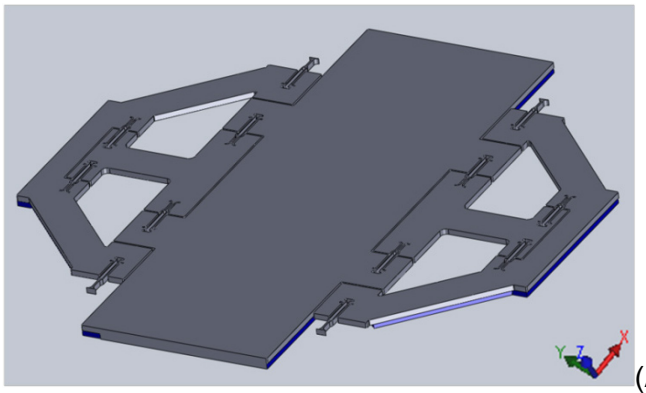
(A)
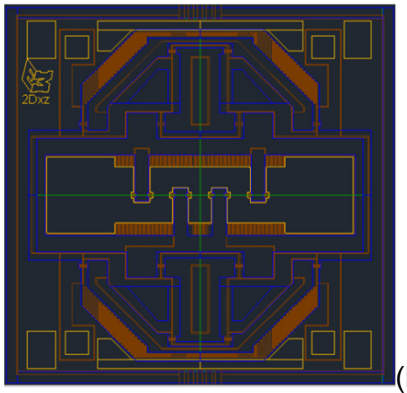
(B)

Figure 3.10 – 2D MEMS XZ-plane resonant scanner design. (A) Schematic of the XZ-plane resonant scanner, inner X-axis tilting mirror is not shown in the illustration; (B) Mask CAD design of the 2D MEMS XZ-plane resonant scanner (Autocad).

FEM simulation has been performed in Solidworks to verify the XZ scanning design, shown in Fig.3.11. Simulation in Ansys software was also performed for comparison. We can find similar frequency value for different vibration modes. For example, the 1st mode is 1123 Hz in Ansys compared to 1107 Hz in Solidworks software. We carefully design the Z-axis mechanism so that the translational motion can be realized at the 1st vibration mode while other tilting mode is separated far away from it.

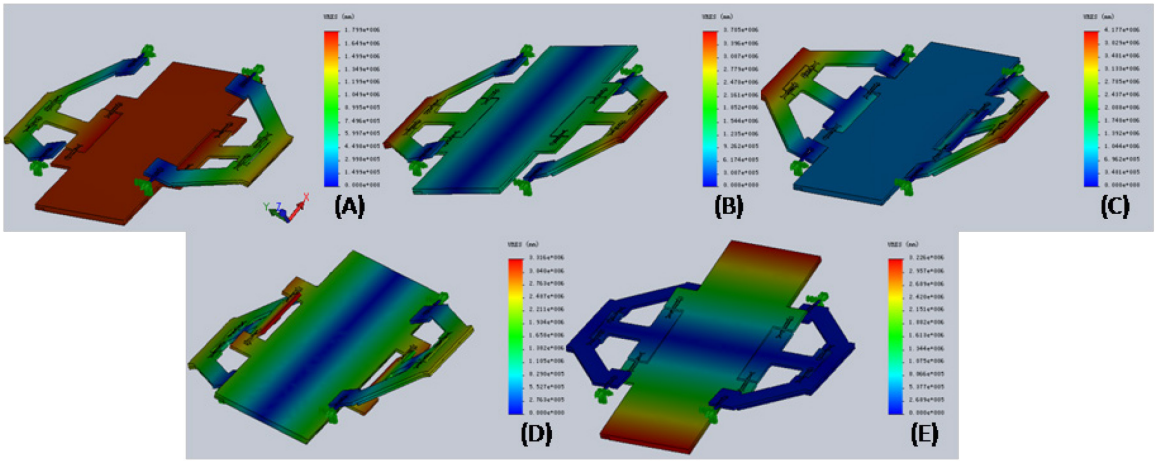

Figure 3.11 – 2D XZ-plane MEMS resonant scanner FEM simulation in Solidworks, mechanical vibration eigen mode. (1st to 5th resonant mode: 1107, 1657, 2563, 3810, 4133 unit:Hz, Ansys simulation results are similar, i.e. 1st mode 1123Hz, 2nd mode 1622Hz.)

3.2.3.3 Fabrication Process

Compared with the 1D MEMS scanner, the 2D MEMS scanner design requires backside structure for the tilting gimbal frame. A robust and high yield (> 80%) four masks, three-step (frontside, backside 2-step etching) DRIE etching SOI process has been developed for the fabrication, as shown in Fig. 3.12, and a 4-inch SOI wafer with 35 μm silicon device layer, 1μm buried oxide layer and

500μm silicon handle layer is used. A patterned 120nm gold (Au/Cr) layer is coated for electrical pads and reflective surface on the tilting micro-mirror (650 x 600 μm^2 on each side). With the gold coating, we can achieve high quality reflective surface (>90% reflection efficiency at near infra-red range). Backside hard mask is prepared by two steps, LPCVD SiO_2 and PECVD SiO_2. Then frontside comb-drive and isolation trench are realized by DRIE. Later, the SOI wafer is diced into modules for post-processing, Fig 3.12H. Two step etchings (Fig. 3.12I&J) are performed on the backside for islands and backside enhancement for torsional tilting mirror flatness, Fig. 3.12K.

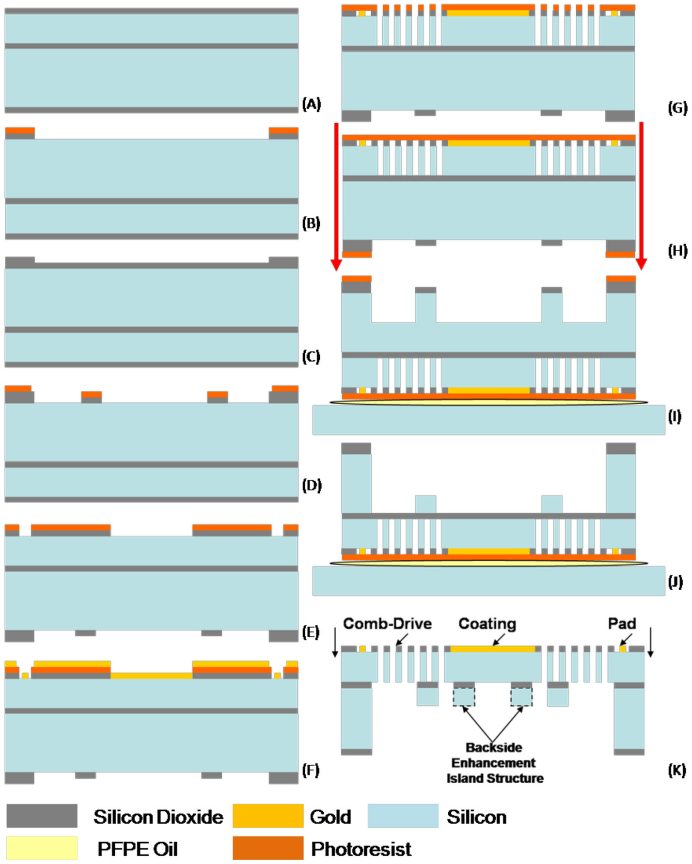

Figure 3.12 – Process flow of 2D XY-plane and XZ-plane MEMS resonant scanners.

3.2.3.4 Characterization

Stereomicroscope image of the MEMS 2D XY-plane resonant scanner module is shown in Fig. 3.13. Fig. 3.14A shows the stereomicroscope images of the 2D MEMS XY-plane scanner in OD 5mm package and detailed structural features (different hinge design) shown in Fig.3.14B&C. The curvature and the surface roughness of the inner scanning mirror's reflective surface are measured by a Zygo optical surface profiler (NewView 5000, Zygo, Middlefield, CT). The measurement shows that the mirror has a radius of curvature of ~ 1.7 m and a RMS roughness of ~ 2 nm, providing a high optical quality. Similar design with aluminum coating is shown in Fig.3.16A, with SEM images of detailed features shown in Fig.3.16B-E.

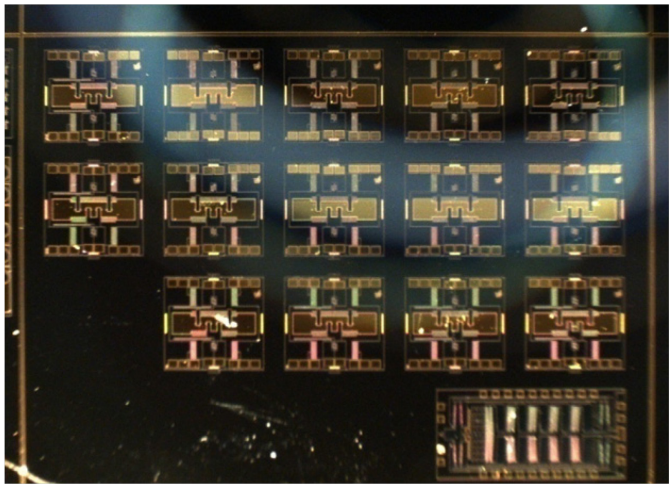

Figure 3.13 – Stereomicroscope image of the 2D XY-plane MEMS resonant scanner module.

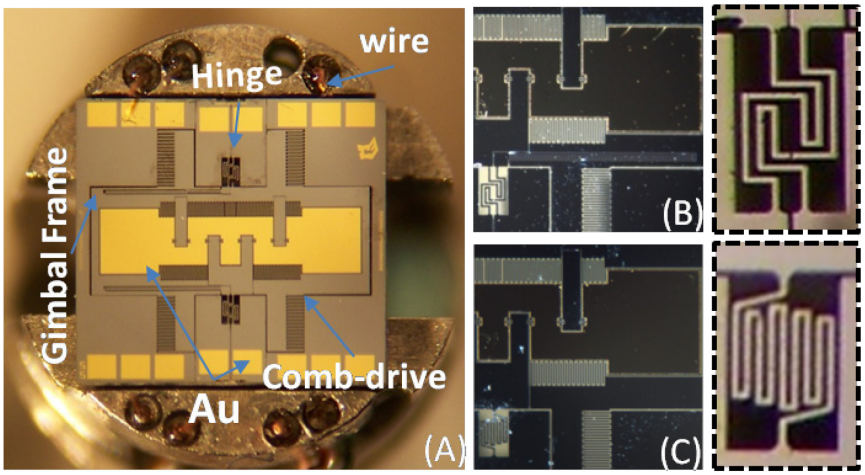

Figure 3.14 – 2D XY-plane MEMS scanner for NIR imaging. (A) Stereomicroscope image of 2D XY-plane MEMS Au coated scanner inside OD5mm packaging; (B) "Loop" shape hinge design; (C) "Zig-Zag" shape hinge design.

In Fig. 3.15, structures of the MEMS devices, like backside enhancement and torsional spring and electrostatic comb-drive, are shown in details. The link arm is used for releasing individual MEMS chip safely with high yield during the post-process.

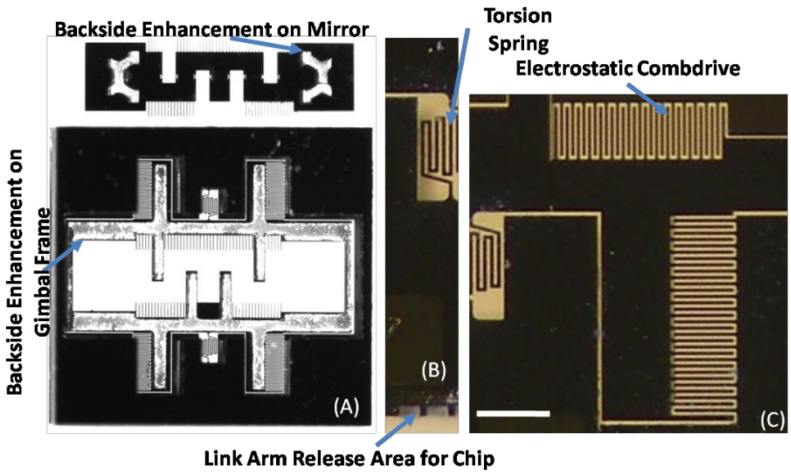

Figure 3.15 – 2D XY-plane MEMS resonant scanner details. (A) Stereomicroscope image of backside gimbal frame structure and inner scanning mirror (upper, clipped). (B) Stereomicroscope image of link arm for releasing and the torsion spring. (C) Stereomicroscope image of electrostatic comb-drive, scale bar: 200 μm.

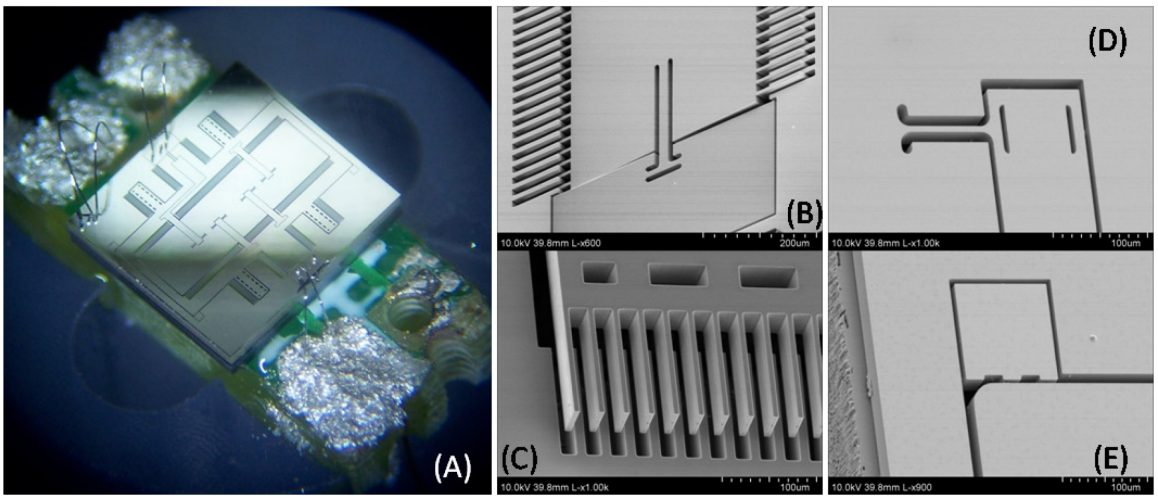

Figure 3.16 – 2D XY-plane MEMS resonant scanner for visible range imaging. (A) Stereomicroscope image of 2D XY-plane MEMS aluminum coated resonant scanner on a PCB inside OD10mm packaging; (B) SEM of comb-drive actuator next to the outer hinge; (C) SEM of tilted comb-drive actuator on the outer frame; (D) SEM of inner hinge; (E) SEM of electrical isolation bump on the gimbal frame.

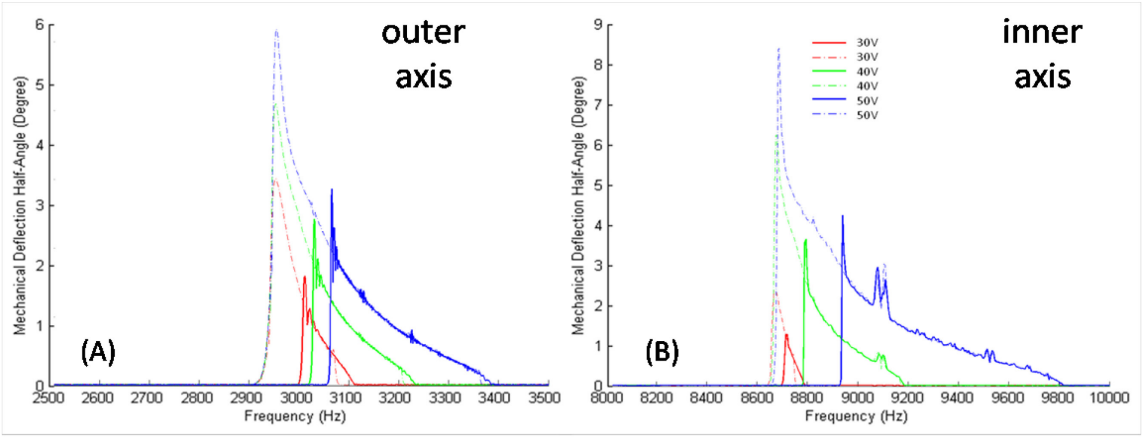

Figure 3.17 – 2D XY-plane MEMS resonant scanner characteristics. Mechanical scan angle versus driving frequency on (A) Outer axis; (B) Inner axis.

Performance test shows that the new 2D resonant microscanner can achieve large tilting angles (up to ± 6° mechanical scan angle for outer axis, up to ± 9° mechanical scan angle for inner axis) at low driving voltage (< 50 V) with a tunable driving frequency bandwidth close to resonance. Fig. 3.17 shows

dynamic response curves of the fabricated device with varied low driving voltages.

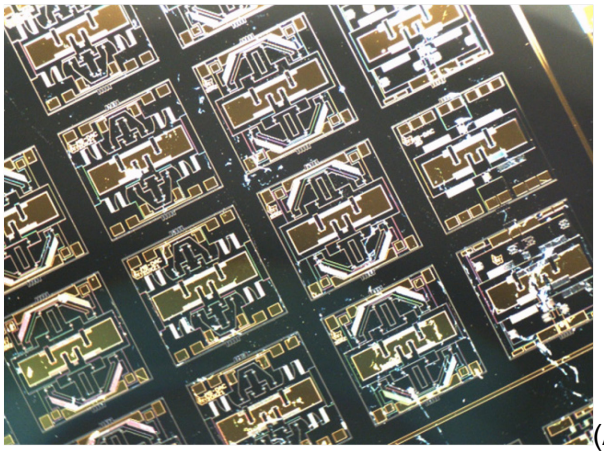 (A) 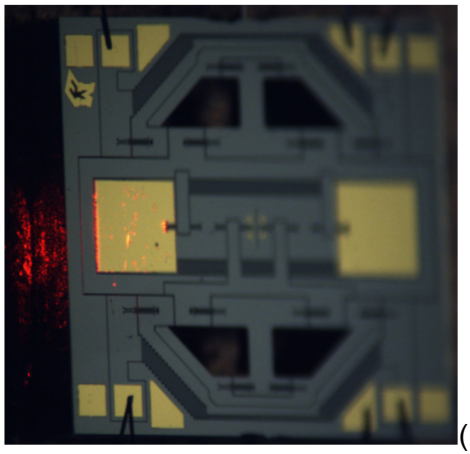 (B)

Figure 3.18 – 2D XZ-plane MEMS resonant scanner. (A) Stereomicroscope image of 2D XZ-plane MEMS resonant scanner module; (B) Wire bonded Au-coated 2D XZ-plane resonant scanner released from module, 3.2 × 3 mm^2.

2D MEMS XZ scanner is shown in Fig.3.18. Large Z-axis displacement performance of the XZ scanner is shown in Fig. 3.19. Up to 360 μm displacement can be found at peak under vaccum, while > 100 μm can be found at 1atm ambient air condition. The blurring under the stereomicroscope is used for characterizing the Z-axis displacement performance, in Fig. 3.20. The displacement versus driving frequency response curve at 1atm is shown in Fig.3.21.

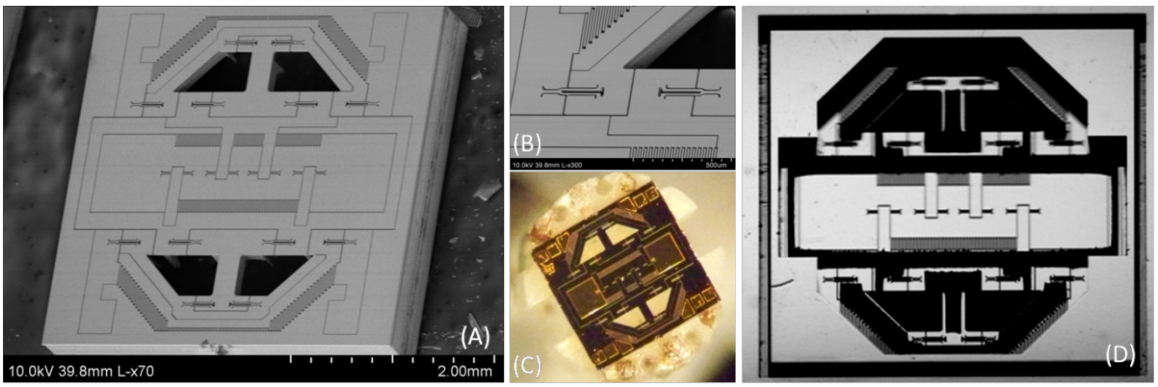

Figure 3.19 – 2D XZ-plane MEMS resonant scanner. (A) SEM of 2D XZ resonant scanner ; (B) SEM of hinges on outer frame for z-axis out-of-plane actuation; (C) Stereomicroscope image of 2D XZ-plane MEMS resonant scanner on a plastic stage in OD5mm packaging; (D) Stereomicroscope image of the backside of the scanner.

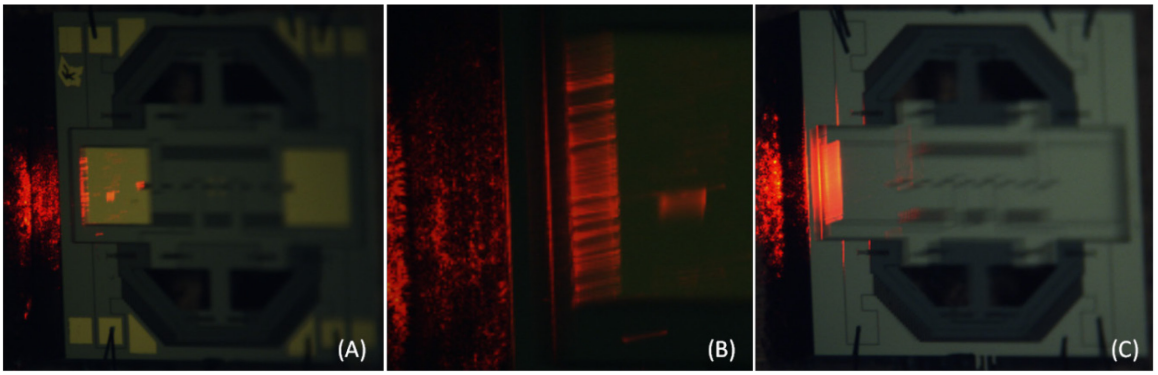

Figure 3.20 – 2D XZ-plane MEMS resonant scanner out-of-plane displacement on z-axis. (A) XZ Au/Ti coated scanner driven at 100 Vpp, 1atm, medium displacement ~ 100 um; (B) Zoom-in view of XZ Au/Ti coated scanner at 100 Vpp, 6 Torr, driving frequency 2950 Hz with maximum displacement at peak ~270 μm; (C) XZ aluminum coated scanner driven at 40 Vpp, 31 mTorr, driving frequency 2653 Hz with maximum displacement at peak ~ 360 μm.

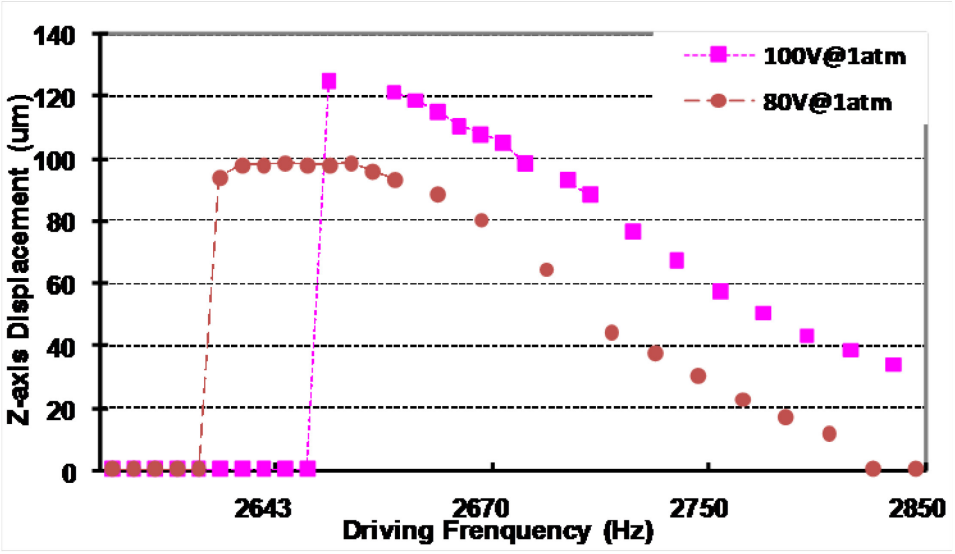

Figure 3.21 – 2D XZ-plane MEMS resonant scanner characteristics, out-of-plane z-axis displacement versus driving frequency under different driving voltage at 1 atm ambient environment.

3.3 Thin film PZT based MEMS Scanner

To perform real time vertical cross-sectional imaging in live animals, we have developed a miniature axial (Z-axis) scanner that can move the dual axes focal volume with sufficient speed and linearity to create high resolution images of the epithelium without distortion. High actuations speeds are needed for this application because small animal (e.g. mouse) models have much larger relative breathing displacements and faster heart rates than humans and these movements can introduce motion artifact into the images. Novel multi-axis differential scanner and monolithic XZ scanner will be introduced individually. The monolithic XZ scanner will be integrated into OD5mm package for vertical cross-sectional imaging with dual axes confocal endomicroscope.

3.3.1 Working Principle

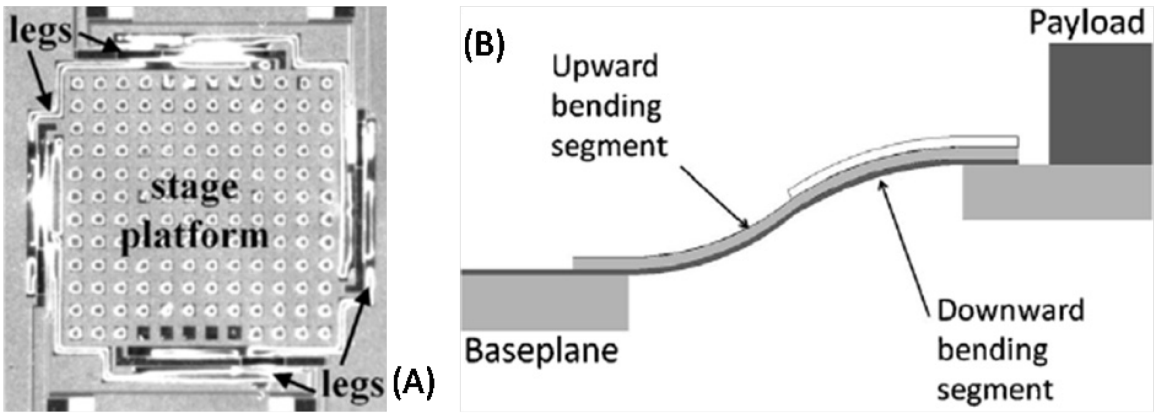

Figure 3.22 – Working principle of thin-film PZT based MEMS scanner. (A) Single beam based Z-axis scanner; (B) Cross-sectional view of the bending beam's schematic drawing.

Z-axis actuation will be developed using piezoelectric thin films, which can provide much larger displacement forces than most micro-actuation technologies. In unimorph piezoelectric beams, the contraction of the piezoelectric thin films within the beam causes either an upward or downward bending of the actuator, converting a large piezoelectric actuation force into significant displacements. In previous work [56], the upward and downward bending unimorphs were used to generate a net lateral displacement at the working tip of the actuator, as shown in Fig. 3.22 and Fig. 3.23. The operating principle uses two layers of platinum (Pt) to sandwich the piezoelectric element (PZT) deposited over a SiO_2 layer. A layer of gold (Au) is used to provide stiffness. The upward and downward bending unimorphs will be combined to achieve net vertical motion in the Z-axis, Fig. 3.22B. The forces generated are much higher than that of other micro-actuators, and the displacements are much larger than that of most piezoelectric materials [57, 58].

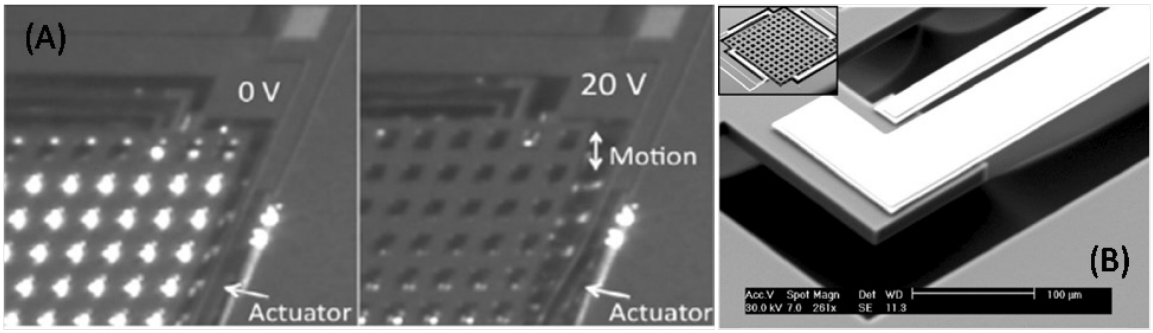

Figure 3.23 – Characterization of single beam based Z-axis scanner. (A) Single beam based Z-axis scanner driven at 20 V; (B) SEM of single unimorph beam based z-axis scanner [56].

3.3.2 Fabrication Process

The devices are fabricated using a new robust SiO_2 encapsulation trench fabrication process shown in Fig. 3.24. Trenches are etched by DRIE through the device layer of an SOI (30/2/500 μm) wafer, then filled with SiO_2 and planarized by chemical mechanical polishing (CMP) (Fig. 3.24a). The SiO_2 trenches define the gimbal frame and joint islands under the PZT folding beams with high accuracy and resistance to damage during later processing. A Pt/PZT/Pt/Ti stack and Au coating (for electrodes and dictating beam bending profiles) are then deposited and patterned (Fig. 3.24b). Structural features are roughly defined by front-side DRIE (Fig. 3.24c). Next, front-side features are protected by photoresist AZ9260 during backside DRIE that partially removes the silicon handle layer to provide space for scanning motion. XeF_2 etching is performed (Fig. 3.24d) to release the PZT beams, silicon islands between beams, and the gimbal frame, which are protected by the aforementioned SiO_2 trench barrier.

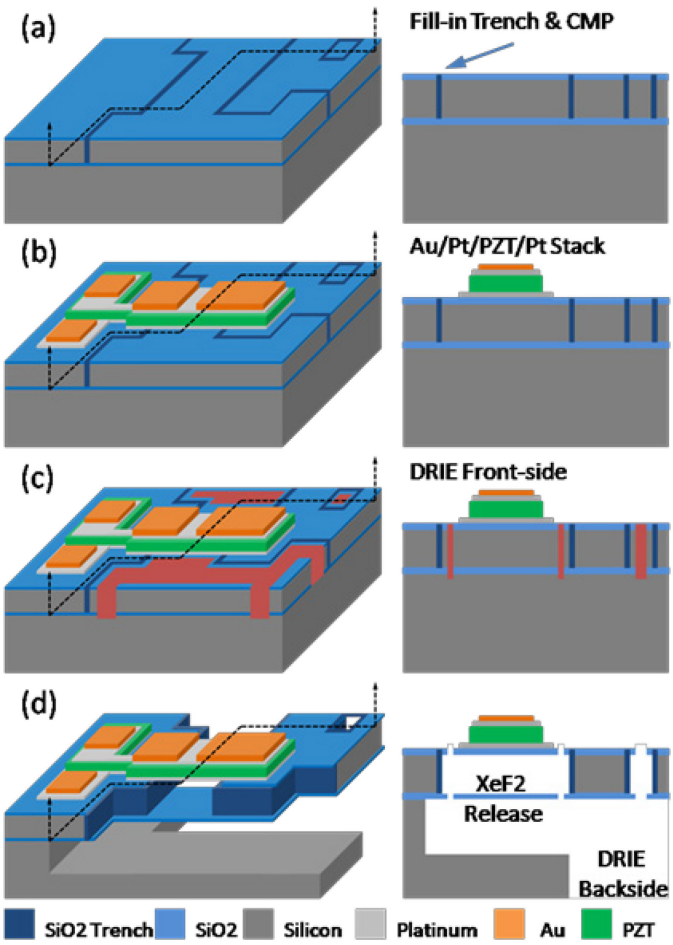

Figure 3.24 – SiO_2 trench encapsulation based fabrication process.

3.3.3 Multi-axis Differential Scanner

3.3.3.1 Scanner Design

An example of how upward and downward bending piezoelectric unimorphs may produce net translational motion by connecting bending unimorphs in series is shown in Fig. 3.25. The design of an multi-axis differential (Z-axis piston, tilt and tip motion) scanner will begin with a preferred actuator layout using the space constraints of the dual axes scan head in OD5mm package. A top view of the schematic layout of the proposed multi-axis

differential system is shown in Fig. 3.25A. An actuator leg is placed at each of the four corners of the mirror platform to drive vertical movement using an applied voltage to the bond pads. Adjacent actuators provide alternating upward and downward motion to provide the axial scanning movement. The side view in Fig. 3.25B shows the individual two fold Z-stage configuration and the downward and upward bending segments located below the mirror platform. The synchronized motion of these segments creates a net force that scans the mirror platform in the axial (Z-axis) direction. The photomask design of individual actuator is shown in Fig. 3.25C. There is a tradeoff between actuator length ($L_{seg,up}$+$L_{seg,down}$), vertical displacement, and natural frequency in Hertz. As expected, the Z-axis displacement increases with the length of the actuator. We can fabricate devices with a wide range of actuator lengths that will meet the performance specifications for the axial displacement needed to vertically scan the full thickness of the epithelium (> 500 μm).

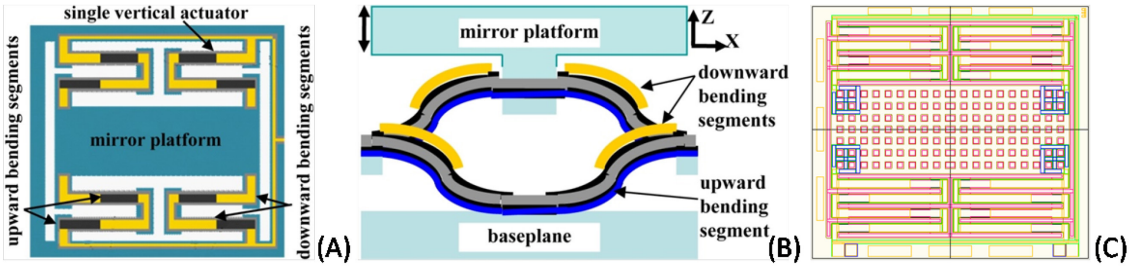

Figure 3.25 – Multi-axis differential actuator. (A) Top view of differential actuator layout shows one leg at each of the four corners of the mirror platform. Adjacent actuators provide alternating upward and downward motion to provide real time Z-axis displacement and tilt-tip motion. B) Side view shows individual two fold differential actuator configuration with downward and upward bending segments. C) Mask CAD design for the four-fold differential actuator which is in the middle of fabrication. (3.2 mm width × 2.9 mm height).

3.3.3.2 Characterization

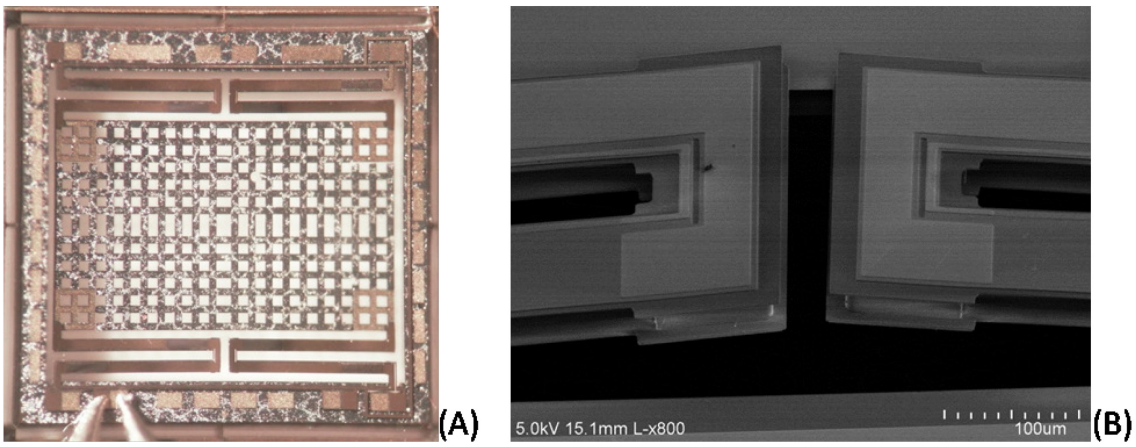

Figure 3.26 – Multi-axis two-fold thin-film PZT based device with capacitive sensor. (A) Stereomicroscope image of the device; (B) SEM of the two fold beams and SiO_2 encapsulation.

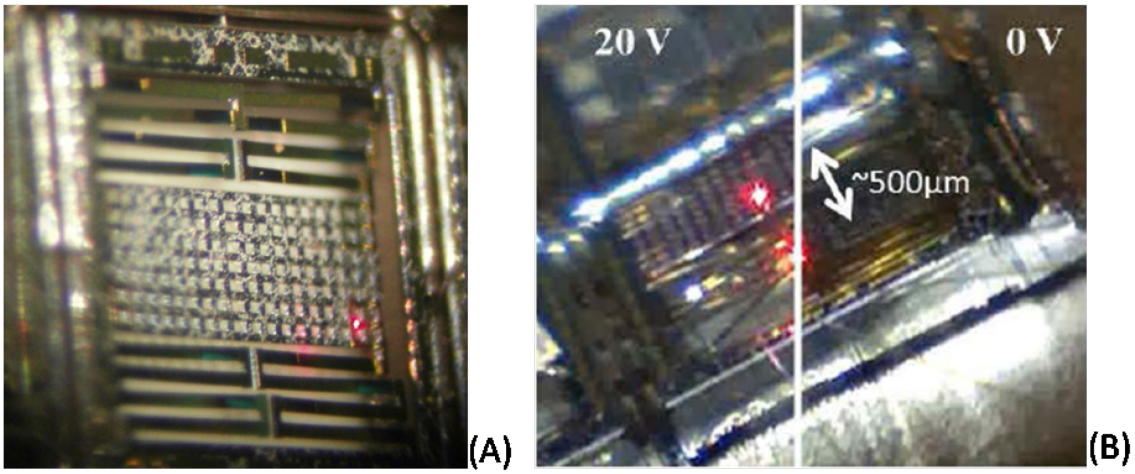

Figure 3.27 – Multi-axis four-fold thin-film PZT based device. (A) Stereomicroscope image of the device; (B) Large Z-axis displacement > 500 µm at 20 V driving voltage. Monolithic XZ (potential Y-axis scanning with differential driving) thin-film PZT based device.

Multi-axis differential device is shown in Fig. 3.26 and Fig. 3.27, with two folded and four folded unimorph thin-film PZT beams respectively. The large displacement > 500 µm under low driving voltage 20 V is performed with four folded beams, shown in Fig. 3.27B.

3.3.4 Monolithic XZ-plane Scanner

3.3.4.1 Scanner Design

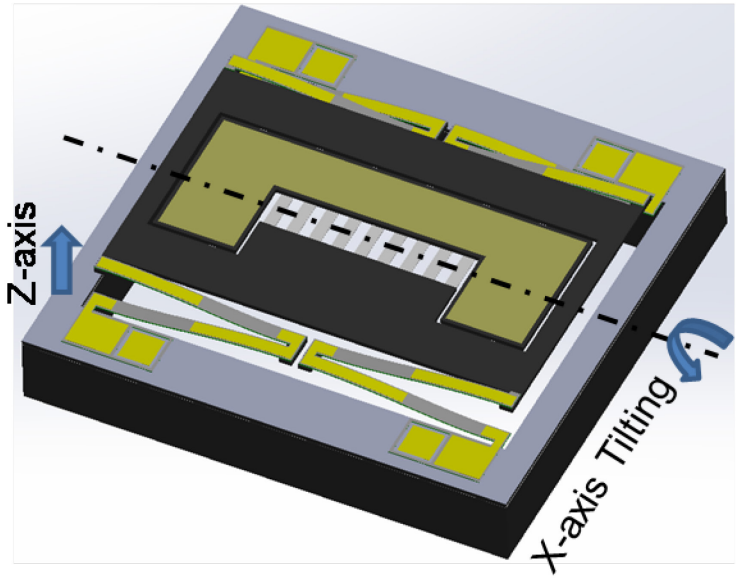

Figure 3.28 – Monolithic design for vertical cross-sectional imaging with dual axes confocal endomicroscope, footprint 3 × 3.2 mm^2.

We propose a novel thin-film PZT translational/tilt micro-scanner (footprint: 3 × 3.2 mm^2) for large FOV vertical cross-sectional (XZ-plane) imaging with a dual axes confocal fluorescence medical endomicroscope (outer diameter < 5 mm), shown in Fig.3.28. Vertical cross-sectional view has rarely been exploited by endomicroscopes while en-face (XY-plane) imaging with slow z-stacking must be resorted to, largely because fast axial scanning is challenging in limited space. Using folded PZT unimorphs with fast response and a passive inner silicon dioxide (SiO_2) spring array, this device performs both large vertical (Z-axis) displacement and high-speed, large-amplitude tilting (X-axis during imaging).

A single-beam unimorph thin-film PZT translational micro-scanner with up to 100 μm displacement was demonstrated [56]. Utilizing two or more folded

beams at the devices' four corners, the current monolithic micro-scanners perform more than double z-axis displacement and eliminate twisting about the z-axis. Meanwhile, inside a gimbal frame an inner scanning mirror supported by a passive SiO2 spring array can perform large tilting angle amplitude using low voltage, high frequency AC excitation (< 5 V_{pp}) delivered through the outer PZT beams. This allows the device to reach larger out-of-plane displacements and higher bandwidth than existing micro-scanners/actuators for out-of-plane displacement based on electrostatic or electrothermal transduction, while power requirements and volume are much lower than electro-magnetic devices. An alternate thin-film PZT based micro-scanner [59] demonstrated large tilting angle at high speed but much smaller displacement on the z-axis.

3.3.4.2 Characterization

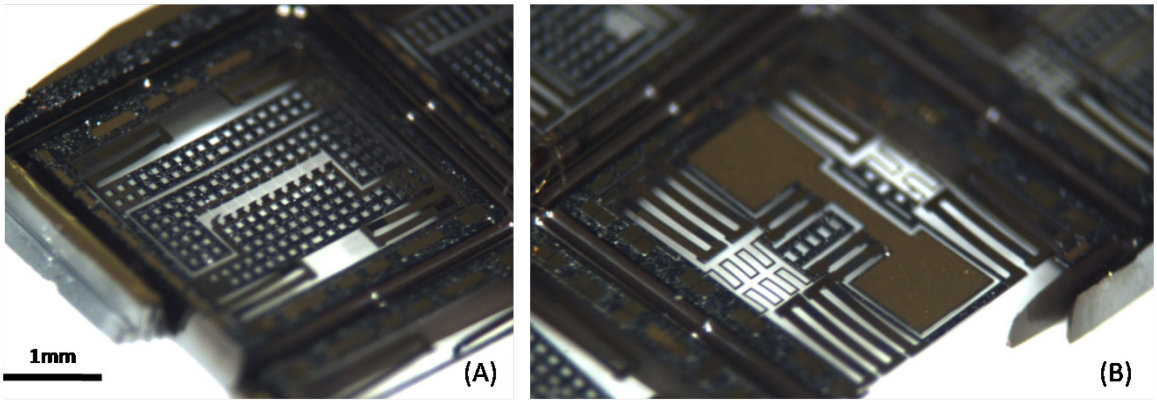

Figure 3.29 – Monolithic thin-film PZT based device. (A) Passive SiO_2 spring array based XZ device; (B) Next generation PZT active spring array based 3D scanning device (raster scan pattern on XZ or YZ-plane).

The monolithic translational/tilt micro-scanner stereomicroscope is shown in Fig. 3.29A, with a second generation design's image shown in Fig. 3.29B, in

which the inner dumbbell-shape scanning mirror is coated with patterned Au/Ti for near infra-red light beam reflection (> 90% efficiency).

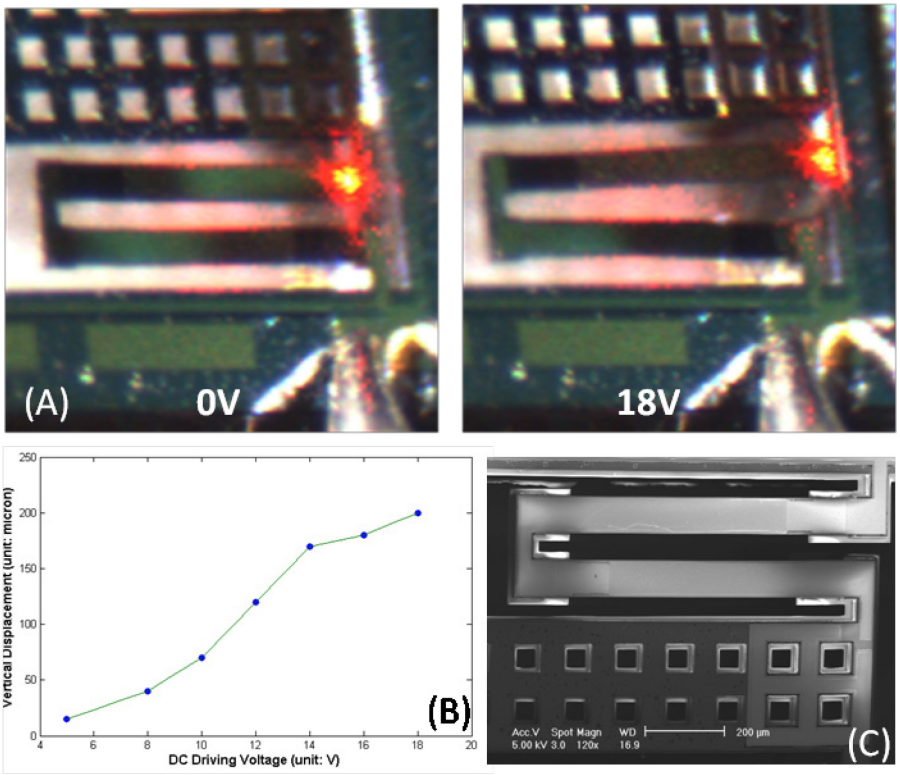

Figure 3.30 – Characterization of the translational out-of-plane displacement of the thin-film PZT two-fold unimorph beams driven monolithic device. (A) Large displacement > 200 μm performed by thin-film PZT based two-fold beams driven at DC 20V (B) Z-axis displacement of the outer gimbal frame of the monolithic XZ-plane scanning device; (C) SEM of thin-film PZT folded beams.

The static and dynamic performance of the monolithic micro-scanner has been characterized. Large vertical translation (> 200 μm) is achieved at 18 V (Fig. 3.30A), with measured bandwidth of Z-axis motion up to 200 Hz. SEM images of PZT two-fold beams is shown in Fig.3.30C. A passive SiO_2 spring array supporting the mirror is shown in Fig.3.31A. The inner mirror achieves mechanical scanning angles up to ±6º with resonant frequency 3.8 kHz

(Fig.3.31B). The translation/tilt range and bandwidths correspond to future endomicroscope imaging up to 30 frames per second with 800 × 200 μm^2 FOV in the XZ-plane.

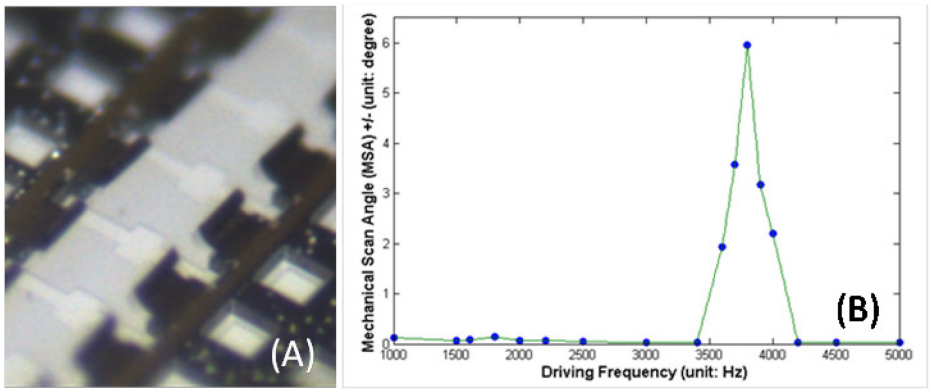

Figure 3.31 – Characterization of the inner tilting mirror of the thin-film PZT two-fold unimorph beams driven monolithic device. (A) Stereomicroscope image of 2 μm thick passive SiO2 spring array; (B) Mechanical scan angle (MSA) versus driving frequency, large tilting angle of the inner mirror with low driving voltage at extremely low current, MSA ±6º is realized @ 3.8 kHz 5 Vpp for 800 μm FOV on X-axis (for lateral scanning) with dual axes confocal endomicroscope.

Chapter 4

Imaging System Integration and Characterization

Based on the key components, including the MEMS scanner, actuator and micro-optics, we have performed system integration of the multi-spectral dual axes confocal endomicroscope prototypes, from OD10mm handheld to OD5mm miniature imaging system. For "proof-of-concept" study, we are mainly focused on targeted vertical cross-sectional imaging with multi-spectral OD10mm handheld dual axes confocal endomicroscope system. This system is characterized in the reflective mode first. Then, to test its vertical cross-sectional imaging performance in the fluorescent mode, we acquired images on a cubic scattering-free PDMS based phantom. In addition, NIR dye stained bulk tissue specimens have been *ex-vivo* imaged with the dual axes confocal endomicroscope to validate the vertical cross-sectional imaging under scattering conditions.

4.1 System Integration

Systems integration is a very challenging part of the development of the dual axes confocal endomicroscope because of the small size required to insert

the instrument into hollow organs and to perform accurate and stable placement on the epithelium of the hollow organ in live animals or human. This process requires a package design that allows for precise mounting of the following optical elements: two fiber-coupled collimator lenses, a 1D or 2D MEMS scanner for XY-plane scanning, Z-axis scanner for focusing, a parabolic focusing mirror, and a hemispherical index-matching solid immersion lens (SIL) element for index matching [22, 45]. Two collimated beams are focused at an inclination angle θ to the Z-axis by a parabolic mirror with a maximum cone half-angle α to a common point in the tissue after being deflected by a MEMS scanner. Wiring, packaging, and alignment for micro-optics will be described in details in section 4.1.

4.1.1 MEMS Device Wiring and Packaging

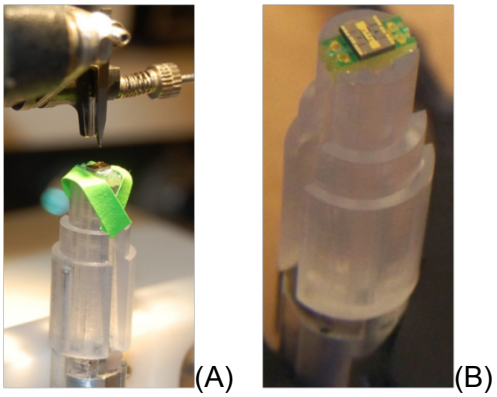
(A) (B)

Figure 4.1 – Wire bonding process for MEMS chip packaging inside the endomicroscope. (A) Photograph of wire bonding process for the 1D MEMS scanner glued in the OD10mm handheld system packaging; (B) Photograph of a 2D Au/Ti coated MEMS device on PCB in the OD10mm handheld system packaging.

For OD10mm handheld dual axes confocal endomicroscope system, MEMS scanner is glued by conductive silver epoxy (EG58, Thorlabs, USA) onto the custom-made printed circuit board (PCB). Then the Au wire (OD 0.015", West

Bond) is used for wiring bonding from the Au/Ti pad on the MEMS chip to the Au pad on the PCB, as shown in Fig. 4.1. Copper wires are soldered (or silver epoxy) onto the PCB and used for driving voltage electricity delivery from outside to the MEMS chips or sensing signal transmission, as shown in Fig. 4.1 and Fig. 4.2A. Similar approach has been used for packaging of MEMS devices (1D, 2D XY-plane or 2D XZ-plane, or monolithic thin film PZT actuator) in the OD5mm miniature endomicroscope, as shown in Fig. 4.2.

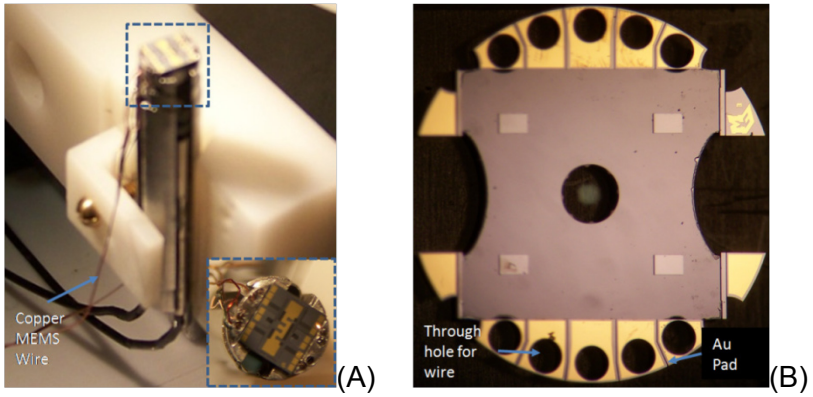

(A) (B)

Figure 4.2 – Wiring and packaging of MEMS chip inside OD5mm endomicroscope. (A) Photography of the Au/Ti coated 2D MEMS device in OD5mm packaging; (B) Miniature SOI based MEMS chip holder for advanced packaging in OD5mm or smaller instrument.

In the OD5mm instrument packaging, the MEMS chip holder is made out of stainless steel, which has better strength in miniature scale and can perform a similar function as a PCB holder. For advanced packaging, we will use silicon on insulator (SOI) based MEMS chip holder for OD5mm and smaller instrument in the future, in Fig. 4.2B.

4.1.2 Micro-Optical and Opto-mechanical Devices

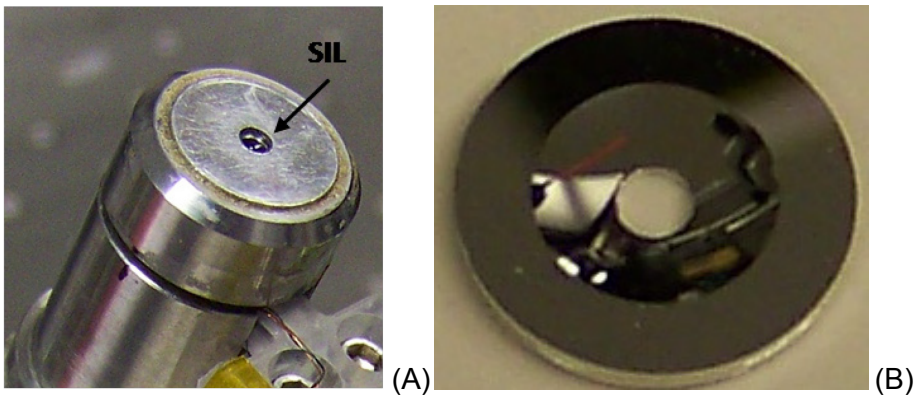

Figure 4.3 – OD10mm parabolic mirror packaging in the endomicroscope. (A) OD10mm parabolic mirror with SIL in the center packaged in the handheld system; (B) OD10mm parabolic mirror's reflective surface fabricated by single point diamond turning.

The flat side of the SIL, Fig.4.3A, is placed in the center of the parabolic mirror and used against the tissue surface to couple the incident beams with minimal aberrations. The parabolic mirror is fabricated with glass substrate using a molding process that provides a surface profile and smoothness needed for diffraction-limited focusing of the collimated beams (Anteryon, Netherland). In the optical path, once the collimated beams are aligned parallel to each other, the parabolic mirror then provides a “self-aligning” property for the optical imaging system, which forces the focused beams to intersect at a common focal point within the tissue. Focusing is performed primarily by the parabolic mirror which is a non-refractive optical element and produces beams with an NA of around 0.12. This feature allows for light over a broad spectral regime to become focused to the same point below the tissue surface simultaneously, allowing for multi-spectral confocal imaging to be performed. As shown in Fig.4.3, parabolic mirrors are glued and sealed inside stainless steel cap for good alignment and instrument waterproof protection. As an alternative approach, single point

diamond turning (SPDT) machining has also been performed successfully for fabricating both OD10mm parabolic mirror and OD5mm one using optics grade aluminum alloy material, shown in Fig. 4.3B. To realize the ultra-thin thickness without geometry deformation is the most challenging work. For example, the thickness of OD5mm parabolic mirror is only 0.5 mm on the edge, <0.2 on the inner diameter (ID) 2 mm central hole for SIL.

Fiber coupled collimators are used for those two collimated beams in the dual axes confocal imaging system, as shown in Fig. 4.4. The optical path of the dual axes endomicroscope consists of two parallel and collimated beams, each being used to provide an illumination and a collection optical path, respectively. In the OD10mm handheld system, we utilize a custom-made achromatic doublet lens NT65-568 (Edmund Optics, NJ, USA) based collimator (600 nm to 800 nm, 2.99 mm focal length, GRINTECH GmbH, Jena, Germany) with OD2.8mm, shown in Fig.4.4A. Single mode fiber (S630-HP, NA = 0.12, Nufern, East Granby, CT) is used in the fiber coupled achromatic collimator. The fiber and the lens are mounted by active alignment using optical grade UV-glue (direct gluing) with the goal to obtain an pointing accuracy of < 0.25º on best effort basis (approx. 0.1º). For the miniature OD5mm system, a gradient-index (GRIN) lens based collimator with OD1.2mm has been developed for NIR range, shown in Fig. 4.4C&D. Single mode fiber (780-HP, NA = 0.12, Nufern, East Granby, CT) is used in the GRIN lens based collimator.

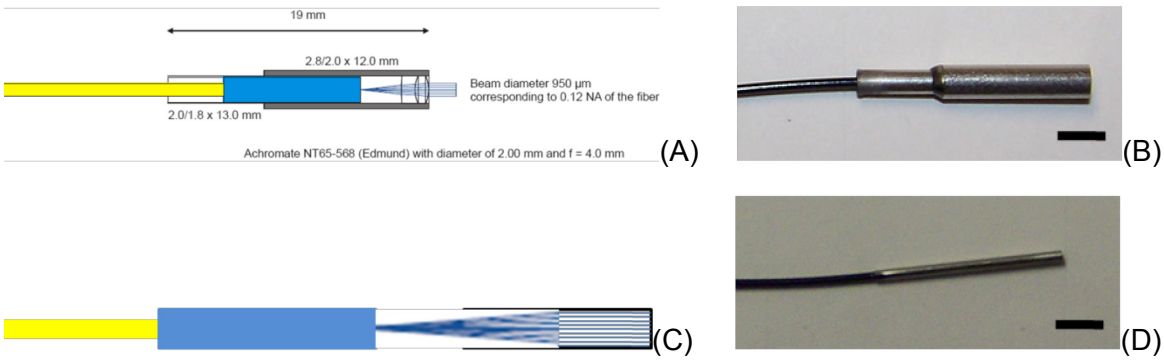

Figure 4.4 – Fiber coupled collimators. (A) Schematic of achromatic lens based collimator; (B) Photograph of Achromatic lens based collimator; (C) Schematic of GRIN lens based collimator; (D) Photograph of GRIN lens based collimator. Scale bar: 5mm.

4.1.3 Alignment and Integration

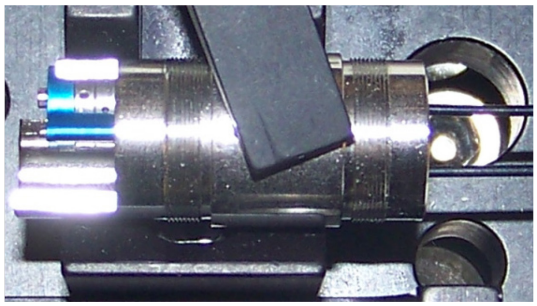

Figure 4.5 – Beam alignment setup. Achromatic collimators are packaged inside the collimator housing with two prisms on the excitation beam arm for fine adjustment.

Alignment of the two collimated beams in the dual axes configuration is a key procedure to maximize the imaging quality of this instrument. This can be accomplished by placing the two fiber-pigtailed collimators in a pair of precision machined sleeves in the housing, as shown in Fig. 4.5. The laser beam is coupled into the single mode fiber based achromatic collimator. The illumination beam (0.95 mm $1/e^2$ diameter) is delivered through the collimator. The collimators are fixed inside two parallel holes drilled using a computer numerical control (CNC) machine (Haas system). The illumination beam passes through

two custom-made 0.1 deg optical wedges (Risley prisms) that are 3.5 × 3.5 mm^2 in dimension, made of N-BK7 glass, and anti-reflection coated with reflectivity < 0.5% for 640-800 nm (Tower Optical, Boynton Beach, FL). Each Risley prism is held by a metal holder, shown in Fig. 4.5, which is located inside a sleeve through Class III medium fit. A miniature wrench is used to turn the processing holes. The Risley prisms provide fine adjustment to bring the illumination and collection beams into a parallel relationship within 0.05 degrees. The center-to-center distance between the collimated beams is 3.8 mm in the OD10mm handheld system. For OD5mm miniature system, the center-to-center distance is slightly adjusted to 3.7 mm. The same alignment procedure can be applied for both handheld and miniature system. Optimal alignment is then validated by measuring the lateral and axial resolution in reflective mode, which will be introduced in section 4.2.1.

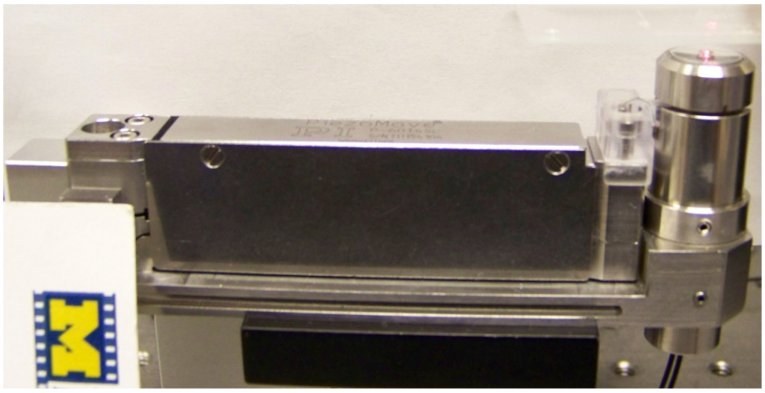

Figure 4.6 – OD10mm handheld multi-spectral dual axes confocal endomicroscope.

We have developed a OD10mm handheld “proof-of-concept” design that provides us an opportunity to study the vertical cross-sectional imaging in a dual axes endomicroscope. The instrument package, shown in Fig. 4.6, is realized

fully in stainless steel (Protomatic, Dexter, MI) and is sealed by epoxy glue. For vertical cross-sectional imaging with the OD10mm handheld system, we have developed a novel and compact opto-mechanical design for an axial scanning mechanism axial with a fast pure Z-axis fast motion. The axial scanning mechanism is based on the combination of MEMS 1D scanner with P601.4SL PZT actuator, which has been introduced briefly in Chapter 2. For our application, we need to realize a raster-scanning pattern with kHz tilting speeds at 2-10 Hz frame rates over a Z-axis range of 0 to 400 μm, Fig. 4.7A. An electro-static MEMS 1D X-axis resonant scanner is located in the post-objective position, and is directly integrated onto the Z-axis actuator through a PCB and cantilever (Fig. 4.7) that can be well aligned along the Z-axis and located closely to the parabolic mirror at the end. Using the “T-shape” mechanical cantilever linker (Fig. 4.7B, #2), the scanner and its PCB are all directly mounted onto the tip of the bulky PZT based Z-axis actuator with embedded strain gauge sensor (P601.4SL, Physik Instrumente, Auburn, MA) that translates the focal volume into the tissue over a range of 0 ~ 400 μm with 0 degree tilt angle (Fig. 4.7B). While scanning in resonant mode (> 3 kHz), the MEMS device is not affected by low frequency vibrations (< 100 Hz) produced by the Z-axis actuator.

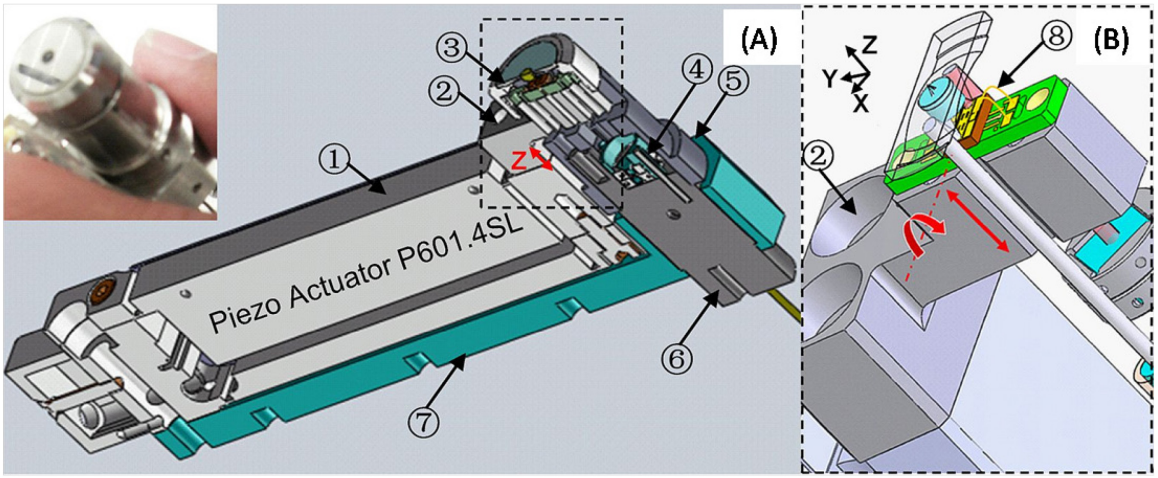

Figure 4.7 – Schematic of the OD10mm handheld dual axes endomicroscope packaging. (A) Cross-sectional view of system packaging without protection shell shows inner integrated XZ-plane 2D scan engine for vertical cross-sectional imaging (inset: handheld prototype); (B) Magnified view of XZ-plane 2D scan engine design. Components: (1) Z-axis piezo actuator; (2) “T-shape” cantilever on the tip of PZT actuator; (3) parabolic mirror and its holder; (4) prism holder clamp; (5) tube jacket; (6) collimator housing tube; (7) PZT actuator holder; (8) Au bonding wire for electricity connection.

OD5mm miniature dual axes confocal endomicroscope system has also been developed for small animal imaging, shown in Fig. 4.8. The fast Z-axis is realized by bulky PZT driver P601.4SL actuator on the backside through sliding mechanism, in Fig. 4.8A. 2D XY-plane MEMS scanner is used inside for *en-face* imaging, in Fig. 4.8B. Fig. 4.8C shows the OD5mm parabolic mirror with SIL glued in the central position. In the future, the XZ or monolithic thin-film PZT XZ scanner will be integrated into the OD5mm miniature system. The P601.4SL based Z-axis actuation will be eliminated so that the imaging system's rigid end length will be short (< 25 mm).

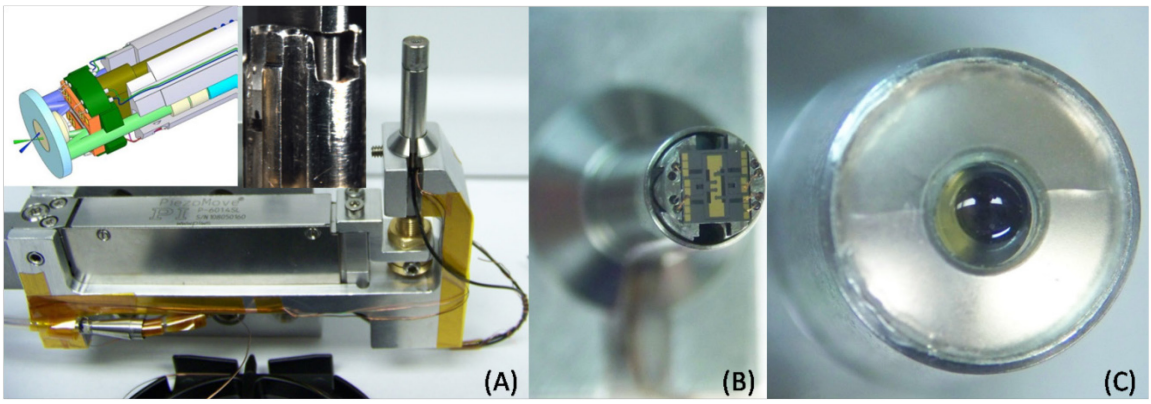

Figure 4.8 – OD5mm miniature dual axes confocal endomicroscope system with P601.4SL driver for small animal imaging, (A) System integration and packaging; (B) OD5mm tip without parabolic mirror cap; (C) Parabolic mirror on the cap.

4.1.4 Control and Image Acquisition

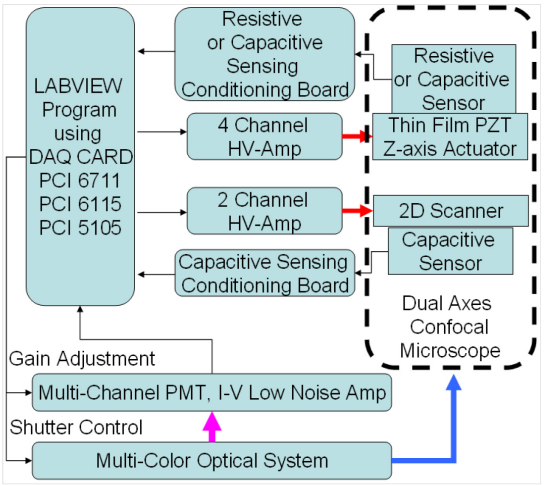

Figure 4.9 – Schematic of instrument control and data acquisition for multi-spectral dual axes confocal endomicroscope imaging system.

We used a multifunction data acquisition board (PCI-6115, National Instruments, Austin, TX) and 2-channel function generator (33522A, Agilent, Santa Clara, CA) to operate the instrument. A high speed analog output board (National Instruments, PCI-6711) will generate the waveforms needed to drive the scanning mirror, and will provide the triggers for the data acquisition board,

shown in Fig. 4.9. The MEMS scanner and Z-axis actuator are driven with a square and an edge-smoothed triangle waveform, respectively, using a 2-channel high voltage amplifier (TEGAM 2350, Geneva, Ohio). The mirror is excited to start tilting and reaches the peak amplitude by sweeping the pulse width modulation (PWM, 0 to 50%, with 10% step size) of a square waveform in 1.0 sec initiation time by fixing the drive frequency at a desired value for imaging. For example, the resonant frequency of the tilting mirror is 3010 Hz at a drive frequency of 6020 Hz, $f_{res}=f_{driving}\times N/2$, N=1). Meanwhile, synchronization of the phase between the driving waveform on X-axis and Z-axis, which is the key for vertical cross-sectional imaging at fast frame rates, is achieved using custom LabVIEW (National Instruments, Austin, TX) program.

We acquire and reconstruct vertical cross-sectional images with lateral field-of-view > 800 μm with a tissue penetration depth around 400 μm, as shown in Fig.4.10. Because we expect a transverse resolution of ~ 5 μm, the fluorescence image will be digitized to 480 × 240 pixels, which is oversampled by a factor of 2 to meet the Nyquist criteria. A high speed, 2 channels, 12 bit data acquisition board (National Instruments, PCI-6115) that can digitize 10×10^6 pixels/sec per channel is used. At this rate, two fluorescence images (671nm and 785nm wavelength) can be acquired at speeds up to 30 Hz, which easily exceeds our goal of 10 Hz. The vertical cross-sectional images have a high dynamic range (> 40 dB), and will be digitized to 12 bits at 10 frames per sec, limited by the gain-settling time of the PMT (> 2 ms). The field of view and frame rate for the images collected are determined by the amplitude and frequency of

these control signals. 2D vertical cross-sectional fluorescence images are acquired and displayed in real time to enable continuous visualization. All data are saved in 8-bit format video sequence and 12-bit format image, which can be viewed using NIH ImageJ® software.

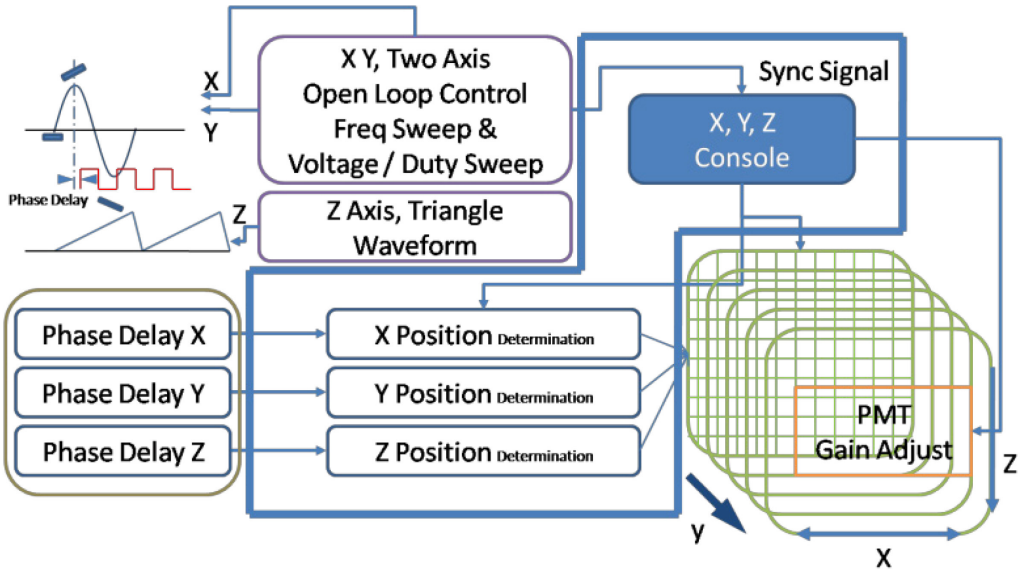

Figure 4.10 – Schematic of image reconstruction. Each XZ-plane image is acquired by scanning X-axis tilting mirror in ~ 3 kHz with 5 Hz on Z-axis. Phase is synchronized by Labview program.

4.2 System Characterization

4.2.1 Lateral and Axial Resolution

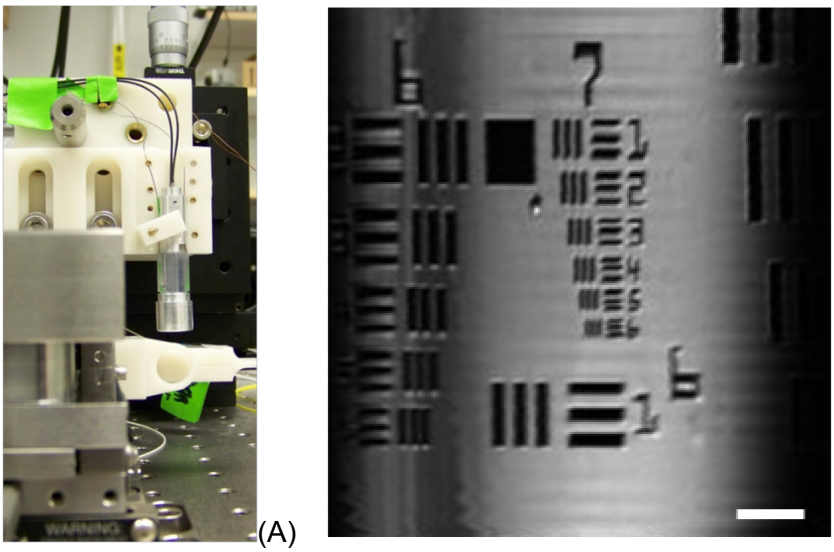

(A) (B)

Figure 4.11 – Lateral resolution testing. (A) Photograph of the test setup in reflective mode; (B) En-face (XY-plane) reflectance image of a standard USAF 1951 target shows lateral resolution of around 4 μm, FOV 400 × 400 μm^2, scale bar 50 μm.

For system characterization, we measured the lateral resolution of the handheld instrument by performing en-face (XY-plane) imaging of a standard (USAF 1951) resolution target mounted on an additional Y-axis scanner (P601.4SL, 0 to 400 μm, Physik Instrumente, Auburn, MA) that is placed outside of the instrument, shown in Fig.4.11A.

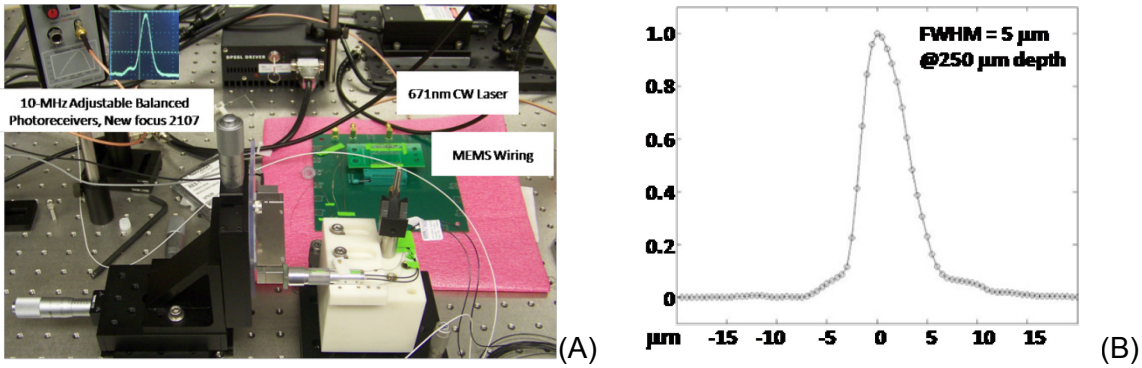

(A) (B)

Figure 4.12 – Axial resolution test, (A) Test setup; (B) Axial scan from a reflective target shows FWHM of 5 μm at depth of 250 μm in a scattering-free deionized-water film.

The 1-D MEMS scanner inside the instrument performed X-axis scanning. The lateral resolution from the en-face reflectance image is around 4 μm (group 7, element 5), shown in Fig. 4.11B.

For axial resolution measurement, we used the setup shown in Fig.4.12A. A reflective aluminum coated mirror is placed on the P601.4SL actuator for Z-axis scanning. The axial resolution was determined by measuring the full width at half-maximum (FWHM) of the signal reflected from the surface of a chrome coated mirror through a scattering-free deionized-water film between the mirror and the SIL to simulate the optical thickness of the tissue. The measured axial resolution was around 5 μm with 671 nm illumination, Fig. 4.12B.

To characterize the imaging performance and field of view in the fluorescent mode, we first image the fluorescent beads (excitation 671 nm) on the glass slides. X-axis lateral scanning is realized by 1-D MEMS scanner while the Y-axis scanning is done by outside P601.4SL actuator. Because of the post-objective scanning, the scan patter is an arc trajectory during the lateral scanning. From the *en-face* imaging in Fig.4.13, we can tell that beads' image on the left and right side is only the tip of the sphere beads due the arc scan pattern. From the center to the edge of the image, the distance difference is around 20 μm on the Z-axis.

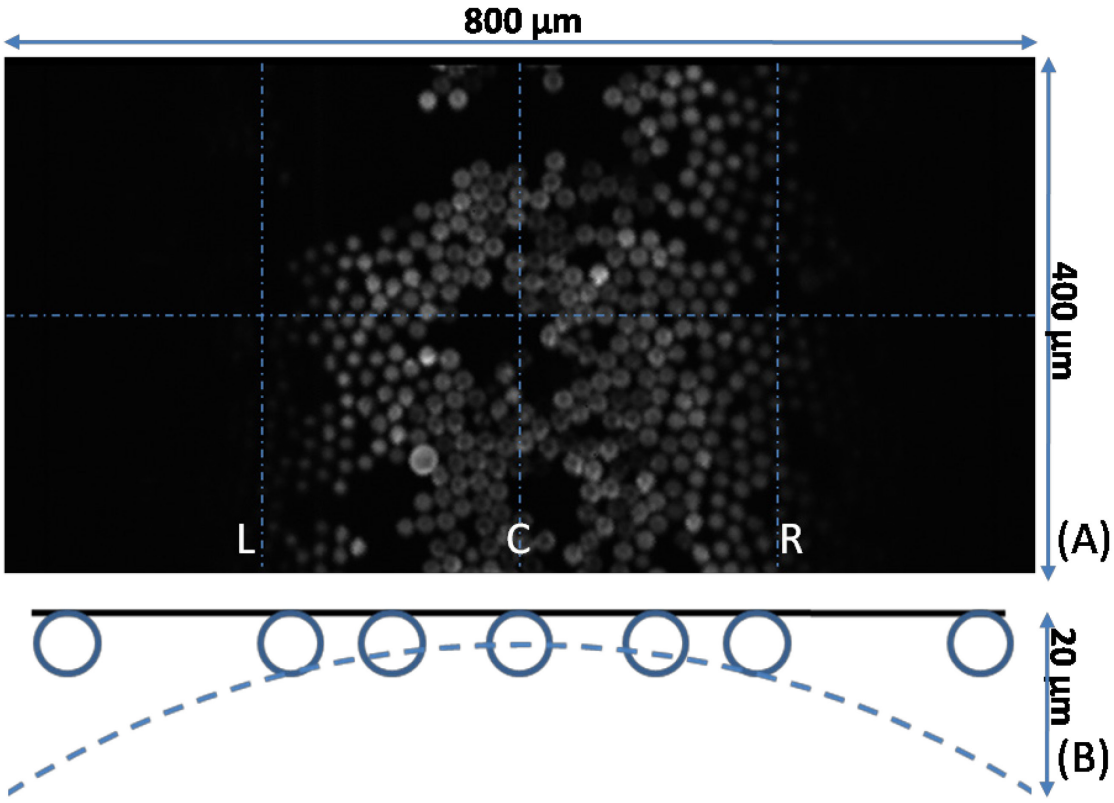

Figure 4.13 – *En-face* imaging on 15 µm fluorescent beads on glass slide. (A) 800 µm x 400 µm FOV, L: left, C: center, R: right; (B) Schematic of the post-objective scanning arc trajectory, showing 20 µm gap on the Z-axis.

To demonstrate the full field of view, we imaged the Cy5.5 dye diluted solution with low concentration of 10 µM, shown in Fig.4.14. The arc is shown at the border of dye solution and air gap. Some small particles are also visualized deeply in the fluorescent vertical cross-sectional image because of good axial resolution.

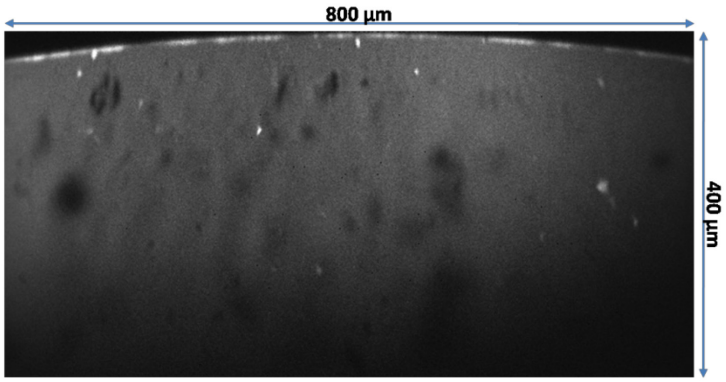

Figure 4.14 – Fluorescent vertical cross-sectional imaging with FOV 800 µm x 400 µm on Cy5.5 dye diluted solution with low concentration of 10µM.

4.2.2 Characterization of Vertical Cross-sectional Imaging

4.2.2.1 Vertical Cross-sectional Imaging on Phantom

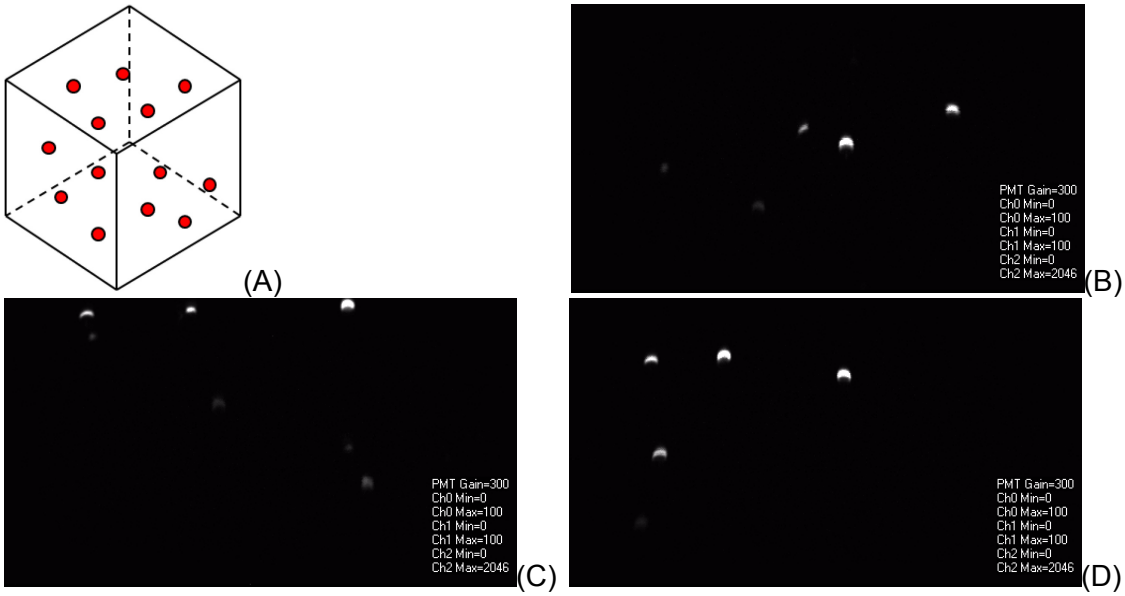

Figure 4.15 – Vertical cross-sectional imaging on fluorescent beads based 3D cubic phantom. (A) Schematic of 3D cubic PDMS phantom with mixed beads inside; (B) to (D) show Fluorescent vertical cross-sectional images of beads phantom with field of view 800 µm x 400 µm.

To the best of our knowledge, there is no commercial phantom developed for fluorescent vertical cross-sectional imaging characterization. To characterize

the vertical cross-sectional imaging performance, we developed a 3D cubic PDMS phantom with mixed fluorescent polyester beads (OD ~ 15 μm, excitation wavelength: 671nm) inside, Fig. 4.15A. In the test setup, we only use 2mW power intensity out of SIL for illumination. The gain of the PMT is set to 300 mV since the signal from fluorescent beads is very strong. As shown in Fig. 4.15B-D, vertical cross-sectional imaging of the polyester beads only show the upper side of the sphere while bottom signal is blocked. This is a unique performance of the vertical cross-sectional imaging on fluorescent beads. The MEMS scanner's mechanical tilting angle is fixed at ± 6º for 800 μm lateral scanning on X-axis. With good lateral and axial resolution (< 5 μm), OD15 μm beads can be shown in the vertical cross-sectional view with large field of view 800 × 400 μm^2.

4.2.2.2 *Ex-vivo* Vertical Cross-sectional Imaging on human colon tissue

To demonstrate the vertical cross-sectional imaging performance biological specimen with scattering, we imaged human colon tissue specimens. The fresh bulk tissues were collected via pinch biopsy during standard endoscopy at University of Michigan Hospital. Patient informed consent was obtained and approved by the Institutional Review Board of the University of Michigan School of Medicine. Fresh biopsy specimens were soaked for 1 to 5min in a near infra-red non-specific staining dye Cy5.5. The dye was dissolved, at a concentration of 100 μM in water that contained 10% DMSO solution to facilitate tissue penetration. Prior to vertical cross-sectional imaging, excess dye was removed by soaking and irrigating the tissues with water. In the tumor tissue, the epithelial layer is thicker than the one of normal tissue. As shown in Fig. 4.16, the

vertical cross-sectional images of tumor tissue and normal tissue visualize the differentiation of the crypts in the epithelial layer.

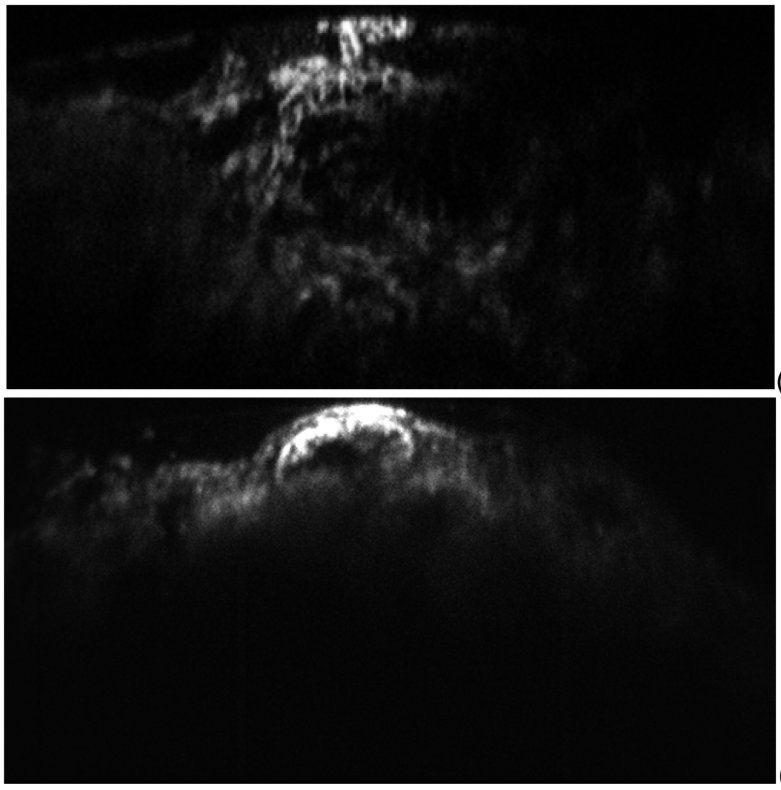

Figure 4.16 – Vertical cross-sectional imaging on human colon tissue. (A) Tumor tissue; (B) Normal tissue, crypts can be found in the morphology.

Chapter 5

Targeted Vertical Cross-sectional Imaging

In Chapter 5, the genetically engineered mouse model will be introduced first in section 5.1. Next, we will present the single-color NIR (λ_{ex} = 671 nm) ex-vivo targeted vertical cross-sectional imaging on the colon tissue (both distal and proximal ends) of the mouse model in section 5.2. Then, in section 5.3, we will describe the multi-spectral targeted ex-vivo and in-vivo vertical cross-sectional imaging on the mouse prolapsed area. Finally, fluorescence contrast ratio measurement will be discussed in section 5.4, based on the *in-vivo* targeted vertical cross-sectional images.

5.1 Genetically Engineered Mouse Model of Spontaneous Colorectal Cancer

Small animal models play an important role in the study of colon cancer biology because the natural history of these tumors develop over an abbreviated time course (between 6 to 12 months) compared to that of humans. A number of spontaneous tumor models have been genetically engineered to model colon cancer syndromes in humans, such as hereditary nonpolyposis colon cancer

(HNPCC) and adenomatous polyposis coli (APC) [60-62]. Our collaborators from Dr. Fearon's Laboratory at the University of Michigan have developed a genetically engineered mouse model of colon cancer (Fig.5.1 and Fig.5.2) that spontaneously expresses polyps in the distal colon and rectum [63, 64]. This small animal model can be used to demonstrate the imaging performance of the novel dual axes confocal fluorescent microscope and to evaluate specific binding of the fluorescence-labeled peptides. The model is based on mutations in the adenomatous polyposis coli (APC) gene to initiate cancer development in the distal colon. Previous mouse models based on the APC gene expressed tumor mainly in the small intestine where it would be extremely difficult to access using techniques of intra-vital microscopy in a non-terminal experiment. This new mouse model of colon cancer can express dypslastic lesions in the distal colon and forms invasive cancer for use to validate our miniature microscope and peptide probes. The human CDX2 sequences confer preferential transgene expression in colonic epithelium in the adult mouse, and mice carrying a CDX2P-NLS-Cre recombinase transgene and a loxP-targeted Apc allele developed mainly distal colon tumors (in Fig. 5.1), with carcinomas seen in 6 of 36 (17%) of mice after 300 days. Like human colorectal lesions, the mouse tumors also show bi-allelic APC inactivation, β-catenin dysregulation, global DNA hypomethylation, and chromosomal instability.

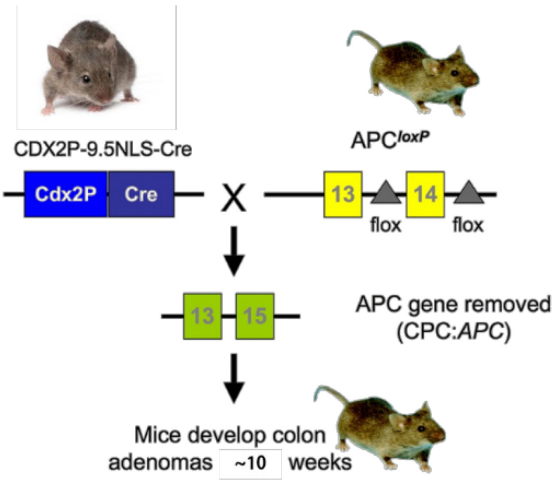

Figure 5.1 – The CPC;Apc mouse model of colon cancer. This genetically engineered mouse develops mutations in one allele of the Apc gene under regulation by Cre recombinase resultin in spontaneous adenomas in the distal colon.

The distal expression of colonic neoplasia in this genetically engineered mouse model allows for us to validate specific peptide binding to colonic adenomas in vivo. In Fig. 5.2, numerous dysplastic lesions that range in size from 2 to 5 mm can be seen in the distal colon (white box). In addition, 5 lesions can be seen in the small bowel (arrows), scale bar 10 mm.

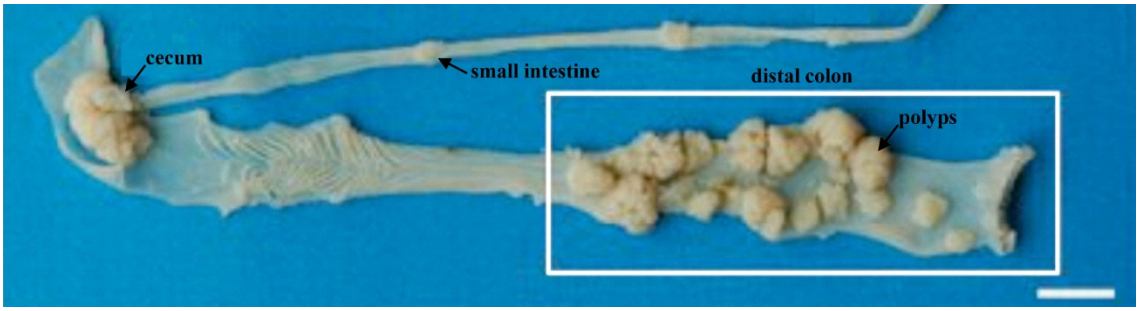

Figure 5.2 – The CPC;Apc mouse model of colorectal adenomas. This mouse is genetically engineered to spontaneously delete on Apc allele to develop polyps in the distal colon and rectum (box), scale bar 10 mm.

5.2 Single Color Targeted Vertical Cross-sectional Imaging

5.2.1 Administration and Methods

We demonstrated single color NIR targeted vertical cross-sectional fluorescence images in a mouse model of colonic dysplasia ex-vivo. The chemical structure of the Cy5.5-labeled peptide specific for colonic dysplasia is shown in Fig. 5.3. The amino acid sequence LTTHYKL is connected by a GGGSK linker on the C-terminus to the Cy5.5 fluorophore to prevent steric hindrance. This targeting peptide was selected using in vivo phage display technology [36]. We use CPC;Apc mice that are genetically engineered to spontaneously develop pre-malignant colonic lesions similar to that seen in human disease. Mice were cared for with approval of the University Committee on the Use and Care of Animals (UCUCA) at the University of Michigan and housed in specific pathogen-free conditions and supplied water *ad libitum*. As shown in Fig. 5.4A, CPC;Apc mice of age 6-7 months were injected with the Cy5.5-labeled peptide, LTTHYKL-GGGSK-Cy5.5, hereafter LTT*-Cy5.5, at a concentration of 400 μM via tail vein. LTT*-Cy5.5 was allowed to circulate for 15 minutes. The mice were then euthanized, and the colon was excised, washed, blotted dry, and mounted on glass slides using 3M Vetbond tissue adhesive. Distal and proximal ends of the colon tissue are shown in Fig. 5.4B. The fresh colonic mucosa were imaged immediately with 2 mW of excitation at λ_{ex} = 671 nm. Dysplasia is mainly located at the distal end while the proximal end is basically normal tissue area. The tissues were then fixed with 10% buffered formalin for 24 hours, paraffin-embedded and sectioned into 10 μm thin slices

and stained with hematoxylin and eosin (H&E). Histology was captured on an Axioskop2 upright microscope (Carl Zeiss Microimaging, Inc. Thornwood, NY).

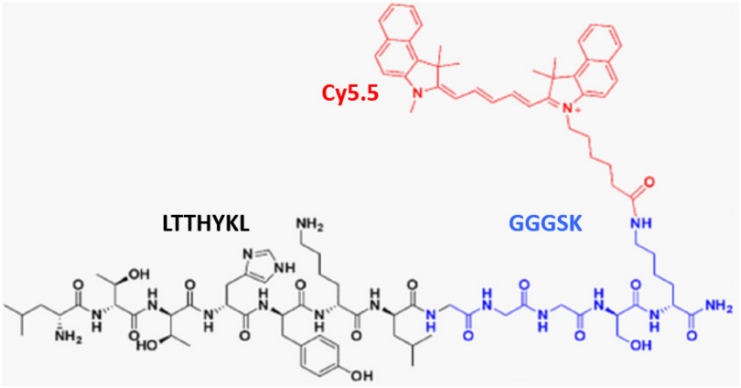

Figure 5.3 – Chemical structure of NIR dye Cy5.5 labeled peptide LTT*-Cy5.5. LTTHYKL peptide (black) with GGGSK linker (blue) and Cy5.5 fluorophore (red).

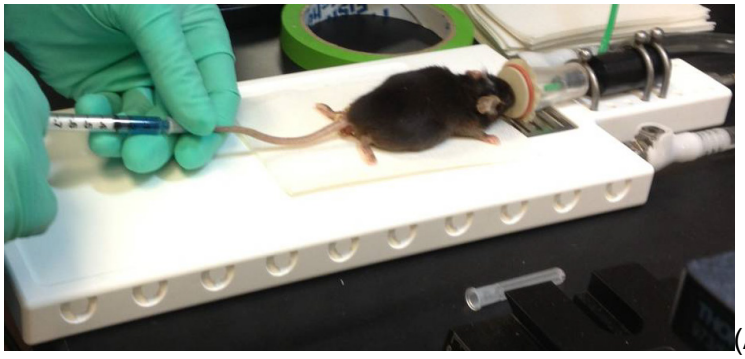
(A)

(B)

Figure 5.4 – Administration and method for targeted ex-vivo vertical cross-sectional imaging on distal and proximal colon tissue of CPC;Apc mouse model. (A) Tail-vein injection of peptide solution; (B) Photograph of proximal (left) and distal (right) ends of mouse colon tissue glued on glass slides.

5.2.2 *Ex-vivo* Imaging Results

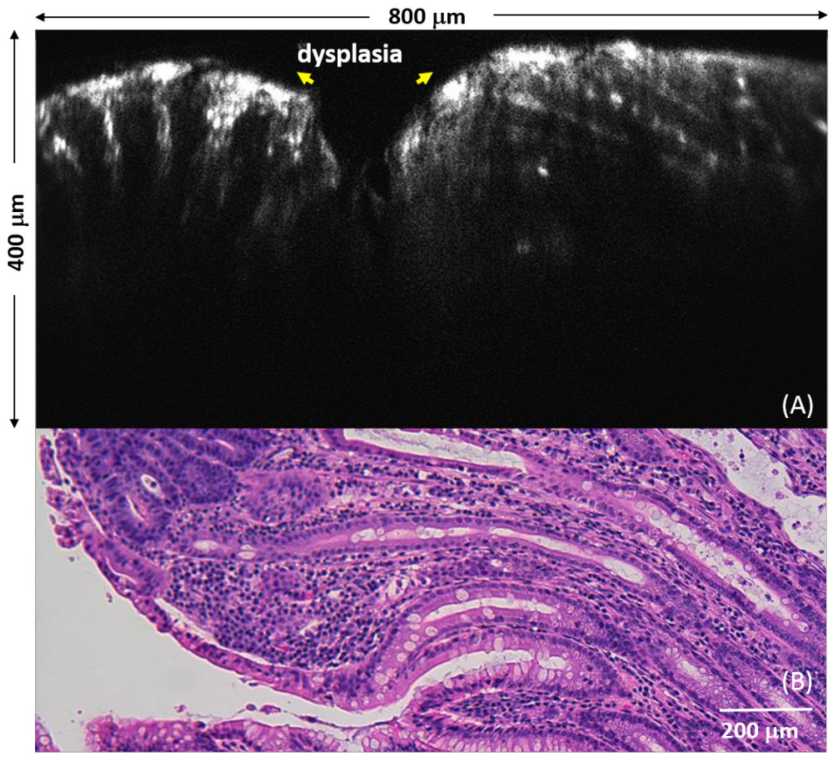

Figure 5.5 – Vertical cross-sectional image of colonic dysplasia. (A) NIR fluorescence image from CPC;Apc mouse colon ex-vivo shows vertical oriented dysplastic crypts. (800 µm x 400 µm FOV) (B) Corresponding histology (H&E), scale bar 200 µm.

Single color NIR (λ_{ex} = 671 nm) targeted fluorescence images of colon show dysplastic crypts in the vertical orientation, Fig. 5.5A, demonstrating the histology-like performance over a FOV of 800 µm (width) × 400 µm (depth). The corresponding histology (H&E) of dysplastic crypts are shown in Fig. 5.5B. The arc seen at the top of this image is likely produced by the interface between the SIL and tissue that results from post-objective scanning. The contrast from specific binding of the LTT-Cy5.5 peptide can be appreciated by the image of the border between normal colonic mucosa and dysplasia, as shown in Fig. 5.6A. Vertically oriented crypts can be appreciated in the corresponding histology (H&E), scale bar 200 µm, Fig. 5.6B. Use of a specific binding peptide allows for

the transition from normal to pre-malignant mucosa to be visualized with high contrast using the same gain on the PMT. Compared to normal colonic mucosa, the NIR fluorescence (excitation λ_{ex}=671 nm) intensity of dysplasia is >3. The peptide binds to cells in the epithelium (~ 150 to 200 µm), and tissue below is not expected to produce signal. A control for this peptide has been demonstrated previously [36].

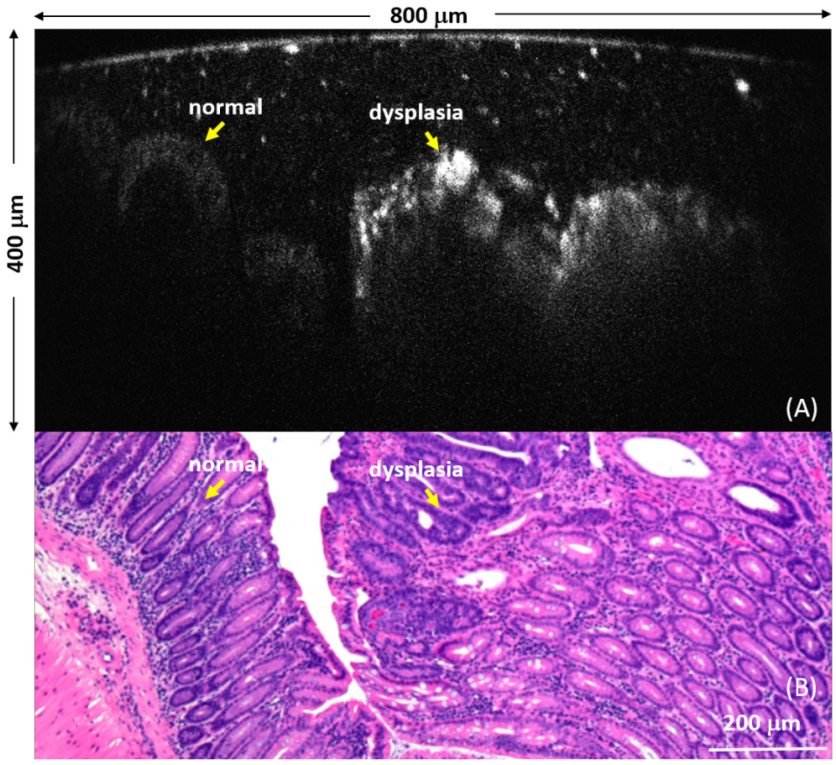

Figure 5.6 – Vertical cross-sectional image of the border between normal colonic mucosa and dysplasia. (A) NIR fluorescence image from CPC;Apc mouse colon *ex-vivo* shows the border between normal colonic mucosa and dysplasia shows increased contrast from specific binding of the LTT*-Cy5.5 peptide (800 µm x 400 µm FOV) (B) Corresponding histology (H&E), scale bar 200 µm.

5.3 Multi-spectral Targeted Vertical Cross-sectional Imaging

5.3.1 Administration and Methods

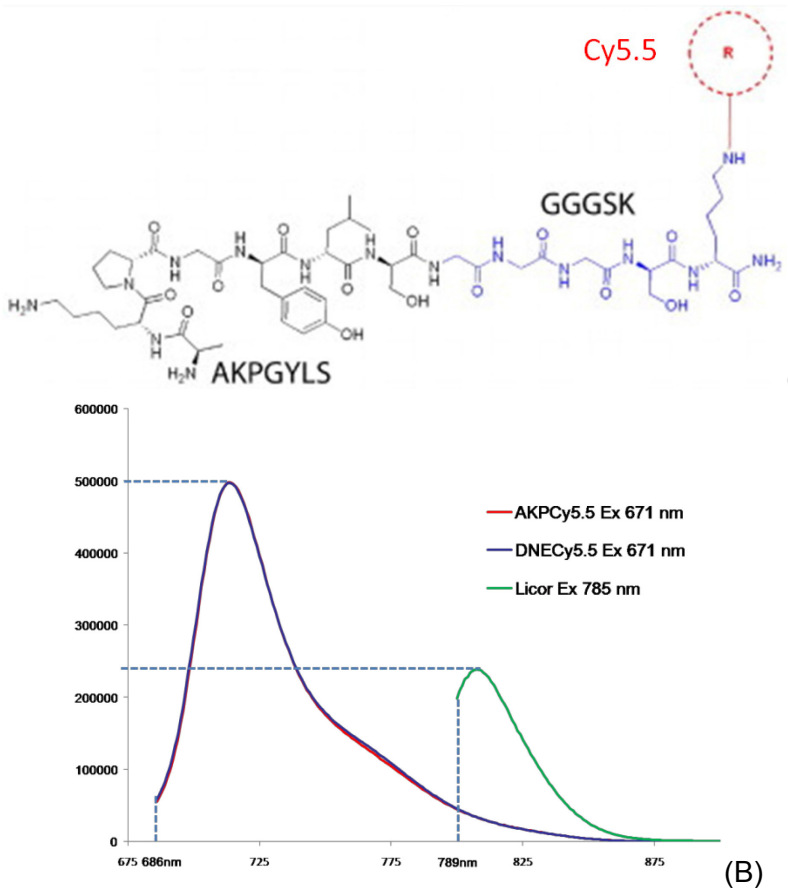

Figure 5.7 – NIR dye labeled peptide AKP*-Cy5.5. (A) Chemical structure of AKPGYLS peptide (Black) with GGGSK linker (blue) and Cy5.5 fluorophore (red); (B) Fluorescence spectrometry result of AKP*-Cy5.5 and DNE*-Cy5.5 and IRDye 800CW.

Single color NIR targeted *ex-vivo* vertical cross-sectional imaging demonstrates fluorescence contrast with the specific binding peptide. For the colon model, one of the key challenges is distinguishing the polyp that is imaged. To perform longitudinal study of the polyps development, We have demonstrated multi-spectral *in-vivo* targeted vertical cross-sectional imaging of the polyps on the CPC;Apc mice whose rectums have prolapsed and there is no ambiguity of polyp location. The multi-spectral *in-vivo* imaging is potentially useful for

quantitatively measuring the dynamics performance of peptide. NIR dye labeled peptide channel fluorescence contrast ratio will be measured based on the anatomical illumination on the other channel with NIR dye staining. One image channel is for the Cy5.5-labeled peptide while another channel is for IRDye 800CW (Li-Cor Biosciences) stained morphology visualization. The chemical structure of the Cy5.5-labeled peptide, AKPGYLS, specific for colonic dysplasia is shown in Fig. 5.7A. The amino acid sequence AKPGYLS is connected by a GGGSK linker on the C-terminus to the Cy5.5 fluorophore to prevent steric hindrance. This targeting peptide was selected using in vivo phage display technology and validated using flow cytometry and small animal endoscopy (Karl Storz Veterinary Endoscopy, Goleta, CA) [36]. Control peptide, DNEPIAQ, was developed in house and tested using *in-vivo* near-infrared (NIR) endoscopy compared to various targeting peptides. The peptides were purified using a preparative-HPLC (Water Breeze HPLC, Milford, MA) and characterized with an ESI mass spectrometer (Micromass LCT Time-of-Flight mass spectrometer with electrospray). The purity (> 95%) of the peptides was assessed by analytical HPLC. A NIR dye IRDye 800CW (Li-Cor Biosciences) with anabsorption maximum at 774 nm and an emission maximum at 789 nm in water was selected to use as a background contrast agent for surrounding tissues. Excitation spectra of Cy5.5 conjugated peptides and IRDye 800CW were confirmed using a fluorescence spectrometer, as shown in Fig. 5.7B.

We use CPC;Apc mice that are genetically engineered to spontaneously develop pre-malignant colonic lesions similar to that seen in human disease.

Mice were cared for with approval of the University Committee on the Use and Care of Animals (UCUCA) at the University of Michigan and housed in specific pathogen-free conditions and supplied water *ad libitum* throughout the study.

(A)


(B)

Figure 5.8 – Administration and method for in-vivo multi-spectral vertical cross-sectional imaging on the prolapse area of CPC;Apc mouse colon. (A) Prolapse of five-month-old mouse; (B) *In-vivo* imaging on the prolapse area of 10-month-old CPC;Apc mouse colon.

Five-month-old mice may develop prolapse outside the colon, in Fig. 5.8A. For *in-vivo* targeted vertical cross-sectional imaging, five- to twelve-month-old CPC;Apc mice with prolapse (in Fig. 5.8B) were injected via tail vein with AKPGYLS-GGGSK-Cy5.5, 600 μM in 1× phosphate-buffered saline (PBS). The administration and methods are similar with the procedures shown in Fig. 5.4A. For multi-spectral *in-vivo* imaging, the peptide conjugate was allowed to circulate for 2 hours and 30 minutes, in Fig. 5.9. Mice were then injected with IRDye 800CW, 600 μM in PBS immediately prior to imaging at the prolapse area. After IRDye 800CW injection, as shown in Fig.5.8B, we started *in-vivo* multi-spectral targeted vertical cross-sectional imaging immediately with 2 mW of excitation at λ_{ex}= 671 nm and λ_{ex}= 785 nm. We imaged the prolapse area *in-vivo* for about 30 minutes to 1 hour immediately right after IRDye 800CW injection. After *in-vivo*

imaging, the mice were euthanized quickly. Prolapse, distal and proximal colon was extracted, washed with phosphate buffered saline (PBS), blotted dry, mounted on glass slides using 3M Vetbond tissue adhesive, and kept on ice shortly prior to imaging with the same multi-spectral imaging system. The control peptide, DNEPIAQ-GGGSK-Cy5.5, 600 µM in PBS, was tested in the same manner as the targeting peptide. After *in-vivo* and *ex-vivo* imaging, The tissues were then fixed with 10% buffered formalin for 24 hours, paraffin-embedded and sectioned into 10 µm thin slices and stained with hematoxylin and eosin (H&E). Histology was captured on an Axioskop2 upright microscope (Carl Zeiss Microimaging, Inc. Thornwood, NY).

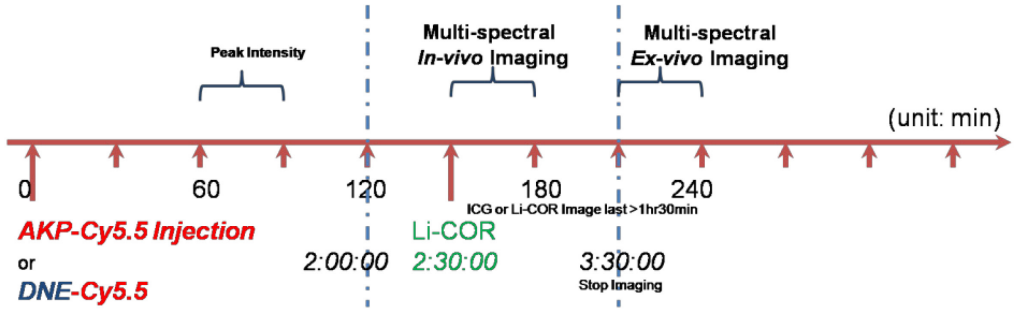

Figure 5.9 – Peptide administration and targeted in-vivo imaging procedure for prolapse of CPC;Apc mouse model. About 2 hours and 30 minutes after peptide-Cy5.5 injection, IRDye 800CW dye injection and later multi-spectral in-vivo imaging on the prolapse was performed.

5.3.2 *Ex-vivo* Imaging Results

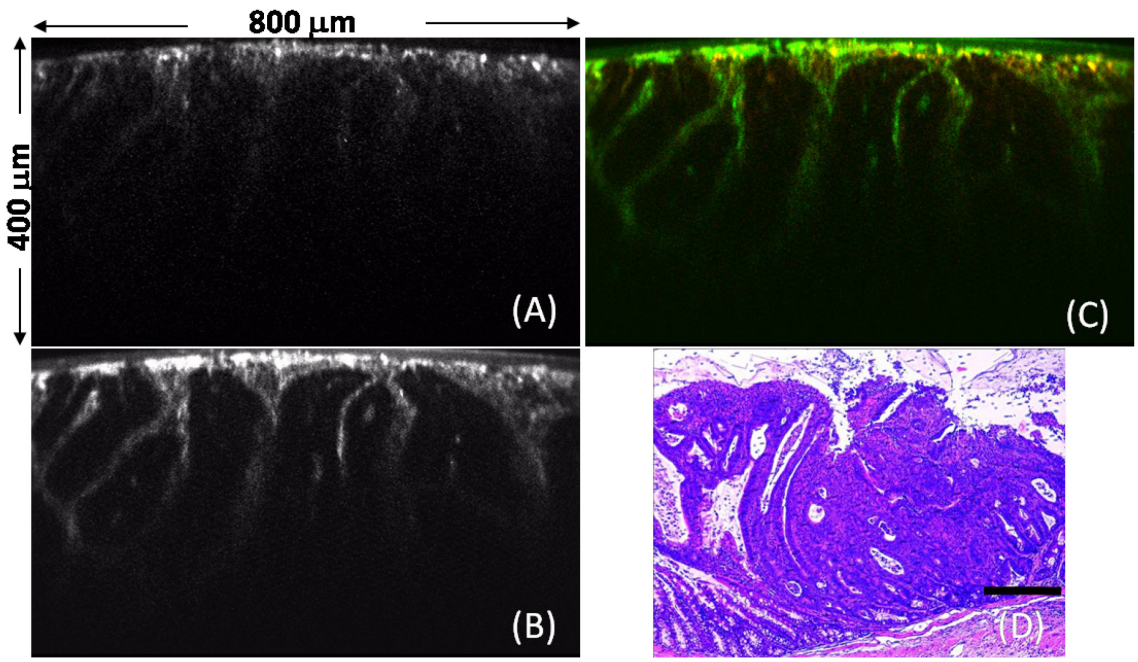

Figure 5.10 – Multi-spectral *ex-vivo* targeted vertical cross-sectional imaging on the dysplastic tissue of the mouse colon distal end. (C) is the merged pseudo-colored image of (A)&(B). (A) shows the AKP*-Cy5.5 (excitation λ_{ex}= 671 nm) specific bonding peptide channel; (B) shows the IRDye 800CW (excitation λ_{ex}= 785 nm) NIR dye stained morphology channel. (D) Corresponding histology (H&E), black color scale bar 100 µm.

Multi-spectral *ex-vivo* targeted vertical cross-sectional fluorescence images of colon show dysplastic crypts of mouse distal colon in the vertical orientation, Fig. 5.10, demonstrating the histology-like performance over a FOV of 800 µm (width) × 400 µm (depth). Fig. 5.10C is the merged pseudo-colored image of Fig. 5.10A&B. Fig. 5.10A shows the AKP*-Cy5.5 (excitation λex=671 nm) specific bonding peptide channel while Fig. 5.10B shows the IRDye 800CW (excitation λex=785 nm) NIR dye stained morphology channel. The arc seen at the top of this image is likely produced by the interface between the SIL and tissue that results from post-objective scanning. Multi-spectral *ex-vivo* targeted vertical cross-sectional fluorescence images of normal crypts on the mouse colon

proximal end are shown in Fig. 5.11, demonstrating the histology-like performance over a FOV of 800 μm (width) × 400 μm (depth). Vertically oriented dysplastic and normal crypts can be appreciated in the corresponding histology (H&E), scale bar 100 μm, Fig. 5.10D and Fig. 5.11D. We can distinguish the fluorescence signal intensity contrast by comparing the peptide channels from Fig. 5.10A and Fig. 5.11A.

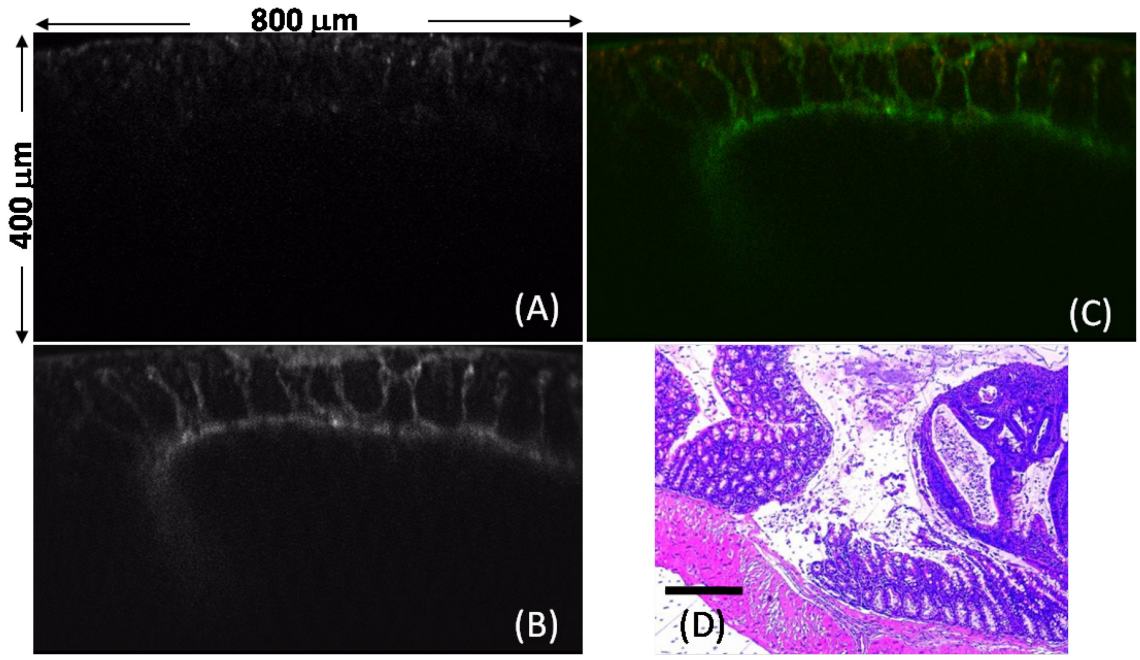

Figure 5.11 – Multi-spectral ex-vivo targeted vertical cross-sectional imaging on the normal tissue of the mouse colon proximal end. (A)-(C) show the images of normal crypts. (C) is the merged pseudo-colored image of (A)&(B). (A) shows the AKP*-Cy5.5 (excitation λ_{ex}= 671 nm) specific bonding peptide channel; (B) show the IRDye 800CW (excitation λ_{ex}= 785 nm) dye stained morphology channel. (D) Corresponding histology (H&E), scale bar 100 μm.

As shown in Fig. 5.12, the contrast from specific binding of the AKP*-Cy5.5 peptide can be appreciated by comparing the fluorescence signal intensity of the normal colonic mucosa with the one of dysplasia. Use of a specific binding

peptide AKP*-Cy5.5 allows for the transition from normal to pre-malignant mucosa to be visualized with high contrast using the same gain on the PMT. Compared to normal colonic mucosa, the NIR fluorescence (excitation λ_{ex}= 671 nm) intensity of dysplasia is >1.7 times. The peptide binds to cells in the epithelium (~150 to 200 μm), and tissue below is not expected to produce signal.

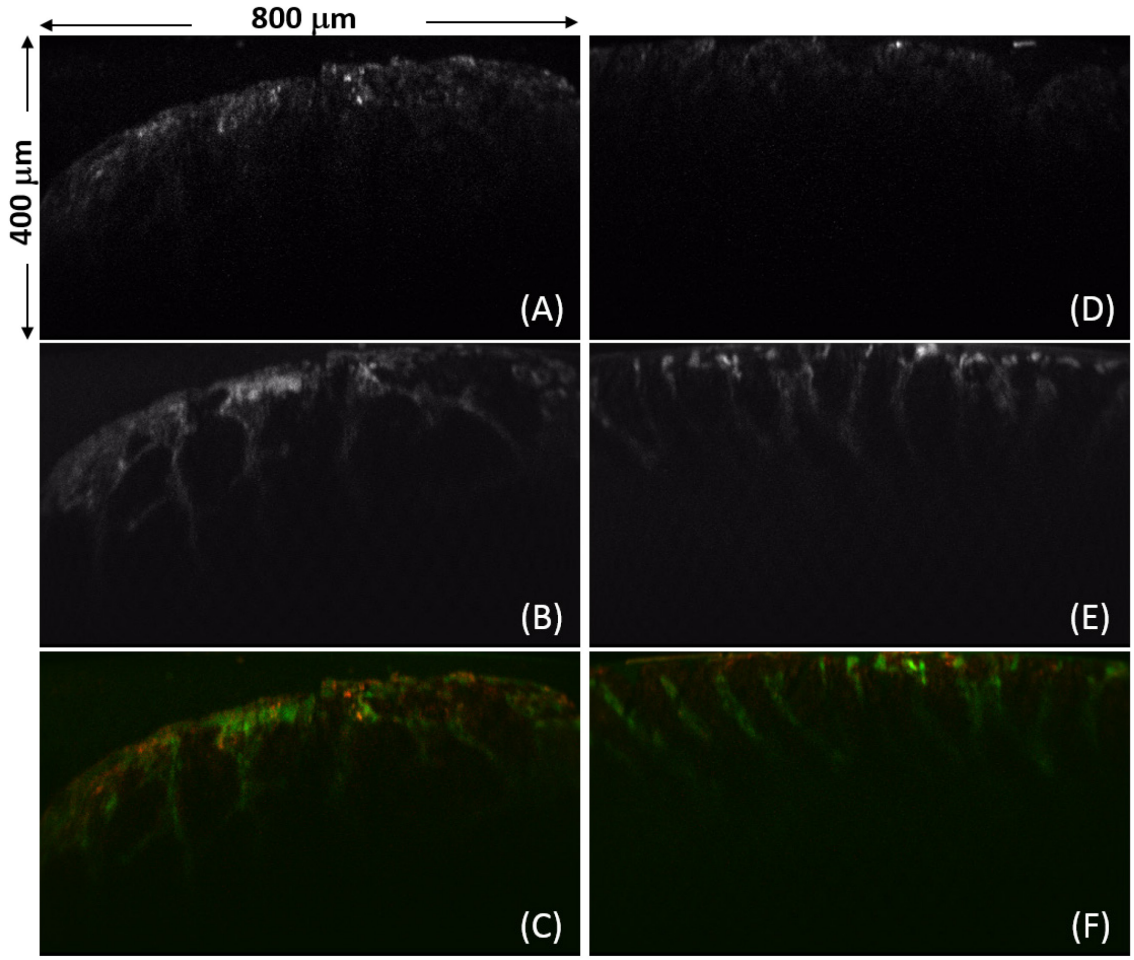

Figure 5.12 – Multi-spectral *ex-vivo* targeted vertical cross-sectional imaging on the mouse colon. (A)-(C) show the targeted vertical cross-sectional images of dysplastic crypts. (D)-(F) shows the targeted vertical cross-sectional images of normal crypts. (C) is the merged pseudo-colored image of (A)&(B). (F) is the merged pseudo-colored image of (D)&(E). (A)&(D) show the AKP*-Cy5.5 (excitation λ_{ex}= 671 nm) specific bonding peptide channel; (B)&(E) show the IRDye 800CW (excitation λ_{ex}= 785 nm) dye stained morphology channel.

5.3.3 *In-vivo* Imaging Results

Multi-spectral *in-vivo* targeted vertical cross-sectional fluorescence images of colon show dysplastic crypts of mouse prolapse in the vertical orientation, Fig. 5.10, demonstrating the histology-like performance over a FOV of 800 μm (width) × 400 μm (depth). Fig. 5.13C is the merged pseudo-colored image of Fig. 5.13A&B. Fig. 5.13A shows the AKP*-Cy5.5 (excitation λ_{ex}= 671 nm) specific bonding peptide channel while Fig. 5.13B shows the IRDye 800CW (excitation λ_{ex}=785 nm) NIR dye stained morphology channel.

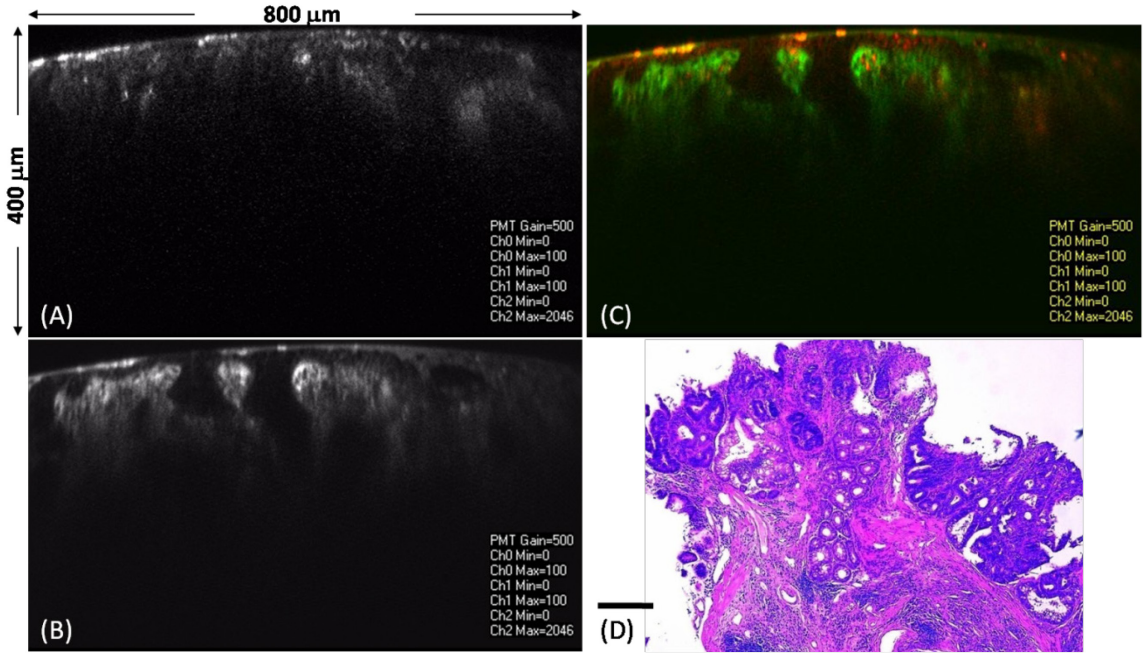

Figure 5.13 – Multi-spectral *in-vivo* targeted vertical cross-sectional imaging of dysplastic crypts on the mouse colon prolapse area. (C) is the merged pseudo-colored image of (A)&(B). (A) shows the AKP*-Cy5.5 (excitation λ_{ex}= 671 nm) specific targeting peptide channel; (B) shows the IRDye 800CW (excitation λ_{ex}= 785 nm) dye stained morphology channel. (D) Corresponding histology (H&E), black color scale bar 100 μm.

Multi-spectral *in-vivo* targeted vertical cross-sectional fluorescence images of normal crypts of the same mouse prolapse are shown in Fig. 5.14, demonstrating the histology-like performance over a FOV of 800 μm (width) × 400 μm (depth). Fig. 5.14C is the merged pseudo-colored image of Fig. 5.14A&B. Fig. 5.14A shows the AKP*-Cy5.5 (excitation λ_{ex} = 671 nm) specific binding peptide channel while Fig. 5.14B shows the IRDye 800CW (excitation λ_{ex} = 785 nm) NIR dye stained morphology channel. Vertically oriented dysplastic and normal crypts can be appreciated in the corresponding histology (H&E), scale bar 100 μm, Fig. 5.13D and Fig. 5.14D.

We can distinguish the fluorescence signal intensity contrast by comparing the peptide channels from Fig. 5.13A and Fig. 5.14A. As shown in Fig. 5.15, the contrast from specific binding of the AKP*-Cy5.5 peptide can be appreciated by comparing the fluorescence signal intensity of the normal colonic mucosa (Fig. 5.15A) with the one of dysplasia (Fig. 5.15D). Fig. 5.15C is the merged pseudo-colored image of Fig. 5.15A&B. Fig.5.15F is the merged pseudo-colored image of Fig. 5.15D&E. Fig. 5.15A&D show the AKP*-Cy5.5 (excitation λ_{ex}= 671 nm) specific binding peptide channel while Fig. 5.15B&E show the IRDye 800CW (excitation λ_{ex}= 785 nm) NIR dye stained morphology channel. Compared to normal colonic mucosa, the NIR fluorescence (excitation λ_{ex}= 671 nm) intensity of dysplasia on the peptide channel is > 1.7 times. The peptide binds to cells in the epithelium (~150 to 200 μm), and tissue below is not expected to produce signal.

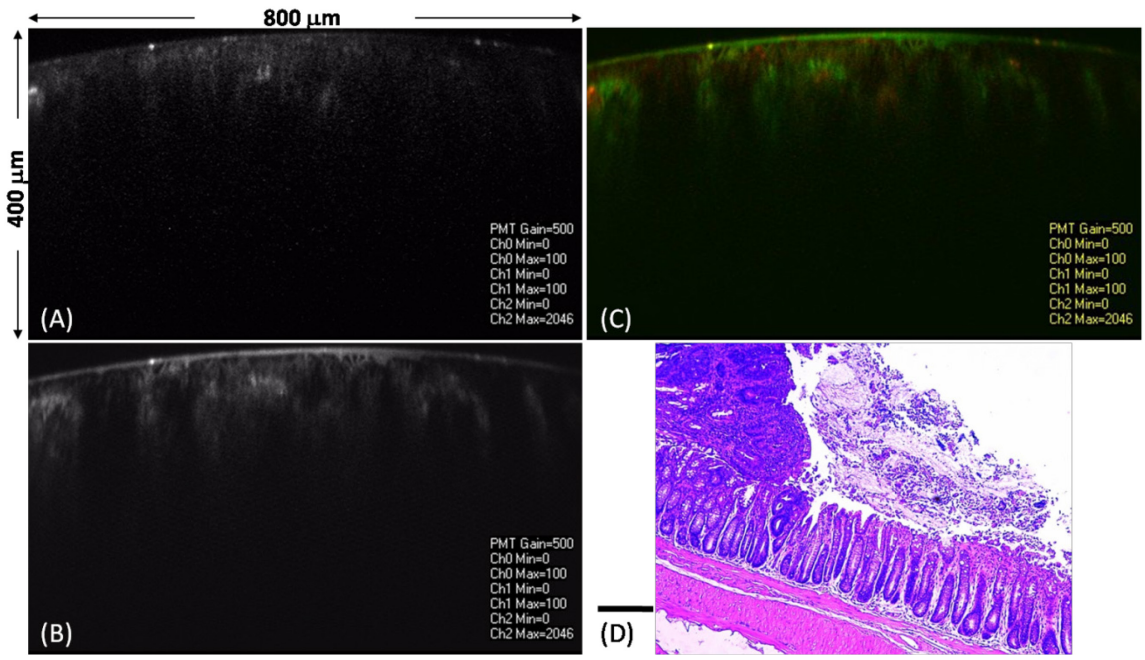

Figure 5.14 – Multi-spectral *in-vivo* targeted vertical cross-sectional imaging of normal crypts on the mouse colon prolapse area. (C) is the merged pseudo-colored image of (A)&(B). (A) shows the AKP*-Cy5.5 (excitation λ_{ex}= 671 nm) specific targeting peptide channel; (B) shows the IRDye 800CW (excitation λ_{ex}= 785 nm) dye stained morphology channel. (D) Corresponding histology (H&E), black color scale bar 100 µm.

Multi-spectral *in-vivo* targeted vertical cross-sectional fluorescence images of the border between dysplastic crypts and normal crypts on mouse prolapse are shown in Fig. 5.16, demonstrating the histology-like performance over a FOV of 800 µm (width) × 400 µm (depth). Fig. 5.16C is the merged pseudo-colored image of Fig. 5.16A&B. Fig. 5.16F is the merged pseudo-colored image of Fig. 5.16D&E. Fig. 5.16A&D show the AKP*-Cy5.5 (excitation λ_{ex}= 671 nm) specific binding peptide channel while Fig. 5.16B&E show the IRDye 800CW (excitation λ_{ex}= 785 nm) NIR dye stained morphology channel. Use of a specific binding peptide allows for the transition from normal to pre-malignant mucosa to be visualized with high contrast using the same gain on the PMT.

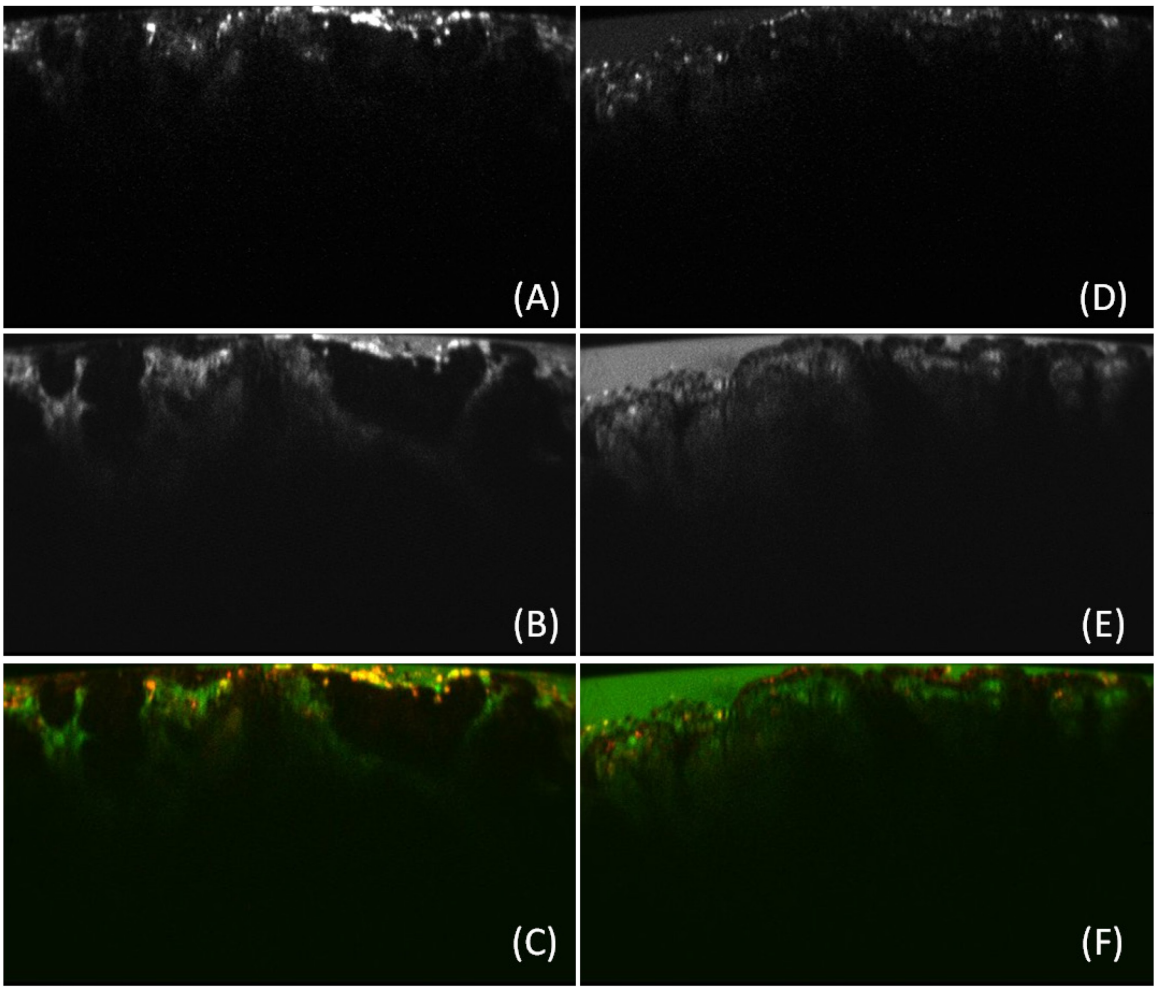

Figure 5.15 – Multi-spectral in-vivo targeted vertical cross-sectional imaging comparison between dysplastic and normal crypts on the mouse colon prolapse. (A)-(C) show the targeted vertical cross-sectional images of dysplastic crypts. (D)-(F) shows the targeted vertical cross-sectional images of normal crypts. (C) is the merged pseudo-colored image of (A)&(B). (F) is the merged pseudo-colored image of (D)&(E). (A)&(D) show the AKP*-Cy5.5 (excitation λ_{ex}= 671 nm) specific bonding peptide channel; (B)&(E) show the IRDye 800CW (excitation λ_{ex}= 785 nm) dye stained morphology channel.

As shown in Fig. 5.16A&D, the contrast from specific binding of the AKP*-Cy5.5 peptide can be appreciated by comparing the fluorescence signal intensity of the normal colonic mucosa with the one of dysplasia on the border (Fig. 5.16A&D). Compared to normal colonic mucosa, the NIR fluorescence (excitation λ_{ex}= 671 nm) intensity of dysplasia is > 1.7 times. The peptide binds to cells in

the epithelium (~150 to 200 μm), and tissue below is not expected to produce signal.

Multi-spectral *in-vivo* targeted vertical cross-sectional fluorescence images of the border between dysplastic crypts and normal crypts on mouse prolapse with control peptide DNE*-Cy5.5 are shown in Fig. 5.17, demonstrating the histology-like performance over a FOV of 800 μm (width) × 400 μm (depth). Fig. 5.17C is the merged pseudo-colored image of Fig. 5.17A&B. Fig. 5.17A shows the DNE*-Cy5.5 (excitation λ_{ex}= 671 nm) control peptide channel while Fig. 5.17B shows the IRDye 800CW (excitation λ_{ex}= 785 nm) NIR dye stained morphology channel. Use of a control peptide allows for the transition from normal to pre-malignant mucosa to be visualized with low contrast using the same gain on the PMT. As shown in Fig. 5.17A, the contrast from specific binding of the AKP*-Cy5.5 peptide can be appreciated by comparing the fluorescence signal intensity of the normal colonic mucosa with the one of dysplasia on the border (Fig. 5.17A). Compared to normal colonic mucosa, the NIR fluorescence (excitation λ_{ex}=671 nm) intensity of dysplasia is ~ 1.4 times, much lower than the specific binding peptide AKP*-Cy5.5. The peptide binds to cells in the epithelium (~150 to 200 μm), and tissue below is not expected to produce signal.

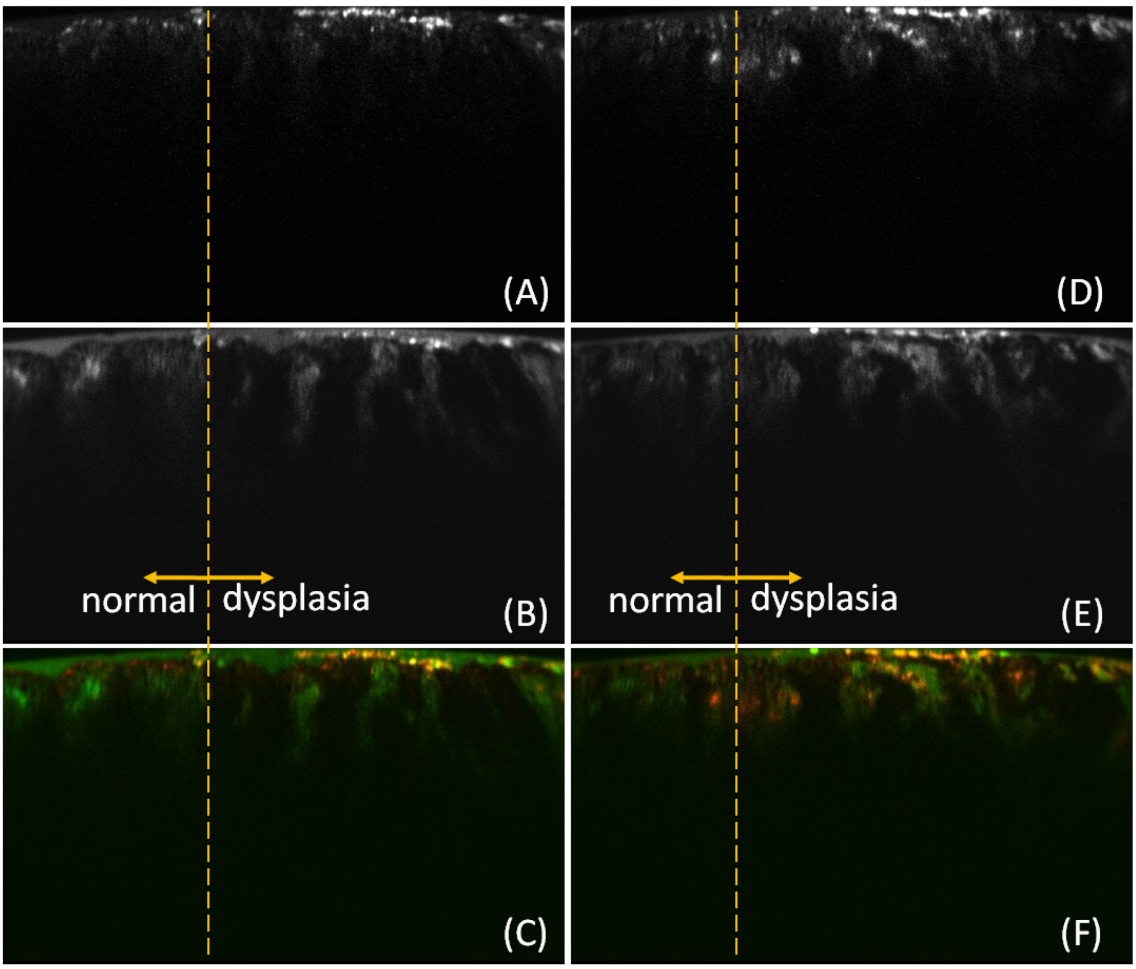

Figure 5.16 – Multi-spectral *in-vivo* targeted vertical cross-sectional imaging of the border between dysplastic and normal crypts on the mouse colon prolapse area with specific peptide AKP*-Cy5.5. (C) is the merged pseudo-colored image of (A)&(B). (F) is the merged pseudo-colored image of (D)&(E). (A)&(D) show the AKP*-Cy5.5 (excitation λ_{ex}= 671 nm) specific bonding peptide channel; (B)&(E) show the IRDye 800CW (excitation λ_{ex}= 785 nm) dye stained morphology channel.

An alternative control has been demonstrated by imaging the squamous skin tissue and the border between squamous and the dysplasia area. Multi-spectral *in-vivo* targeted vertical cross-sectional fluorescence images of squamous and the border between squamous and dysplastic crypts on mouse prolapse with specific binding peptide AKP*-Cy5.5 are shown in Fig. 5.18,

demonstrating the histology-like performance over a FOV of 800 μm (width) × 400 μm (depth).

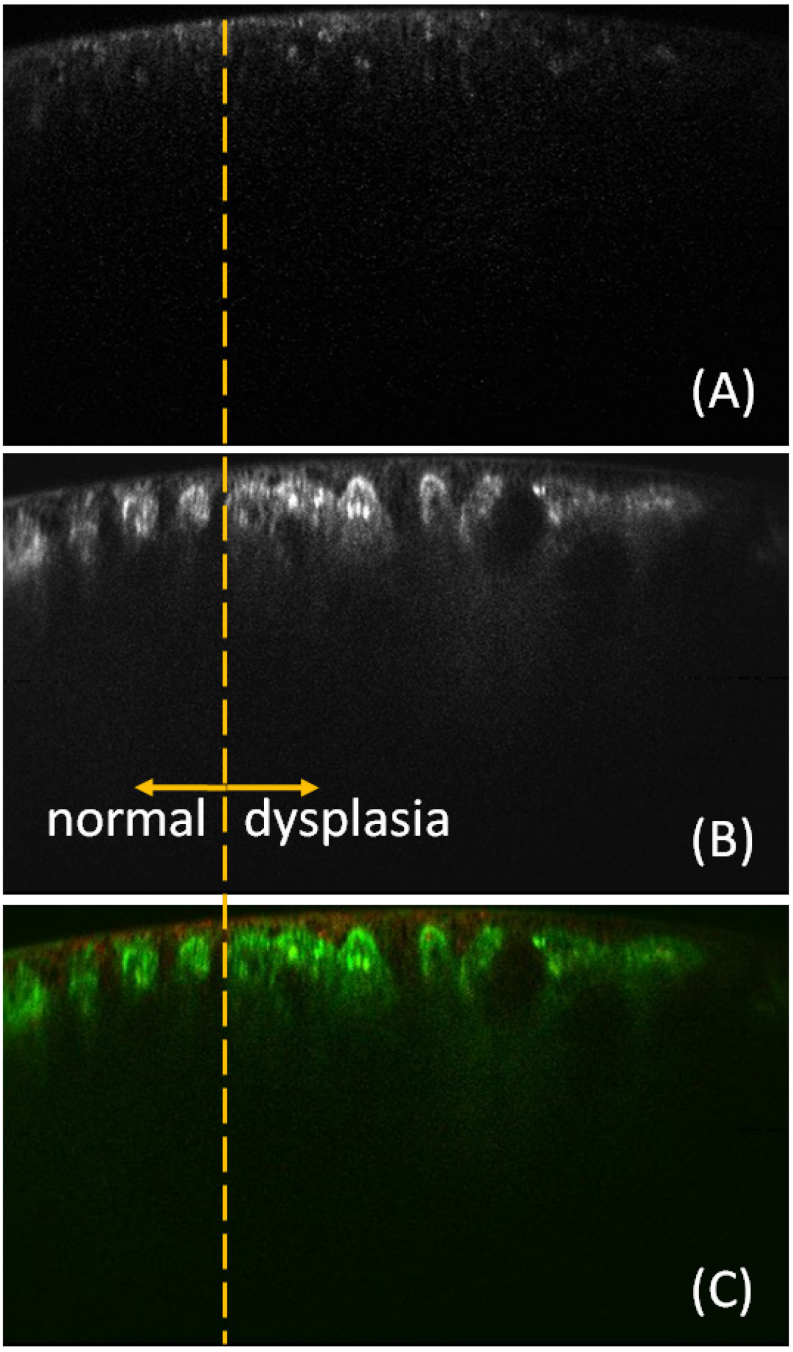

Figure 5.17 – Multi-spectral *in-vivo* targeted vertical cross-sectional imaging of the border between dysplastic and normal tissue on the mouse colon prolapse area with control peptide DNE*-Cy5.5. (C) is the merged pseudo-colored image of (A)&(B). (A) shows the DNE*-Cy5.5 (excitation λ_{ex}= 671 nm) peptide channel; (B) show the IRDye 800CW (excitation λ_{ex}= 785 nm) dye stained morphology channel.

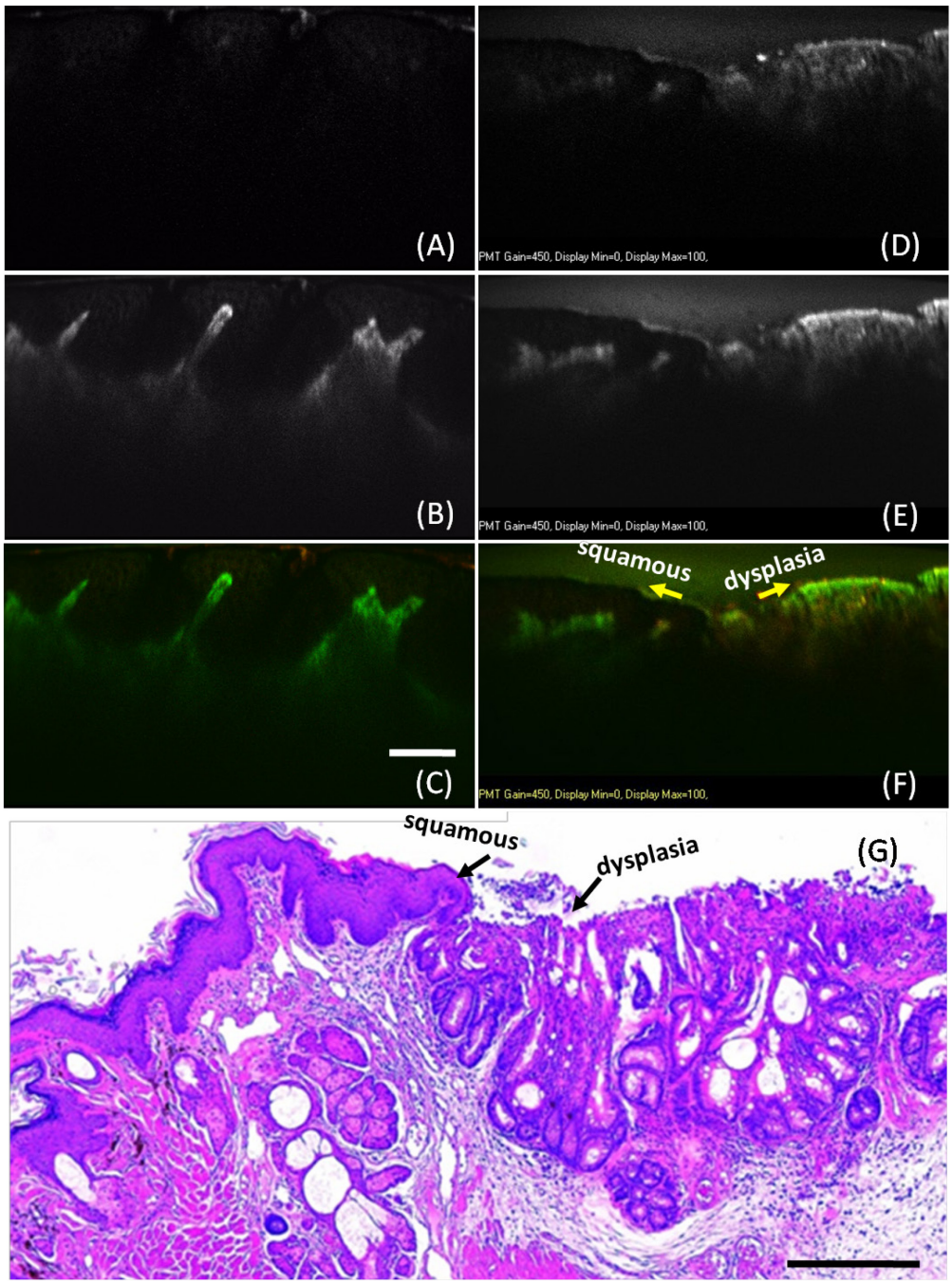

Figure 5.18 – Multi-spectral *in-vivo* targeted vertical cross-sectional imaging of the squamous on the mouse prolapse skin area with peptide AKP*-Cy5.5. (C) is the merged pseudo-colored image of (A)&(B), white color scale bar in (C) is 100 µm. (D) is the merged pseudo-colored image of (E)&(F). (A)&(D) show the AKP*-Cy5.5 (excitation λ_{ex}= 671 nm) specific binding peptide channel. (B)&(E) show the IRDye 800CW (excitation λ_{ex}= 785 nm) dye stained morphology channel. (A)-(C) show the images of the squamous skin tissue (D)-(F) show the images of the border between squamous and displastic crypts. (D) Corresponding histology (H&E), black color scale bar 500 µm.

Fig. 5.18C is the merged pseudo-colored image of Fig. 5.18A&B. Fig. 5.18F is the merged pseudo-colored image of Fig. 5.18D&E. Fig. 5.18A&D show the AKP*-Cy5.5 (excitation λ_{ex}= 671 nm) specific binding peptide channel while Fig. 5.18B&E show the IRDye 800CW (excitation λ_{ex}= 785 nm) NIR dye stained morphology channel. NIR dye stained morphology channel. Use of a specific binding peptide allows for the transition from squamous to pre-malignant mucosa to be visualized with high contrast using the same gain on the PMT. As shown in Fig. 5.18A, the binding of the AKP*-Cy5.5 peptide to squamous tissue is minimum according to the fluorescence signal intensity. As shown in Fig. 5.18D-F, the contrast from specific binding of the AKP*-Cy5.5 peptide can be appreciated by comparing the fluorescence signal intensity of the squamous with the one of dysplasia on the border (Fig. 5.18D-F). Compared to squamous, the NIR fluorescence (excitation λ_{ex}= 671 nm) intensity of dysplasia is > 10 times, much higher than the contrast between dysplasia and normal using specific binding peptide AKP*-Cy5.5. The peptide has minimum binding to the squamous tissue. The peptide binds to cells in the epithelium (~ 150 to 200 μm), and tissue below is not expected to produce signal.

5.4 Fluorescence Contrast Ratio of Targeted Vertical Cross-sectional Imaging

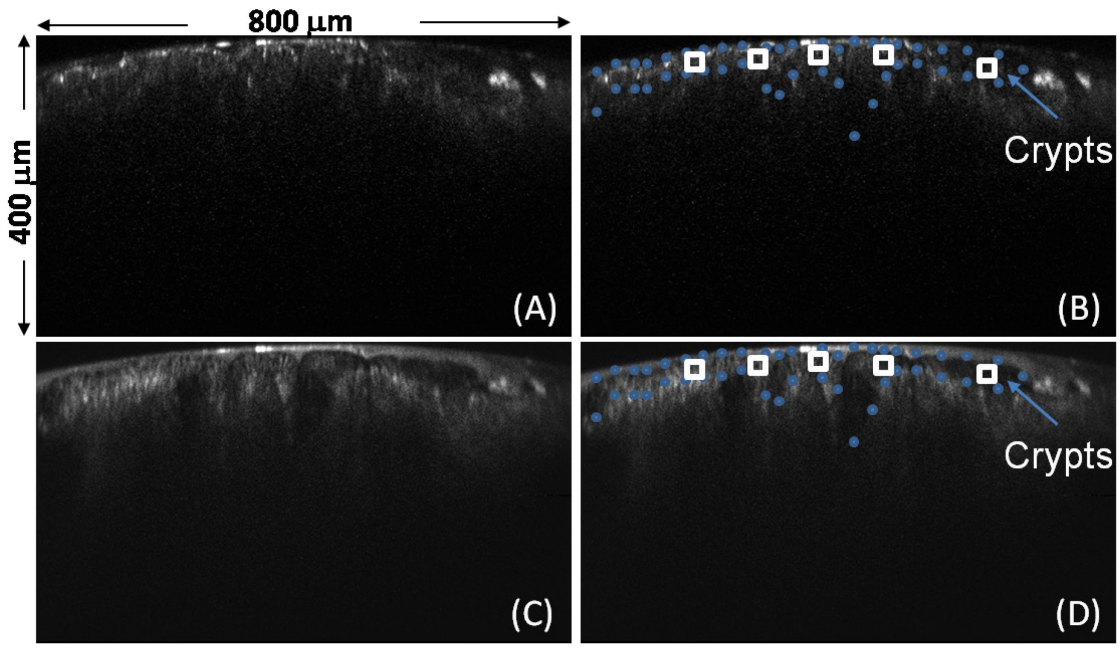

Figure 5.19 – Fluorescence contrast ratio measurement approach for multi-spectral *in-vivo* vertical cross-sectional imaging. (A)&(C) are original images on normal crypts of the mouse prolapse. (B)&(D) are images with region-of-interest demonstrating the measurement. (A) shows the DNE*-Cy5.5 (excitation λ_{ex}= 671 nm) control peptide channel; (C) shows the IRDye 800CW (excitation λ_{ex}= 785 nm) dye stained morphology channel. Contour of the crypts area can be found in the morphology image channel (C). blue color circles indicate the whole area on the peptide image channel (B). White color boxes indicate the five sites chosen for fluorescence signal contrast ratio measurement for muli-spectral *in-vivo* images.

The multi-spectral targeted vertical cross-sectional images are analyzed by selecting 10 representative images of dysplastic and normal crypts during each 5 minutes period from the 30 minutes video stream in both fluorescence channels based on the following criteria: (1) minimum motion artifact, (2) lack of stool or excess mucus preventing contact with the mucosa, and (3) recognizable crypt morphology. There will be n = 30 dysplastic crypts area and n = 30 normal crypts area in total for fluorescence contrast ratio measurement. The fluorescence signal intensity will be calculated by taking the mean of a pixel array corresponding to a 10 × 10 μm^2 square region within the colonocyte layer for 5

sites within each image. The signal noise will be calculated by taking the standard deviation of the values in this pixel array. The fluorescence contrast ratio will be obtained from the ratio of the mean dysplastic crypts to the mean normal crypts fluorescence intensity.

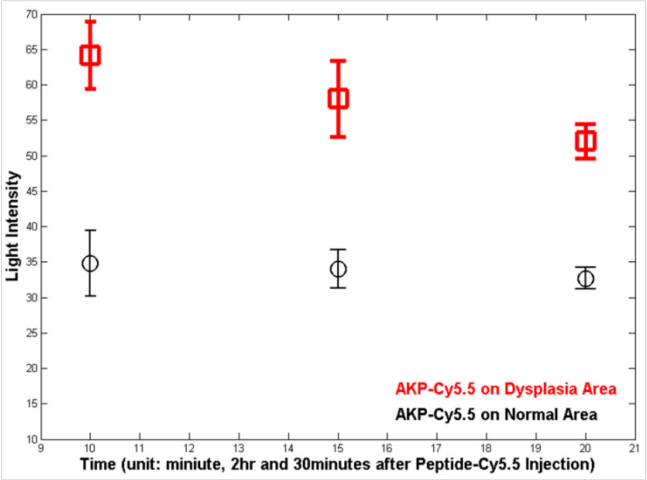

Figure 5.20 – Multi-spectral *in-vivo* vertical cross-sectional imaging specific peptide AKP*-Cy5.5 fluorescence signal intensity versus time.

The fluorescence contrast ratio measurement method has been applied to both specific binding peptide AKP* and control peptide DNE*. The fluorescence signal intensity of dysplastic crypts and normal crypts versus time results for AKP* are shown in Fig. 5.20. The fluorescence signal intensity of dysplastic crypts and normal crypts versus time results for DNE* are shown in Fig. 5.21. Multi-spectral images were collected from IRDye 800CW dye injection about 2 hours and 30 minutes later from peptide-Cy5.5 injection. The fluorescence signal intensity decays along the timeline, as shown in Fig. 5.20 and Fig. 5.21.

With AKP* specific binding peptide, the fluorescence signal intensity of the normal crypts decays much slower than the one of dysplastic crypts. Because

the AKP* specific binding peptide only has minimum non-specific binding to the normal crypts. The non-specific binding intensity can be viewed as "background" signal. In comparison, with the DNE* control peptide, the decay trends of dysplastic and normal crypts are nearly parallel since control peptide is non-specific binding to both types of crypts.

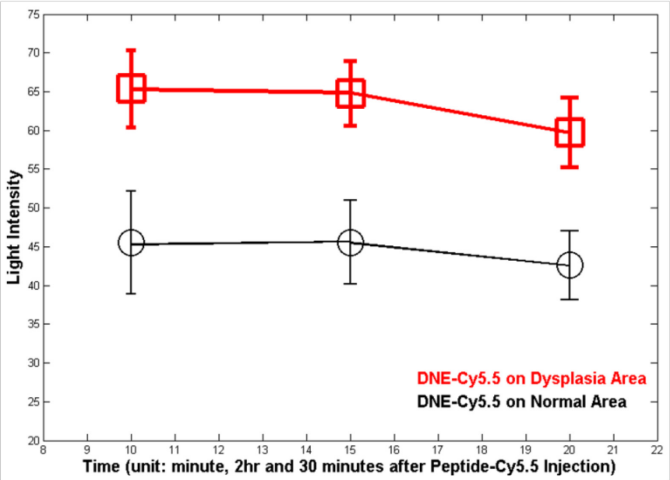

Figure 5.21 – Multi-spectral *in-vivo* vertical cross-sectional imaging control peptide DNE*-Cy5.5 fluorescence signal intensity versus time.

Biomarker	Dysplastic Crypts (n=30) Intensity		Normal Crypts (n=30) Intensity		Fluorescence Contrast Ratio
	mean	s.t.d.	mean	s.t.d.	
AKP* specific peptide	60.514	6.508	33.846	3.582	1.789
DNE* control peptide	62.684	5.608	44.399	5.611	1.411
IRDye 800CW staining	42.517	4.305	39.102	5.124	1.087

Table 5.1 – Muli-spectral *in-vivo* images fluorescence contrast ratio measurement.

The mean fluorescence contrast ratio is calculated based on the mean fluorescence signal intensities of dysplastic and normal crypts. As shown in

Table 5.1, with specific binding peptide AKP*, the fluorescence signal intensity of dysplastic crypts is 60.514 ± 6.508, while the fluorescence signal intensity of normal crypts is 33.846 ± 3.582. The fluorescence contrast ratio for specific binding peptide AKP* is 1.789, compared to 1.411 with control peptideDNE*. On the morphology channel, with the IRDye 800CW dye staining, dysplastic, normal crypts and other tissue types have nearly similar fluorescence signal intensities and decay trends. The fluorescence contrast ratio for IRDye 800CW dye staining is 1.087, in Table 5.1.

5.5 Signal Intensity versus Depth of Targeted Vertical Cross-sectional Imaging

The superior dynamic range (Z-axis) of the dual axes confocal endomicroscope system design enables deep imaging in the bulk tissue specimens. For example, the fluorescence signal intensity was analyzed based on the 785nm fluorescence channel in Fig. 5.10, which a multi-spectral *in-vivo* targeted vertical cross-sectional fluorescence image on the dysplastic crypts with specific peptide AKP*-Cy5.5. We calculate the mean value and standard variation of the fluorescence signal intensity based on the signal in the 30 x 30 μm^2 area every 30 μm along the Z-axis. The fluorescence signal intensity versus depth (Z-axis) for Fig. 5.10 is shown in Fig. 5.22. In Fig. 5.22, the fluorescence signal intensity decrease with increasing depth. However, at depth of up to 300 μm, there is still good signal-to-noise ratio which is sufficient for us to tell the morphology structure. In this study, the thickness of the bulk distal colon tissue from mouse is relatively thinner than that of human colon tissue. In the future, we

should be able to demonstrate the full capability of deep imaging with dual axes confocal endomicroscope.

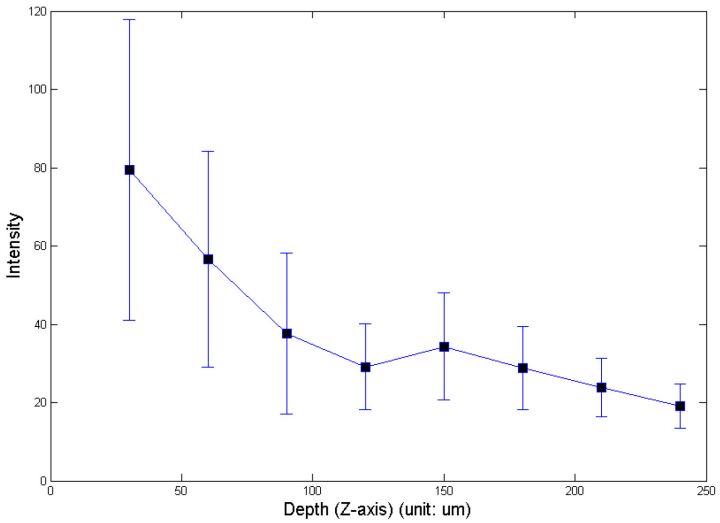

Figure 5.22 – Fluorescence signal intensity versus depth for IRDye 800CW dye stained channel (λ_{ex}= 785 nm) of the multi-spectral *in-vivo* vertical cross-sectional imaging with specific peptide AKP*-Cy5.5 in Fig. 5.10.

Chapter 6

Conclusions and Future Work

6.1 Summary of Dissertation

In the research performed in this dissertation, a multi-spectral dual axes confocal endomicroscope imaging system has been successfully developed and demonstrated *in-vivo* imaging in a mouse model of spontaneous colorectal cancer. Targeted vertical cross-sectional images with a large field-of-view have been collected using excitation at λ_{ex}= 671 nm and 785 nm. Several novel scan engines have been demonstrated in the miniature endomicroscope to produce both lateral and axial scanning, including MEMS device based meso-scale "proof-of-concept" mechatronic system and monolithic 2D XZ-plane MEMS scanners (electrostatic and thin-film piezoelectric). Longitudinal studies in the mouse model have been demonstrated using this targeted in-vivo imaging system. A summary of all the achievements are described in the following sections.

6.1.1 Vertical Cross-sectional Scan Engine Development

One of our aims achieved in this research work is the development of novel scan engines for vertical cross-sectional (XZ-plane) scan (in lissajous or raster scan pattern) in the miniature endomicroscope. This dissertation fully details different approaches to realize both X-axis lateral high speed (~ 3 KHz) tilting and out-of-plane translational (Z-axis, up to 10 Hz) motion. A meso-scale mechatronic system is proposed for a handheld “proof-of-concept” system, which consists of 1D electrostatic in-plane comb-drive based MEMS X-axis lateral resonant scanner and a bulk PZT based Z-axis actuator. Based on the same strategy, 2D electrostatic MEMS XY-plane scanner integrated with Z-axis actuator will provide 3D scan (2D *en-face* imaging with Z-axis stacking). The most challenging task is to realize XZ-plane scanning in a single MEMS chip with small footprint (< 3 × 3 mm^2). A 2D electrostatic in-plane comb-drive based MEMS XZ-plane resonant scanner has been developed. Characteristic measurements demonstrate the vertical cross-sectional scanning in a stable lissajous scan pattern.

By exploiting the advantages of thin-film piezoelectric materials and multi-fold unimorph beams based mechanisms, a novel thin-film PZT based monolithic MEMS XZ-plane scanner has been proposed as a comprehensive solution for the vertical cross-sectional scanning. In addition, 3D scanning can be performed by the same MEMS chip with differential driving on the outer frame for both translational (Z-axis) and lateral (Y-axis) motions. The unique properties of thin-film PZT materials enable the MEMS device to perform both large tilting angle and translational displacement at ultra-low driving voltage (< 20 V) and extremely

low driving current with broad bandwidth (up to 300 Hz). The development of this advanced field of thin-film PZT based MEMS devices will be a significant step in developing scanners for future endomicroscopes.

6.1.2 Dual Axes Confocal Endomicroscope System Integration

The MEMS device based XZ-plane scan engines enable the development offiber coupled miniature endomicroscope with dual axes confocal architecture. This dissertation details the system-level integration work of a multi-spectral dual axes confocal endomicroscope, fiber coupled illumination/collection optics development, and data acquisition system. Optical ray-tracing simulation has been demonstrated for imaging system design and optimization. We utilized achromatic lens based fiber coupled collimators for multi-spectral imaging with minimum aberration. The single mode fibered coupled WDM beam combiner system integrates the 671 nm and 785 nm solid-state diode cw laser into a multi-spectral system. A custom-made fiber coupled cage system based fluorescence collection unit has also been developed. Control and image reconstruction program has been developed for *in-vivo* imaging with up to 10 frames per second. Based on the phantom and dye-stained bulk tissue specimens, detailed specifications, such as lateral/axial resolution and XZ-plane FOV, were further characterized.

6.1.3 Multi-spectral *In-vivo* Targeted Vertical Cross-sectional Imaging

The major accomplishment of this dissertation is the achievement of multi-spectral in-vivo targeted vertical cross-sectional imaging in the CPC;Apc mouse model of spontaneous colorectal cancer. Systemic administration of dysplasia specific binding peptides has been performed in this mouse. Using the handheld "proof-of-concept" dual axes confocal endomicroscope, we have successfully performed longitudinal NIR multi-spectral *in-vivo* imaging of the epithelium in mouse colon. The multi-spectral images consist of two channels: one channel is for molecular imaging of the fluorescent labeled peptide, the other one is for anatomical structure illustration. With large XZ-plane FOV (800 × 400 um^2) and sub-cellular resolution (< 5 μm), the system is able to distinguish the differentiation between disease and normal tissue, and acquire images of the border *in-vivo*. In this research, multi-spectral *in-vivo* vertical cross-sectional images were further analyzed for fluorescence signal contrast ratio between dysplastic and normal tissue specimens.

In summary, vertical cross-sections with histology-like images have been collected using novel dual axes confocal endomicroscope architecture. Multi-spectral targeted imaging has been demonstrated *in-vivo* in a small animal model of spontaneous colorectal cancer with fluorescent labeled peptides. The novel monolithic MEMS XZ-plane scanners and integrated advanced optical imaging system promises to have high impact in future MEMS device based endomicroscopes for biomedical imaging.

6.2 Future Research and Applications

We have shown that vertical cross-sectional images of colonic epithelium can be collected *in-vivo* with a dual axes confocal endomicroscope with miniature form factor. The future direction of this research will focus on further miniaturization, expansion of multi-spectral imaging capabilities, and *in-vivo* imaging in mouse models of disease and in human patients. Based on the advanced monolithic MEMS 3D scanners, the dual axes endomicroscope can be packaged into OD5mm or smaller size, in Fig. 6.1.

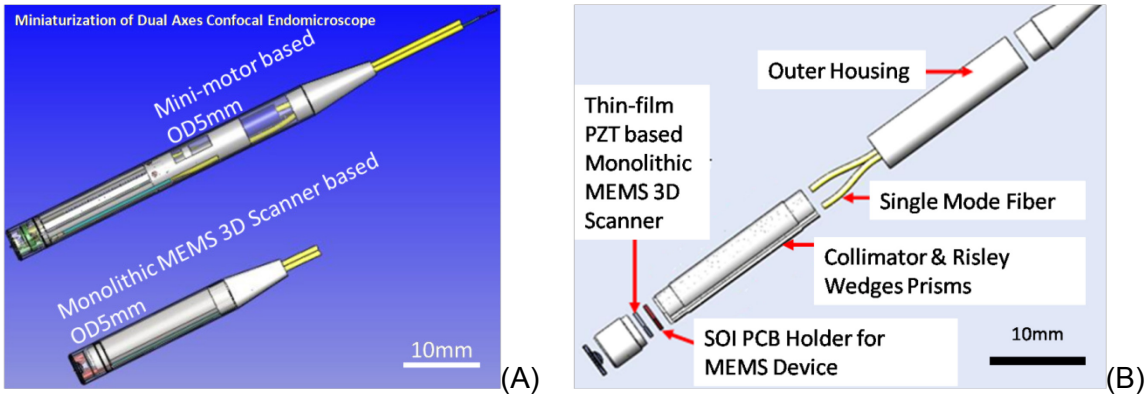

Figure 6.1 – Miniaturization of dual axes confocal endomicroscope. (A) Comparison between mini-motor based OD5mm endomicroscope and monolithic MEMS 3D scanner based OD5mm endomicroscope. (B) Schematic design of the OD5mm endomicroscope with thin-film PZT based monolithic MEMS 3D scanner.

Using advanced micro-optics, the collimating system will be optimized and packaged to a compact system with shorter length. Multi-spectral imaging system will be upgraded to four-color or more wavelengths. Two potential optics designs will be used for the next generation dual parabola based multi-spectral dual axes endomicroscope, in Fig. 6.2. In the first design, in Fig. 6.2A, the light out of fiber can be directly collimated by the backside parabolic mirror after being reflected by prisms. The monolithic 3D MEMS scanner will steer the illumination and

collection beams for 3D imaging. An alternative optics design, in Fig. 6.2B, is based on a combo 3D MEMS scan engine, which integrates MEMS 2D lateral scanner and 1D axial scanner for XY-plane and Z-axis on the opposite ends respectively. Compared to the design with the monolithic 3D MEMS scanner, the wiring will be more complicated in the combo MEMS 3D scanner based design, which is a backup plan in the future.

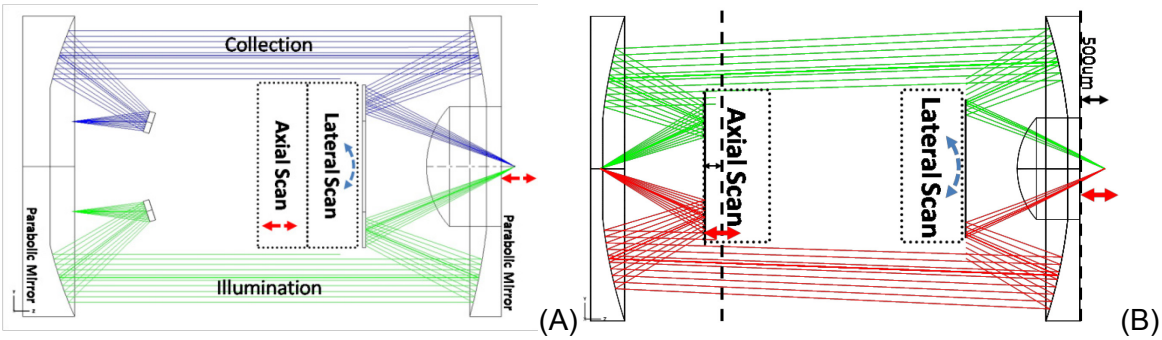

Figure 6.2 – OD5mm dual parabola based multi-spectral dual axes confocal endomicroscope optics design ray-tracing in ZEMAX. (A) Monolithic 3D MEMS scanner based OD5mm endomicroscope. (B) Combo 3D MEMS scan engine based OD5mm endomicroscope. The combo 3D MEMS scan engine consists of a 2D lateral scanner close to the solid immersion lens and a 1D axial scanner on the opposite side.

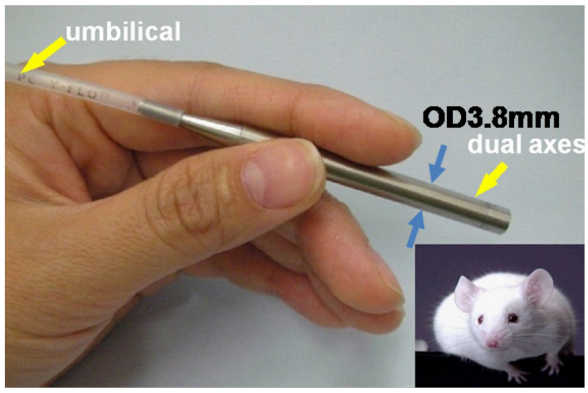

Figure 6.3 – A OD3.8mm miniature multi-spectral *intra-vital* dual axes confocal endomicroscope can be used for broader *in-vivo* imaging application in mice, such as brain, oropharynx, and skin.

With a much smaller package, the dual axes endomicroscope can be used for a broader range of *in-vivo* imaging applications. For example, the OD3.8mm dual axes endomicroscope will be used for *in-vivo* imaging in the colon of mice model, in Fig. 6.3. With a more compact package, the dual axes confocal endomicroscope can be used as an intra-vital imaging tool for other organs in the mouse, such as brain, oropharynx, and skin.

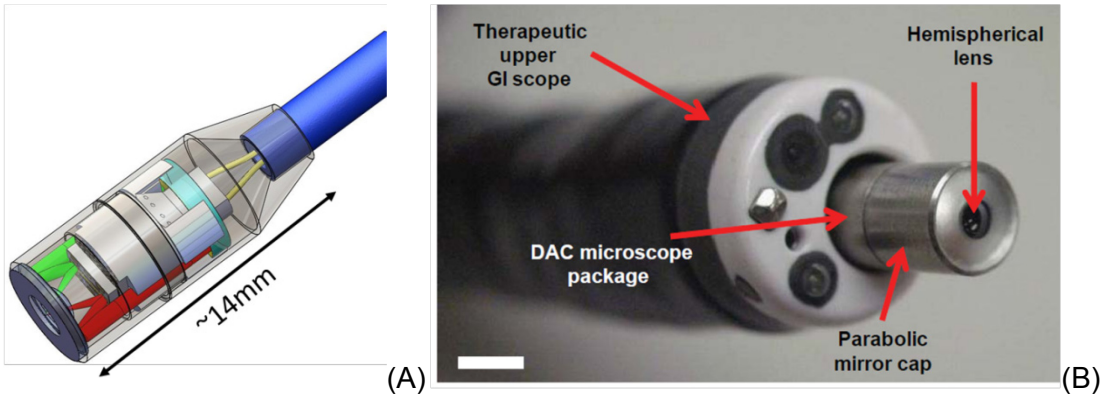

(A) (B)

Figure 6.4 – OD5mm miniature multi-spectral dual axes confocal endomicroscope for *in-vivo* imaging in the clinic. (A) Schematic design of OD5mm dual axes confocal endomicroscope, the rigid part length is ~14 mm. (B) OD5mm dual axes confocal endomicroscope can be passed through the 6mm diameter instrument channel of an Olympus therapeutic upper GI scope, scale bar is 5mm.

Another important application of the miniature dual axes confocal endomicroscope will be for the in-vivo imaging in the clinic. Based on the dual parabolic mirror design, the packaging of the multi-spectral dual axes confocal endomicroscope can be miniaturized to OD5mm with less than 20 mm of rigid length, Fig. 6.4A. This size is compatible with the instrument channel of an Olympus therapeutic upper GI endoscope, Fig. 6.4B. *In-vivo* images can be collected to perform early cancer staging, assess effectiveness of drug delivery,

and perform in-situ histology in hollow organs, such as colon, esophagus, and stomach.

To summarize, a multi-spectral dual axes confocal endomicroscope has been developed and targeted *in-vivo* vertical cross-sectional images have been demonstrated *in-vivo* in the colon of a mouse model of spontaneous colorectal cancer. In the future, additional miniaturization can be achieved with more compact axial and lateral scanners developed with MEMS technology. Also, multi-spectral imaging can be achieved with additional wavelengths over the visible and NIR spectral regime. The research has exciting potential for *in-vivo* imaging in two distinct areas. The first is intra-vital multi-spectral imaging in small animal models of human disease. Another area of impact can be made through further development of the miniature multi-spectral dual axes confocal endomicroscope for clinical imaging of human disease.

References

[1] R. S. Cotran, *et al.*, "Robbins and Cotran Pathologic Basis of Disease," 7th ed, Saunders, Philadelphia, PA (2005).

[2] T. D. Wang*, et al.*, "Functional imaging of colonic mucosa with a fibered confocal microscope for real-time in vivo pathology," *Clin Gastroenterol Hepatol,* vol. 5, pp. 1300-5, Nov 2007.

[3] R. Kiesslich*, et al.*, "Confocal laser endoscopy for diagnosing intraepithelial neoplasias and colorectal cancer in vivo," *Gastroenterology,* vol. 127, pp. 706-13, Sep 2004.

[4] H. J. Shin*, et al.*, "Fiber-optic confocal microscope using a MEMS scanner and miniature objective lens," *Opt Express,* vol. 15, pp. 9113-22, Jul 23 2007.

[5] C. L. Arrasmith*, et al.*, "MEMS-based handheld confocal microscope for in-vivo skin imaging," *Opt Express,* vol. 18, pp. 3805-19, Feb 15 2010.

[6] J. K. Kim*, et al.*, "Fabrication and operation of GRIN probes for in vivo fluorescence cellular imaging of internal organs in small animals," *Nat Protoc,* vol. 7, pp. 1456-69, Aug 2012.

[7] N. Callamaras and I. Parker, "Construction of a confocal microscope for real-time x-y and x-z imaging," *Cell Calcium,* vol. 26, pp. 271-9, Dec 1999.

[8] W. Gobel*, et al.*, "Imaging cellular network dynamics in three dimensions using fast 3D laser scanning," *Nat Methods,* vol. 4, pp. 73-9, Jan 2007.

[9] H. Mansoor*, et al.*, "Vertical optical sectioning using a magnetically driven confocal microscanner aimed for in vivo clinical imaging," *Opt Express,* vol. 19, pp. 25161-72, Dec 5 2011.

[10] K. K. Ghosh*, et al.*, "Miniaturized integration of a fluorescence microscope," *Nat Methods,* vol. 8, pp. 871-8, 2011.

[11] J. B. Pawley, Ed., *Handbook of Biological Confocal Microscopy*. New York, NY: Springer US, 2006.

[12] L. Thiberville*, et al.*, "In vivo imaging of the bronchial wall microstructure using fibered confocal fluorescence microscopy," *Am J Respir Crit Care Med,* vol. 175, pp. 22-31, Jan 1 2007.

[13] T. D. Wang, "In-Vivo Microscopy," in *Translational Multi-Modality Optical Imaging*, X. Intes and F. Azar, Eds., Norwood, MA: Artech House, 2008, pp. 19-32.

[14] T. D. Wang*, et al.*, "Dual-axis confocal microscope for high-resolution in vivo imaging," *Opt Lett,* vol. 28, pp. 414-6, Mar 15 2003.

[15] T. D. Wang*, et al.*, "Dual-axes confocal microscopy with post-objective scanning and low-coherence heterodyne detection," *Opt Lett,* vol. 28, pp. 1915-7, Oct 15 2003.
[16] T. D. Wang*, et al.*, "Confocal fluorescence microscope with dual-axis architecture and biaxial postobjective scanning," *J Biomed Opt,* vol. 9, pp. 735-42, Jul-Aug 2004.
[17] J. T. Liu*, et al.*, "Efficient rejection of scattered light enables deep optical sectioning in turbid media with low-numerical-aperture optics in a dual-axis confocal architecture," *J Biomed Opt,* vol. 13, p. 034020, May-Jun 2008.
[18] L. K. Wong*, et al.*, "Improved rejection of multiply scattered photons in confocal microscopy using dual-axes architecture," *Opt Lett,* vol. 32, pp. 1674-6, Jun 15 2007.
[19] J. T. Liu*, et al.*, "Dual-axes confocal reflectance microscope for distinguishing colonic neoplasia," *J Biomed Opt,* vol. 11, p. 054019, Sep-Oct 2006.
[20] K. T. Mehta and H. S. Shah, "Correlating parameters of the Henyey-Greenstein phase function equation with size and refractive index of colorants," *Appl Opt,* vol. 24, p. 892, Mar 15 1985.
[21] R. Bays*, et al.*, "Clinical determination of tissue optical properties by endoscopic spatially resolved reflectometry," *Appl Opt,* vol. 35, pp. 1756-66, Apr 1 1996.
[22] W. Piyawattanametha*, et al.*, "In vivo near-infrared dual-axis confocal microendoscopy in the human lower gastrointestinal tract," *J Biomed Opt,* vol. 17, p. 021102, Feb 2012.
[23] H. Ra*, et al.*, "In vivo imaging of human and mouse skin with a handheld dual-axis confocal fluorescence microscope," *J Invest Dermatol,* vol. 131, pp. 1061-6, May 2011.
[24] E. Gounaris*, et al.*, "Live imaging of cysteine-cathepsin activity reveals dynamics of focal inflammation, angiogenesis, and polyp growth," *PLoS One,* vol. 3, p. e2916, 2008.
[25] M. Goetz*, et al.*, "In vivo confocal laser laparoscopy allows real time subsurface microscopy in animal models of liver disease," *J Hepatol,* vol. 48, pp. 91-7, Jan 2008.
[26] P. Anikijenko*, et al.*, "In vivo detection of small subsurface melanomas in athymic mice using noninvasive fiber optic confocal imaging," *J Invest Dermatol,* vol. 117, pp. 1442-8, Dec 2001.
[27] E. Laemmel*, et al.*, "Fibered confocal fluorescence microscopy (Cell-viZio) facilitates extended imaging in the field of microcirculation. A comparison with intravital microscopy," *J Vasc Res,* vol. 41, pp. 400-11, Sep-Oct 2004.
[28] K. H. Al-Gubory and L. M. Houdebine, "In vivo imaging of green fluorescent protein-expressing cells in transgenic animals using fibred confocal fluorescence microscopy," *Eur J Cell Biol,* vol. 85, pp. 837-45, Aug 2006.
[29] G. H. Patterson and D. W. Piston, "Photobleaching in two-photon excitation microscopy," *Biophys J,* vol. 78, pp. 2159-62, Apr 2000.

[30] C. Xu, *et al.*, "Multiphoton fluorescence excitation: new spectral windows for biological nonlinear microscopy," *Proc Natl Acad Sci U S A,* vol. 93, pp. 10763-8, Oct 1 1996.
[31] F. Helmchen, *et al.*, "A miniature head-mounted two-photon microscope. high-resolution brain imaging in freely moving animals," *Neuron,* vol. 31, pp. 903-12, Sep 27 2001.
[32] L. Fu and M. Gu, "Fibre-optic nonlinear optical microscopy and endoscopy," *J Microsc,* vol. 226, pp. 195-206, Jun 2007.
[33] C. J. Engelbrecht, *et al.*, "Ultra-compact fiber-optic two-photon microscope for functional fluorescence imaging in vivo," *Opt Express,* vol. 16, pp. 5556-64, Apr 14 2008.
[34] W. Denk, *et al.*, "Two-photon laser scanning fluorescence microscopy," *Science,* vol. 248, pp. 73-6, Apr 6 1990.
[35] P. L. Hsiung, *et al.*, "Detection of colonic dysplasia in vivo using a targeted heptapeptide and confocal microendoscopy," *Nat Med,* vol. 14, pp. 454-8, Apr 2008.
[36] S. J. Miller, *et al.*, "Targeted detection of murine colonic dysplasia in vivo with flexible multispectral scanning fiber endoscopy," *J Biomed Opt,* vol. 17, p. 021103, Feb 2012.
[37] R. Pasqualini and E. Ruoslahti, "Organ targeting in vivo using phage display peptide libraries," *Nature,* vol. 380, pp. 364-6, Mar 28 1996.
[38] W. Arap, *et al.*, "Targeting the prostate for destruction through a vascular address," *Proc Natl Acad Sci U S A,* vol. 99, pp. 1527-31, Feb 5 2002.
[39] J. K. Scott and G. P. Smith, "Searching for peptide ligands with an epitope library," *Science,* vol. 249, pp. 386-90, Jul 27 1990.
[40] S. E. Cwirla, *et al.*, "Peptides on phage: a vast library of peptides for identifying ligands," *Proc Natl Acad Sci U S A,* vol. 87, pp. 6378-82, Aug 1990.
[41] I. New England Biolabs, "Ph.D.7TM phage display peptide library kit. Instruction manual 2006;ver 2.7."
[42] A. J. Zurita, *et al.*, "Combinatorial screenings in patients: the interleukin-11 receptor alpha as a candidate target in the progression of human prostate cancer," *Cancer Res,* vol. 64, pp. 435-9, Jan 15 2004.
[43] K. A. Kelly and D. A. Jones, "Isolation of a colon tumor specific binding peptide using phage display selection," *Neoplasia,* vol. 5, pp. 437-44, Sep-Oct 2003.
[44] K. Kelly, *et al.*, "Detection of invasive colon cancer using a novel, targeted, library-derived fluorescent peptide," *Cancer Res,* vol. 64, pp. 6247-51, Sep 1 2004.
[45] Z. Qiu, *et al.*, "Targeted vertical cross-sectional imaging with handheld near-infrared dual axes confocal fluorescence endomicroscope," *Biomed Opt Express,* vol. 4, pp. 322-30, Feb 1 2013.
[46] Faulhaber Corp., "Dataheet: smoovy Miniature Drive Systems. www.faulhaber-group.com, 2008."

[47] L. Liu and H. Xie, "3-D Confocal Laser Scanning Microscopy Based on a Full-MEMS Scanning System," *Photonics Technology Letters, IEEE,* vol. 25, pp. 1478-1480, 2013.
[48] L. Wu and H. Xie, "A large vertical displacement electrothermal bimorph microactuator with very small lateral shift," *Sensors and Actuators A: Physical,* vol. 145–146, pp. 371-379, 2008.
[49] H. Ra*, et al.*, "Two-Dimensional MEMS Scanner for Dual-Axes Confocal Microscopy," *Microelectromechanical Systems, Journal of,* vol. 16, pp. 969-976, 2007.
[50] K. L. Turner*, et al.*, "Five parametric resonances in a microelectromechanical system," *Nature,* vol. 396, pp. 149-152, 1998.
[51] U. Hakan*, et al.*, "Vibration mode frequency formulae for micromechanical scanners," *Journal of Micromechanics and Microengineering,* vol. 15, p. 1713, 2005.
[52] V. V. Konotop and V. Kuzmiak, "Parametric resonance of a defect mode in a 2D photonic crystal," *Physical Review B,* vol. 64, p. 125120, 2001.
[53] M.-F. Yu*, et al.*, "Realization of parametric resonances in a nanowire mechanical system with nanomanipulation inside a scanning electron microscope," *Physical Review B,* vol. 66, p. 073406, 2002.
[54] J. Wu*, et al.*, "Loading dynamics of optical trap and parametric excitation resonances of trapped atoms," *Journal of Applied Physics,* vol. 100, pp. -, 2006.
[55] H. Schenk*, et al.*, "A resonantly excited 2D-micro-scanning-mirror with large deflection," *Sensors and Actuators A: Physical,* vol. 89, pp. 104-111, 2001.
[56] Z. Qiu*, et al.*, "Large displacement vertical translational actuator based on piezoelectric thin films," *Journal of Micromechanics and Microengineering,* vol. 20, p. 075016, 2010.
[57] K. R. Oldham*, et al.*, "Thin-Film PZT Lateral Actuators With Extended Stroke," *Microelectromechanical Systems, Journal of,* vol. 17, pp. 890-899, 2008.
[58] T. Jarkko*, et al.*, "Piezoelectric thin-film unimorph actuator for optical fibre alignment applications," *Journal of Optics A: Pure and Applied Optics,* vol. 8, p. S398, 2006.
[59] W. Liu*, et al.*, "A tip–tilt–piston micromirror with a double S-shaped unimorph piezoelectric actuator," *Sensors and Actuators A: Physical,* vol. 193, pp. 121-128, 2013.
[60] M. M. Taketo, "Mouse models of gastrointestinal tumors," *Cancer Sci,* vol. 97, pp. 355-61, May 2006.
[61] J. Heyer*, et al.*, "Mouse models for colorectal cancer," *Oncogene,* vol. 18, pp. 5325-33, Sep 20 1999.
[62] J. Jonkers and A. Berns, "Conditional mouse models of sporadic cancer," *Nat Rev Cancer,* vol. 2, pp. 251-65, Apr 2002.
[63] T. Hinoi*, et al.*, "Mouse model of colonic adenoma-carcinoma progression based on somatic Apc inactivation," *Cancer Res,* vol. 67, pp. 9721-30, Oct 15 2007.

[64] A. Akyol*, et al.*, "Generating somatic mosaicism with a Cre recombinase-microsatellite sequence transgene," *Nat Methods,* vol. 5, pp. 231-3, Mar 2008.